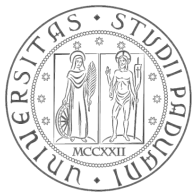


Università degli Studi di Padova

Department of Information Engineering


*Master thesis in ICT for Internet and Multimedia*

# Design and Simulation of Forward-biased Coupling Modulation Ring Modulators


*Master candidate*

**Tommaso Pento**

*Supervisor*

**Luca Palmieri**

*Co-supervisors*

**Jamshidi Kambiz**

**Sourav Dev**



Academic Year 2018/2019, 9th December 2019

**Abstract**

Silicon resonators are nowadays the subject of an intense research activity since they can be employed in many different applications due to their intrinsic advantages such as small footprint and low energy consumption. For instance, they are utilized in optical networks as multiplexers (MUX) and demultiplexers (DEMUX), proving to be extremely useful in the case of Wavelength-Division Multiplexing (WDM) or Dense Wavelength-Division Multiplexing (DWDM) modulation, a technique used to increase the data rate of a given network. They are also suitable as optical modulators when exposed to a varying electric field because of different physical phenomena, such as Kerr effect or Plasma Dispersion Effect (PDE). Furthermore, they have also proven useful for sensing purposes, being extremely sensitive to changes in the environment, such as temperature or physical composition of the device. In this thesis work, the performance of a ring modulator is evaluated with simulation software such as MATLAB and Lumerical. The physical properties are optimized in order to obtain the best results in terms of modulation efficiency, energy consumption and footprint.

# Contents

# List of Figures

# List of Tables

# List of Symbols

| | |
|---|---|
| AD | Add-Drop |
| AP | All-Pass |
| ASK | Amplitude-Shift Keying |
| CMOS | Complementary Metal-Oxide-Semiconductor |
| CROW | Coupled Resonator Optical Waveguide |
| CW | Continuous Wave |
| DEMUX | Demultiplexer |
| DFG | Difference-Frequency Generation |
| DOP | Degree Of Polarization |
| DWDM | Dense Wavelength-Division Multiplexing |
| ER | Extinction Ratio |
| FOM | Figure Of Merit |
| FSK | Frequency-Shift Keying |
| FSR | Free Spectral Range |
| FTTH | Fiber-To-The-Home |
| FWHM | Full Width at Half Maximum |
| GVD | Group Velocity Dispersion |
| HE, EH | Hybrid (modes) |
| IL | Insertion Loss |

| | |
|---|---|
| ISI | InterSymbol Interference |
| LED | Light Emitting Diode |
| MBE | Molecular-Beam Epitaxy |
| MUX | Multiplexer |
| MZM | Mach-Zehnder Modulator |
| NA | Numerical Aperture |
| NRZ | Non-Return-to-Zero |
| OADM | Optical Add-Drop Multiplexer |
| OMA | Optical Modulation Amplitude |
| OOK | On-Off Keying |
| PDE | Plasma Dispersion Effect |
| PECVD | Plasma Enhanced Chemical Vapor Deposition |
| PMD | Polarization Mode Dispersion |
| POF | Plastic Optical Fiber |
| PSK | Phase-Shift Keying |
| Q | Quality Factor |
| SEM | Scanning Electron Microscope |
| SFG | Sum-Frequency Generation |
| SHG | Second-Harmonic Generation |
| SOI | Silicon-On-Insulator |
| SPM | Self-Phase Modulation |
| TE | Transverse Electric |
| TEM | Transverse Electro-Magnetic |
| TIR | Total Internal Reflection |
| TM | Transverse Magnetic |

| | |
|---|---|
| TPA | Two-Photon Absorption |
| UV | Ultraviolet |
| WDM | Wavelength-Division Multiplexing |

# Chapter 1

# Introduction

## 1.1 Motivation

In recent years we have experienced an enormous increase in research regarding photonics. As the name suggests, this relatively young field of study concerns photons and focuses on how they can be manipulated for signal processing, sensing and communication purposes. Since the discovery of light emission by certain semiconductors that led to the first practical Light Emitting Diode (LED) in the 60s and the advent of the optical fiber due to the work of Charles K. Kao and colleagues in the 70s (Nobel Prize in Physics, 2009), photonics has seen a significant growth and covers now a wide variety of different research fields.

Among the most promising ones, silicon photonics is an emerging discipline that establishes the employment of silicon as the optical medium. Silicon has been studied and utilized for decades to build transistors and electrical circuits and as a consequence efficient and well-established manufacturing techniques have been developed to reduce the footprint and the cost of such devices [1]. Furthermore, by integrating photonic systems in electrical circuits it is possible to realize optical interconnects and allow on-chip communications combining both high speed and low power consumption. In fact, conventional metal interconnects are prone to high latency and attenuation limiting their effectiveness at small scale for data rates exceeding 10 Gb/s [2] and will therefore not be suitable in the future. It is believed that silicon photonics will be the main factor for beyond Moore's law computing [3]. In order to build such optical networks, ring resonators are paramount since they have been proven useful in designing small-scale modulators (with an area of few hundreds square micrometers), MUX/DEMUX and delay lines acting as optical buffers, called Coupled Resonator Optical Waveguide (CROW).

Other important applications of photonics are sensing and spectroscopy. In fact, light-matter interaction paves the way for the rise of a large variety of different effects, spanning from absorption to polarization, not to mention scattering and temperature variation. These properties can be exploited in different ways. For example, they might be employed to analyze a particular setting looking for changes in the air composition or sudden temperature surges [4]. In addition, photons can be used in optics to break the diffraction limit allowing nanometric microscopy [5]. Their response to certain materials is beneficial in the case of imaging or spectroscopy, permitting, among others, high-resolution and harmless medical analysis by reducing the exposure to ionizing radiation [6]. In this regard, ring resonators are proven once again useful, since their behavior is heavily affected by the environment. As a consequence, they might react, for instance, to the presence of certain substances to be detected, acting as a label-free biosensor.

For these reasons, ring resonators play an important role in the development and popularity of silicon photonics, and more and more studies are carried out in order to improve and optimize them accordingly to the target operation. A brief summary of some papers on ring resonators and modulators can be found in the next section.

## 1.2 Literature Review

Many research works on ring resonators have been published. Different materials and structures have been studied to ensure the best efficiency and functionality possible.

For instance, in [7] a thorough review of the main properties of ring resonators and their applications is conducted. All the main design parameters are listed and explained, as well as the frameworks currently in use, such as All-Pass (AP) and Add-Drop (AD) resonators, and the possible configurations, such as Optical Add-Drop Multiplexer (OADM) or CROW system. The authors focused also on the different production techniques now employed and the effects of the physical properties on the behavior of the device. In particular, different waveguide sizes and coupling methods are compared with respect to Transverse Electric (TE) and Transverse Magnetic (TM) polarization. Furthermore, the matter of the loss due to bend and waveguide is tackled. Finally, ring modulators are also addressed and their most important attributes explained.

In [8], [9] and [10], optical modulators are studied with respect to different device configurations. In particular, in [8] two different methods are evaluated. In the first case a reverse-biased PN diode-like structure is utilized in

order to achieve modulation by carrier depletion in the optical waveguide, while the second structure is based on a forward-biased PIN diode operating so that the modulation is performed by carrier injection. The results thus found show a substantial difference between the two methods, namely in the frequency of operation and sensitivity parameter. As regards the 3 dB bandwidth, PIN-based modulators are found to be much worse compared to the other configuration (∼1 GHz in the case of PIN, up to 26 GHz in the case of PN). On the other hand, the sensitivity parameter $V_\pi L$ shows an opposite behavior, namely as low as 0.0025 V·cm when it comes to forward-biased devices and around 0.5 V·cm for reverse-biased diodes. Therefore, the authors claim that PIN-based modulators are considerably more efficient but limited to particularly low speed applications, while the other configuration is preferable in all the other cases, despite being less effective when it comes to sheer modulating capabilities. The authors of [9] investigated alternative and advanced waveguide frameworks, such as horizontally-arranged doping layers so to obtain a modulating frequency in excess of 50 GHz in the case of carrier depletion devices. Moreover, data rates of more than 10 Gb/s have been reported by applying to an injection mode modulator a technique called pre-emphasis. Only carrier injection is considered in [10], where data rates up to 12.5 Gb/s are demonstrated by pointing out that the optical response time of the ring is substantially faster compared to the electrical rise time, allowing a better Non-Return-to-Zero (NRZ) modulation especially when pre-emphasis is exploited. The main drawback is the necessity of a high driving voltage (up to 6 V), but accordingly to the authors the issue can be solved by reducing the series resistance (of the order of 7.7 kΩ) with a careful redesign of the junction.

In [11] the main concern is a thorough theoretical study of the bandwidth, with a comparison between optical, electrical and 3 dB bandwidth for a depletion-mode ring modulator. An interesting observation is that the actual bit rate is usually higher than the standard bandwidth, up to a 100% increase. The electrical bandwidth is determined by the RC product, while the optical one depends on the carrier recombination time (in the case of injection type) or in the much faster capacitor discharge (in the case of depletion type).

The main parameters concerning ring resonators are evaluated also in [12], with particular focus on the loss inside the cavity and the self-coupling coefficient with the waveguide. As pointed out by the authors, the two parameters are the most important and can be distinguished by evaluating the output spectrum for different ring configurations and operative wavelengths, since the latter is loss-dependent while the former relies heavily on the coupling distance.

The problem of the waveguide loss is addressed also in [13]. The au-

thors have studied a wide range of waveguides in terms of bend and length, demonstrating that the loss is mainly due to the surface roughness of the vertical sidewalls. The horizontal ones are almost atomically flat and do not constitute a problem in this regard. TM polarization, whose overlap with the cladding is mostly at the top and bottom of the waveguide, shows minor loss compared to TE polarization. The loss has been found to increase with longer wavelengths due to a greater interaction with the cladding. Radii down to 1 $\mu$m are made possible by carefully designing the waveguide, with losses of only 0.086 $\pm$ 0.005 $^{\mathrm{dB}}/_{\mathrm{turn}}$ because of the extreme confinement of the Silicon-On-Insulator (SOI) waveguides used in the experiments, while the standard propagation losses have been calculated to be less than 10 $^{\mathrm{dB}}/_{\mathrm{cm}}$ with reference to practical wavelengths.

## 1.3 Contribution

In this thesis work, the ring modulator configuration based on a PIN junction driven in forward bias is studied and investigated. First, a solid theoretical analysis on ring resonators and modulation techniques is carried out based on previous papers and study material. Afterwards, the injection mode modulator behavior is simulated by means of Lumerical, a popular optoelectronic design software, and consequently optimized. The main parameters considered are:

- Height of the lateral silicon slab connecting the optical waveguide to the electrodes,
- Distance between the electrodes and the optical waveguide (width of the lateral silicon slab),
- Optimization of the doping profile in terms of distribution (constant or diffused) and concentration of dopants,
- Bend of the waveguide, determining the radius of the ring resonator, and
- Coupling system with the waveguide, comprising different structures and gaps between ring and input waveguide.

Finally, the important parameters thus extracted, such as loss and refractive index change, are imported in MATLAB and subsequently analyzed. The final output spectra are then calculated and the most important Figures Of Merit (FOMs) are derived and discussed in order to determine the best configuration possible.

## 1.4 Thesis Outline

The thesis is organized as follows:

**Chapter 2** discusses some fundamentals of electromagnetic theory, considering both the wave and the particle concept, together with some important properties and characteristics.

**Chapter 3** deals with light propagation with focus on waveguides and their structure, as well as some applications.

**Chapter 4** regards the modulation part of the work, comprising different methods with focus on carrier injection.

**Chapter 5** describes ring resonators, their layouts, parameters and usage.

**Chapter 6** presents the simulation results and the comments on the data obtained.

**Chapter 7** sums up the content of the thesis, and comprises also possible future works.

**Chapter 8** contains some further calculations not presented in the previous chapters for the sake of brevity and clarity.

# Chapter 2

# Fundamentals

A thorough display of electromagnetic theory can be found in [14], [15] and [16].

## 2.1 Maxwell's Equations

### 2.1.1 Definition

Maxwell's equations are the fundamental postulates of classical electromagnetics explaining every phenomena that refer to light as a wave. In the time domain, these can be written in the differential form as:

Faraday's Law:

$$\nabla \times \bar{e}\,(\bar{r},t) = -\frac{\partial \bar{b}\,(\bar{r},t)}{\partial t} \tag{2.1}$$

Ampere's Law:

$$\nabla \times \bar{h}\,(\bar{r},t) = -\frac{\partial \bar{d}\,(\bar{r},t)}{\partial t} + \bar{j}(\bar{r},t) \tag{2.2}$$

Gauss' Law:

$$\nabla \cdot \bar{b}\,(\bar{r},t) = 0 \tag{2.3}$$

Gauss' Law for magnetism

$$\nabla \cdot \bar{d}\,(\bar{r},t) = \rho_v\,(\bar{r},t) \tag{2.4}$$

With $\nabla\times$ curl operator and $\nabla\cdot$ divergence operator. Here, considering a 3-dimensional cartesian reference frame in which the position vector is $\bar{r}(x,y,z) = x\widehat{x} + y\widehat{y} + z\widehat{z}$ with $\widehat{x}$, $\widehat{y}$ and $\widehat{z}$ versors:

- $\bar{e}(\bar{r},t) = e_x(\bar{r},t)\,\widehat{x} + e_y(\bar{r},t)\,\widehat{y} + e_z(\bar{r},t)\,\widehat{z}$ [V/m] is the electric field vector;
- $\bar{b}(\bar{r},t) = b_x(\bar{r},t)\,\widehat{x} + b_y(\bar{r},t)\,\widehat{y} + b_z(\bar{r},t)\,\widehat{z}$ [Wb/m²] is the magnetic inductance (flux) field vector;
- $\bar{h}(\bar{r},t) = h_x(\bar{r},t)\,\widehat{x} + h_y(\bar{r},t)\,\widehat{y} + h_z(\bar{r},t)\,\widehat{z}$ [A/m] is the magnetic field vector;
- $\bar{d}(\bar{r},t) = d_x(\bar{r},t)\,\widehat{x} + d_y(\bar{r},t)\,\widehat{y} + d_z(\bar{r},t)\,\widehat{z}$ [C/m²] is the electric displacement (flux) field vector;
- $\bar{j}(\bar{r},t) = j_x(\bar{r},t)\,\widehat{x} + j_y(\bar{r},t)\,\widehat{y} + j_z(\bar{r},t)\,\widehat{z}$ [A/m²] is the electric current density vector;
- $\rho_v(\bar{r},t)$ [C/m³] is the electric charge density.

Equations (2.3) and (2.4) are directly derived from equations (2.1) and (2.2) by using Stoke's and Gauss' (divergence) theorems, as can be seen in Appendix A, and therefore do not add any information. As a consequence, these equations cannot be directly solved as the number of unknown variables exceeds the number of independent equations [17]. As a consequence, additional constitutive relations linking the field vectors must be taken into consideration. In particular, it is common to consider $\bar{e}(\bar{r},t)$ and $\bar{h}(\bar{r},t)$ to be the "primary" responses whereas $\bar{b}(\bar{r},t)$, $\bar{d}(\bar{r},t)$ and $\bar{j_T}(\bar{r},t)$ are "secondary" and therefore written as a function of the electric and magnetic field vectors [18]. These relations depend on the medium in which the wave is propagating and can be written in the simplest case (vacuum) as:

$$\bar{d}(\bar{r},t) = \varepsilon_0 \bar{e}(\bar{r},t) \tag{2.5}$$

$$\bar{b}(\bar{r},t) = \mu_0 \bar{h}(\bar{r},t) \tag{2.6}$$

$$\bar{j}(\bar{r},t) = 0 \tag{2.7}$$

Where

- $\varepsilon_0 \simeq 8.85419 \times 10^{-12}$ F/m is called vacuum permittivity and
- $\mu_0 \simeq 1.25664 \times 10^{-6}$ H/m is called vacuum permeability,

Yielding

$$\nabla \times \bar{e}\,(\bar{r},t) = -\mu_0 \frac{\partial \bar{h}\,(\bar{r},t)}{\partial t} \tag{2.8}$$

$$\nabla \times \bar{h}\,(\bar{r},t) = \varepsilon_0 \frac{\partial \bar{e}\,(\bar{r},t)}{\partial t} \tag{2.9}$$

Which is a well-posed problem.
When not in vacuum, the parameters must be such that:

- $\varepsilon_0$ becomes the electric permittivity $\varepsilon = \varepsilon_r \varepsilon_0$ with $\varepsilon_r$ dimensionless quantity called relative permittivity of the specific medium;
- $\mu_0$ becomes the magnetic permittivity $\mu = \mu_r \mu_0$ with $\mu_r$ dimensionless quantity called relative permeability of the specific medium. It is usually 1 in the case of dielectric media as the ones considered in this thesis;
- $\bar{j}\,(\bar{r},t) = \sigma \bar{e}\,(\bar{r},t)$ where $\sigma$ [S/m] is called electric conductivity. It determines the nature of the specific material (in particular, when $\sigma \gg \varepsilon\omega$, with $\omega$ [1/s] angular frequency of the electromagnetic wave, it is called conductor, otherwise insulator [17]).

The relations thus derived are only valid for a medium which is linear, isotropic, homogeneous, time invariant and non-dispersive. A more thorough and accurate investigation should also take into account real-world properties of the materials, such as:

- Non-linearity: the response of the medium to the incoming radiation depends on the field strength. Usually this is considered when the power density is high and can be modeled by writing the electric permittivity $\varepsilon(\bar{e})$ as a function of the electric field.
- Non-homogeneity: the response is dependent on the position within the medium. It can be modeled by writing the electric permittivity $\varepsilon(\bar{r})$ as a function of the position within the material.
- Non-stationarity: the response is dependent on the particular time instant. Examples of non-stationary materials can be fluids, moving objects or excited matter. It can be modeled by writing the electric permittivity $\varepsilon(t)$ as a function of the time.
- Anisotropy: the response is dependent on the specific direction of the electric field vector. It can be modeled by writing the electric permittivity $\bar{\bar{\varepsilon}}$ as a tensor.

- Dispersion: the response is dependent on the frequency of the incoming light. It can be modeled by writing the electric permittivity $\varepsilon(\omega)$ as a function of the frequency.

For most of these properties, the ideal situation can be considered. In the case of transmission through waveguides (for examples when dealing with ring modulators), neglecting dispersion is however not feasible since it is not possible to be in a monochromatic regime, thus having only a specific frequency.

### 2.1.2 Complex vector representation

In general the fields are functions of time and position. However, the same information can be represented with complex phasors acting as an envelope for the field [17], such as

$$\bar{e}\,(\bar{r},t) = Re[\bar{E}(\bar{r})e^{-i\omega t}] \tag{2.10}$$

$$\bar{h}\,(\bar{r},t) = Re[\bar{H}(\bar{r})e^{-i\omega t}] \tag{2.11}$$

$$\rho_v\,(\bar{r},t) = Re[\rho(\bar{r})e^{-i\omega t}] \tag{2.12}$$

Where $E(\bar{r})$, $H(\bar{r}) \in \mathbb{C}^3$ such that the spatial and temporal components are split and $i$ is the imaginary unit.

The relations are now in the frequency domain after the Fourier transform has been applied to the time domain versions.

The Maxwell's equations (2.2), (2.3), (2.8) and (2.9) can therefore be respectively rewritten with reference to good insulants ($\sigma$ negligible) as

$$\nabla \times \bar{E}(\bar{r}) = -i\omega\mu_0\bar{H}(\bar{r}) \tag{2.13}$$

$$\nabla \times \bar{H}(\bar{r}) = i\omega\varepsilon\bar{E}(\bar{r}) \tag{2.14}$$

$$\nabla \cdot \bar{H}(\bar{r}) = 0 \tag{2.15}$$

$$\nabla \cdot \bar{E}(\bar{r}) = \rho\,(\bar{r}) \tag{2.16}$$

A simple derivation can be made in a region in which the source of the electromagnetic field is not present. The objective is to study the propagation

of the fields. By using some well-known vector identities (Appendix B), one can retrieve the homogeneous Helmholtz equations

$$\nabla^2 \bar{E}(\bar{r}) + \omega^2 \mu_0 \varepsilon \bar{E}(\bar{r}) = 0 \tag{2.17}$$

$$\nabla^2 \bar{H}(\bar{r}) + \omega^2 \mu_0 \varepsilon \bar{H}(\bar{r}) = 0 \tag{2.18}$$

With $\nabla^2$ Laplacian operator. Here different parameters can be defined. For instance, $c = \frac{1}{\sqrt{\mu_0 \varepsilon_0}} \simeq 3 \times 10^8$ $^{\mathrm{m}}/_{\mathrm{s}}$ is called speed of light in vacuum, such that $v_p = \frac{c}{\sqrt{\varepsilon_r}}$ is the velocity of propagation (also called phase velocity) inside a medium whose relative permittivity is $\varepsilon_r$. Furthermore, by separation of the variables applied to equation (2.17) one can write

$$\bar{E}(\bar{r}) = \bar{E}_0 e^{-i\bar{k}\cdot\bar{r}} \tag{2.19}$$

Where $\bar{k} = k_x \widehat{x} + k_y \widehat{y} + k_z \widehat{z}$ [$^1/_{\mathrm{m}}$] is called wave vector such that $|\bar{k}|^2 = \omega^2 \mu_0 \varepsilon$ [$^1/_{\mathrm{m}^2}$] and $|\bar{k}| = k = \omega \sqrt{\mu_0 \varepsilon_0} \sqrt{\varepsilon_r} = \frac{\omega}{c} \sqrt{\varepsilon_r} = \frac{\omega}{c} n$ [$^1/_{\mathrm{m}}$] is called wave number, with $n$ being the refractive index of the material.

Subsequently, by applying equation (2.13) the magnetic field is calculated as

$$\begin{aligned} \bar{H}(\bar{r}) = \frac{\bar{k} \times \bar{E}_0}{\omega \mu_0} e^{-i\bar{k}\cdot\bar{r}} = \frac{|\bar{k}| \hat{k} \times \bar{E}_0}{\omega \mu_0} e^{-i\bar{k}\cdot\bar{r}} = \\ = \sqrt{\frac{\varepsilon}{\mu_0}} \hat{k} \times \bar{E}_0 e^{-i\bar{k}\cdot\bar{r}} = \frac{\hat{k} \times \bar{E}_0}{\eta} e^{-i\bar{k}\cdot\bar{r}} = \bar{H}_0 e^{-i\bar{k}\cdot\bar{r}} \end{aligned} \tag{2.20}$$

Where $\eta$ [$\Omega$] is called intrinsic medium impedance. In the case of vacuum, $\eta_0 \simeq 377\ \Omega$.

The solution thus found is named plane wave because the plane orthogonal to $\bar{k}$ is called plane of constant phase due to the fact that all the points there have the same phase. $\bar{k}$ represents the propagation direction. Moreover, $\bar{k}$, $\bar{E}(\bar{r})$ and $\bar{H}(\bar{r})$ are all orthogonal to each other, forming a right-handed triplet of vectors [19]. The periodicity of the wave, that is, the distance along the propagation direction at which the electric (or magnetic) field recovers the same pattern is called wavelength, written as $\lambda = \frac{2\pi}{|\bar{k}|}$ [m].

When the phasor is reverted back to its real representation, the wave recovered is a sinusoidal function that can be written as

$$\bar{e}(\bar{r}, t) = e_0(\bar{r})\ \cos(\bar{k} \cdot \bar{r} - \omega t + \varphi_e) \tag{2.21}$$

$$\bar{h}(\bar{r},t) = h_0(\bar{r})\,\cos(\bar{k}\cdot\bar{r} - \omega t + \varphi_h) \tag{2.22}$$

Where $\varphi$ represents the phase offset which is not important in absolute terms but it is a useful concept while comparing two or more different waves (see section 2.7).

This kind of solution represents a wave that travels in a given direction without losing energy and therefore is not realistic. Moreover, it carries infinite energy as the plane orthogonal to the propagation vector is infinite (there is no divergence of the wave vectors) [18]. The concept of plane waves, however, is still useful because any real wave can be defined as the sum of a certain number of plane waves. Moreover, far from the source the wave front can be effectively approximated by a plane wave.

To give an illustration, a more realistic solution would be the so-called spherical wave, that can be written as [17]

$$\bar{E}(\bar{r}) = \frac{\bar{E}_0}{|\bar{r}|}e^{-i\bar{k}\cdot\bar{r}} \tag{2.23}$$

In this case, the sphere of radius $|\bar{r}|$ represents the surface of constant amplitude and phase. The field decays with the distance travelled by the wave.

## 2.2 Losses

It is however possible to account for losses due to the material. When $\sigma$ is not negligible, the permittivity constant becomes complex and can be written as $\varepsilon_c = \varepsilon - i\frac{\sigma}{\omega}$. In this case, the propagation vector is no longer real and comprises also an imaginary part, as $\bar{s} = \bar{a} + i\bar{k}$ where $\bar{a} = Re[\bar{s}] \in \mathbb{R}^3$ is called attenuation vector and $\bar{k} = Im[\bar{s}] \in \mathbb{R}^3$ is the previous phase vector. $\bar{a}$ and $\bar{k}$ can be considered parallel [17]. Now the fields of the plane wave can be written as

$$\bar{E}(\bar{r}) = \bar{E}_0 e^{-\bar{a}\cdot\bar{r}} e^{-i\bar{k}\cdot\bar{r}} \tag{2.24}$$

$$\bar{H}(\bar{r}) = \bar{H}_0 e^{-\bar{a}\cdot\bar{r}} e^{-i\bar{k}\cdot\bar{r}} \tag{2.25}$$

The electromagnetic field is therefore reducing its amplitude while travelling along the propagation direction, the attenuation coefficient being $\alpha = |\bar{a}|$ [1/m]. Finally, it is worth noting that as the frequency of the wave increases, the imaginary part tends to zero. As a consequence, at high frequencies conductors (high $\sigma$) behave like insulants.

## 2.3 Power

The power density of an electromagnetic wave represents the flow of energy per unit time across a unit area. It is traditionally described with the so-called Poynting vector as

$$\bar{S}(\bar{r}) \triangleq \bar{E}(\bar{r}) \times \bar{H}^*(\bar{r}) = \frac{|\bar{E}(\bar{r})|^2}{\eta}\hat{k} \ [\mathrm{W/m^2}] \tag{2.26}$$

Where the apex $*$ represents the complex conjugate. The energy flows orthogonally to both the electric and the magnetic fields and is therefore parallel to the propagation vector $\bar{k}$. The complete derivation can be found in Appendix C.

When the fields are represented by sinusoidal functions, as in equation (2.19), the oscillation of the Poynting vector is extremely fast and consequently the instantaneous value is not practical to measure. Usual detectors are able to only record the time-averaged value, integrated over a certain time interval $T$, which is often called irradiance (intensity) and can be written as [19]

$$I = \frac{|\bar{E}(\bar{r})|^2}{2\eta} = \frac{1}{2}\varepsilon_0 cn|\bar{E}(\bar{r})|^2 \ [\mathrm{W/m^2}] \tag{2.27}$$

To calculate the actual power flowing through a surface S one can write

$$P = \int_S I \ \partial A \ [\mathrm{W}] \tag{2.28}$$

## 2.4 Polarization

The polarization is a property of the electromagnetic waves that specifies the oscillation direction of the fields. In particular, both the electric and the magnetic fields oscillate and their composition/predictability determines the degree and type of polarization. Usually, polarization only refers to the electric field since the two are always perpendicular (see equation (2.20)).

Let us take the case of light travelling in a homogeneous isotropic medium, as depicted in figure 2.1. This particular wave is called Transverse Electromagnetic (TEM) since both electric and magnetic fields are orthogonal to the direction of propagation ($\hat{z}$), meaning that $E_{0z} = H_{0z} = 0$.

The polarization is defined as the position of the tip of the electric field vector at a specific position $\hat{r}$ and time $t$ [18]. To analyze the polarization state of a specific wave, the electric field vector is usually decomposed in its

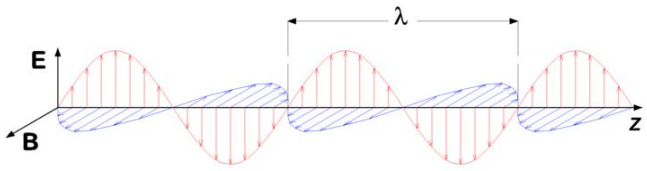


Figure 2.1: *Transverse electromagnetic wave* [20]

$\hat{x}$ and $\hat{y}$ components and their amplitude and relative phase are taken into consideration, as in

$$\bar{e}(z,t) = e_{0x}\,\cos(kz - \omega t + \varphi_x)\hat{x} \pm e_{0y}\cos(kz - \omega t + \varphi_y)\hat{y} \tag{2.29}$$

Which is equivalent to

$$\bar{e}(z,t) = e_{0x}\,\cos(kz - \omega t)\hat{x} \pm e_{0y}\cos(kz - \omega t + \varphi)\hat{y} \tag{2.30}$$

With phase difference $\varphi = \varphi_x - \varphi_y$ (the important parameter to be considered).

In particular, when we have a positive term $\oplus$ the polarization is said to be right-handed (clockwise from the source point of view), while in the case of a negative term $\ominus$ it is left-handed (counter-clockwise from the source point of view). The handedness of the polarization results in two independent degrees of freedom [17].

The field is dependent on both position and time. Let us set $z = 0$ and analyze the time evolution regarding a fixed position (analogous to the case in which the time is fixed and the study is carried out with respect to the position) [21].

In general, the polarization is said to be elliptical since the tip of the electric field vector draws an ellipse in time around the position $z = 0$.

When instead $\varphi = m\pi$, $m \in \mathbb{N}$, the wave is called linearly polarized. In fact, the two components $e_{0x}$ and $e_{0y}$ maintain the same ratio (since they grow and decrease synchronously). A particular condition is met when either $e_{0x}$ or $e_{0y}$ are null, which means that the electric field oscillates along one of the previously defined $\hat{x}$ or $\hat{y}$ axes.

The last possibility is to have $e_{0x} = e_{0y}$ and $\varphi = (2m+1)\frac{\pi}{2}$, $m \in \mathbb{N}$. Here the polarization is circular because the pattern shown by the vector tip is circular.

In figure 2.2 the three different polarization types for TEM waves are shown. The blue and green curves are the amplitudes of the $\hat{x}$ and $\hat{y}$ components of the electric field.

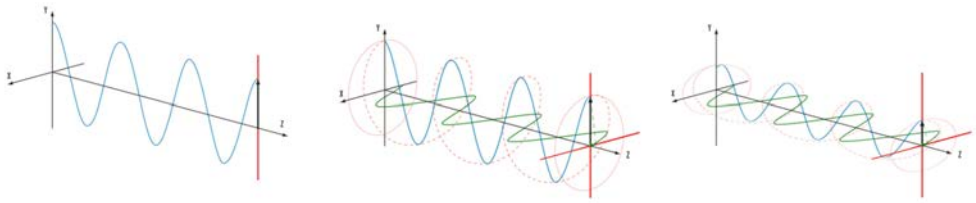

Figure 2.2: *Polarization: linear (left), circular (center), elliptical (right)* [18]

However, natural light is mainly unpolarized, meaning that the polarization direction (due to the amplitude of the two different components and the phase difference) fluctuates randomly in an unpredictable way. Even though natural light sources usually emit incoherent radiation, there is always a certain degree of polarization, primarily due to scattering (molecules acts as small antennas and release polarized light because of internal vibrations). It is therefore possible to define the Degree Of Polarization (DOP) as [18], [21]:

$$V = \frac{I_{max} - I_{min}}{I_{max} + I_{min}} = \frac{I_p}{I_p + I_{up}} \tag{2.31}$$

Where $I_{max}$ and $I_{min}$ are the maximum and minimum light intensities that are measured by means of a polarizer (which is an optical filter sensitive only to a specific type of polarization) rotated by 360°, $I_p$ is the intensity of the polarized light while $I_{up}$ is the intensity of the unpolarized part.

In waveguides no TEM light can propagate. Three are the main categories of allowed polarization: TE, TM or Hybrid (HE, EH). In the case of TE polarization (also called s-polarization) the electric field is transverse to the direction of propagation ($E_{0z} = 0$) while the magnetic field is orthogonal. Regarding TM polarization (also called p-polarization), however, the electric field is orthogonal to the direction of propagation while the magnetic field is transverse ($H_{0z} = 0$). Finally, a hybrid polarization entails both the electric and the magnetic fields not being zero in the direction of propagation ($H_{0z} \neq 0$, $E_{0z} \neq 0$) and it can be expressed by a linear superposition of TE and TM modes.

## 2.5 Wave packets

All the waves considered so far are monochromatic, meaning that they comprise a single frequency therefore being infinite in the time domain (pure sinusoidal signals). Let us now introduce the concept of wave packets, which are collections of waves at different frequencies. The simplest case consists

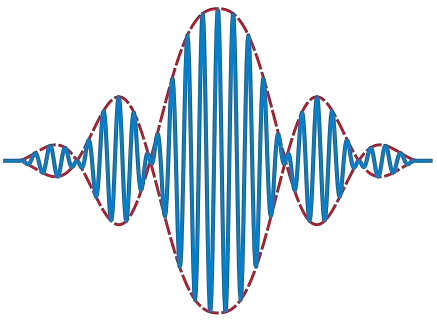

Figure 2.3: *Wave packet* [22]

solely of two monochromatic waves whose angular frequencies ($\omega_1$ and $\omega_2$) and wave numbers ($k_1$ and $k_2$) are only slightly different. Let us define $\omega_A = \frac{\omega_1+\omega_2}{2}$ and $\Delta\omega = \frac{\omega_1-\omega_2}{2}$ such that $\omega_1 = \omega_A + \Delta\omega$ and $\omega_2 = \omega_A - \Delta\omega$. Furthermore, let us define $k_A = \frac{k_1+k_2}{2}$ and $\Delta k = \frac{k_1-k_2}{2}$ such that $k_1 = k_A + \Delta k$ and $k_2 = k_A - \Delta k$. Let us assume that the waves are travelling in the direction of $\hat{z}$, so that the electric fields extend in the plane formed by $\hat{x}$ and $\hat{y}$. The superposition of the two waves can be written as [18]

$$\bar{E}(x,y,z) = E_0(x,y)e^{i\{(k+\Delta k)z-(\omega+\Delta\omega)t\}} + E_0(x,y)e^{i\{(k-\Delta k)z-(\omega+\Delta\omega)t\}} = \\ = 2E_0(x,y)e^{i(kz-\omega t)}\cos(\Delta kz - \Delta\omega t) \quad (2.32)$$

Where $\Delta kz - \Delta\omega t$ is the modulation envelope travelling at the group velocity $v_g$, which is defined as

$$v_g = \frac{\Delta\omega}{\Delta k} = v_p(1 - \frac{k}{n}\frac{\partial n}{\partial k}) \quad (2.33)$$

Based on the group velocity one can also derive the expression for the group index $n_g$, which is

$$n_g = \frac{c}{v_g} = n - \lambda\frac{\partial n}{\partial\lambda} \quad (2.34)$$

From equations (2.33) and (2.34) one can infer that the refractive index is not constant over different frequencies. This concept is called dispersion and is covered in section 3.4.

The energy of the wave packet travels at the group velocity.

In figure 2.3 a generic wave packet is shown. The red dashed line corresponds to the packet envelope, which is travelling at the group velocity. The blue solid line represents the phase velocity, which is usually considerably higher.

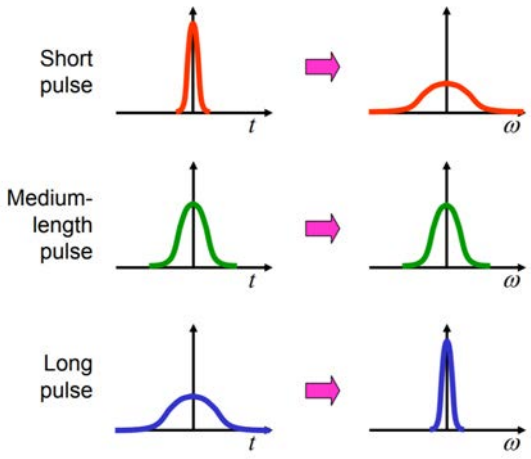


Figure 2.4: *Time/frequency relation of a generic light pulse* [23]

## 2.6 Light pulses

A wave packet is the composition of waves at different wavelengths and its shape is different compared to that of a monochromatic wave. In nature no pure monochromatic radiation exists and the concept of broadband pulses is similar to that of wave packets. Given the relation between the time and frequency domain provided by the Fourier transform, it is possible to assume that a light pulse which is emitted in a short period of time is extremely spread in frequency, while long pulses in the time domain result in narrow-band radiation (see figure 2.4).

Following the Heisenberg principle

$$\Delta E \Delta t = \frac{h}{4\pi} \tag{2.35}$$

Where $\hbar \simeq 6.626 \times 10^{-34}$ J·s is the Planck constant, $\Delta E$ and $\Delta t$ the energy and time uncertainty respectively. Since $\Delta E = h\Delta f$ is recognized as the energy carried by a single photon (which is a quantum of the electromagnetic radiation when the light is considered as a particle [24], see section 2.8 for more details), we can derive the expression for the frequency uncertainty

$$\Delta f = \frac{1}{4\pi \Delta t} \tag{2.36}$$

As we can see, the frequency spectrum $\Delta f$ is broader when the emission time $\Delta t$ shrinks. For instance, a Gaussian pulse can be written in the time domain as [25]

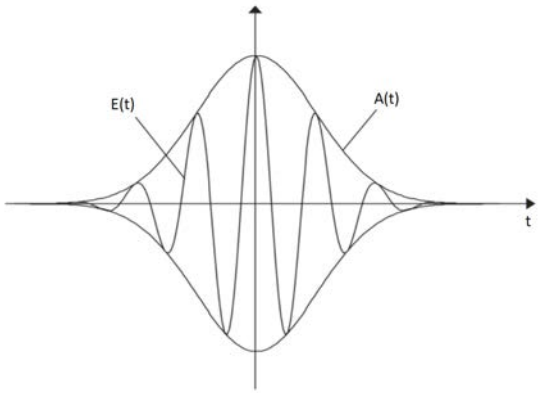


Figure 2.5: *Gaussian pulse in the time domain* [26]

$$E(t) = A(t)e^{i\omega_0 t} = E_0 e^{-(t/\tau_C)^2} e^{i(\omega_0 t + \varphi(t))} \tag{2.37}$$

Where $A(t) = E_0 e^{-(t/\tau_C)^2} e^{i\varphi(t)}$ is the complex envelope, $E_0 e^{-(t/\tau_C)^2}$ is the amplitude of the wave such that $\tau_C = cL_C$ is the coherence time (corresponding to the moment in time in which the amplitude becomes lower than $1/e$ its initial value $E_0$), $\varphi(t)$ is the phase and $\omega_0$ is the central frequency, as can be seen in figure 2.5.

The same pulse in the frequency domain is [18]

$$S(f) \propto e^{-(\frac{f-f_0}{\Delta f})^2} \tag{2.38}$$

With $f_0$ the central frequency and $\Delta f$ the spread of the spectrum in the frequency domain. In particular,

$$\Delta f \tau_C = 0.441 \tag{2.39}$$

Is the relation between the span in time and frequency accordingly to the Heisenberg principle in the case of Gaussian pulses [23].

## 2.7 Interference

Let us consider two waves generated by the same source (and therefore of the same frequency) travelling different paths (of difference $\Delta L$) and later superimposing. The two waves can be initially written as

$$\bar{E}_1(\bar{r}) = \bar{E}_{01} e^{-i(\bar{k}\cdot\bar{r} - \omega t)} \quad \text{and} \quad \bar{E}_2(\bar{r}) = \bar{E}_{02} e^{-i(\bar{k}\cdot\bar{r} - \omega t)} \tag{2.40}$$

At the crossing point it will be

$$\bar{E}_1(\bar{r}) = \bar{E}_{01}e^{-i(\bar{k}\cdot\bar{r}-\omega t+\varphi_1)} \text{ and } \bar{E}_2(\bar{r})=\bar{E}_{02}e^{-i(\bar{k}\cdot\bar{r}-\omega t+\varphi_2)} \tag{2.41}$$

With $\varphi_1$ and $\varphi_2$ phase offsets due to the optical path such that $\Delta\varphi = \varphi_2 - \varphi_1 = |\bar{k}| \cdot \Delta L$ is the phase difference. When superimposing, it is possible to sum $\bar{E}(\bar{r}) = \bar{E}_1(\bar{r}) + \bar{E}_2(\bar{r})$ and therefore to write the intensity as [18]

$$I_T = \frac{1}{2}\varepsilon_0 cn|\bar{E}(\bar{r})|^2 = \frac{1}{2}\varepsilon_0 cn(|\bar{E}_1(\bar{r})|^2 + |\bar{E}_2(\bar{r})|^2 + 2Re[\bar{E}_1(\bar{r})\bar{E}_2(\bar{r})^*]) = \\ = I_1 + I_2 + 2\sqrt{I_1 I_2}\cos(\Delta\varphi) \tag{2.42}$$

As can be seen, the phase difference $\Delta\varphi = \varphi_2 - \varphi_1$ depends on the optical path as $\varphi = \bar{k}\cdot\bar{r}$ is paramount to determine the total intensity at the crossing point.

For instance, when $\Delta\varphi = (2m+1)\pi,\ m \in \mathbb{N}$, we have

$$I_T = I_1 + I_2 - \varepsilon_0 cn|\bar{E}_1(\bar{r})||\bar{E}_2(\bar{r})| < I_1 + I_2 \tag{2.43}$$

Which is called destructive interference since the optical power is reduced.

When $\Delta\varphi = 2\pi m,\ m \in \mathbb{N}$, we have

$$I_T = I_1 + I_2 + \varepsilon_0 cn|\bar{E}_1(\bar{r})||\bar{E}_2(\bar{r})| > I_1 + I_2 \tag{2.44}$$

Which is called constructive interference since the optical power is increased.

For all the other intermediate cases, the output wave will have an intensity included between the intensity $I_T$ given in the case of equations (2.43) and (2.44).

A specific situation, which can be seen in figure 2.6, is given when considering two waves of the same intensity, such that $\bar{E}_{01} = \bar{E}_{02} = \bar{E}_0$ and, as a consequence, $I_1 = I_2 = I$, yielding $I_T = 0$ in the case of destructive interference and $I_T = 4I$ in the case of constructive interference. As can be seen, it is possible to completely negate the electromagnetic field in specific points. It is also possible to extend the formula to the case of $N$ impinging waves, for which the constructive interference reads $I_T = N^2 I$ [19].

However, it is important to point out that interference occurs as long as $\Delta\varphi$ is well-defined, condition which is called temporal coherence. If the phase varies randomly, no pattern is recognizable and $I_T = I_1 + I_2$ [18].

Furthermore, light which is not monochromatic experiences interference as well but on a smaller scale, meaning that the temporal coherence is not an absolute property but will eventually subside: even light which is highly

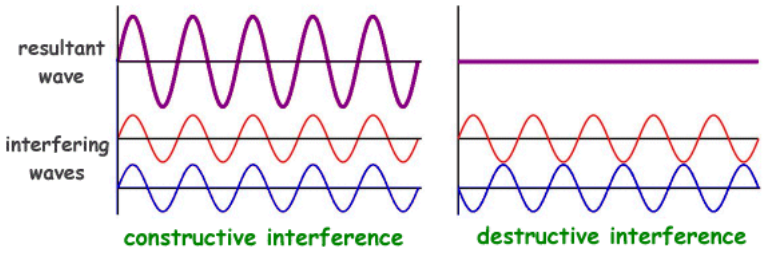


Figure 2.6: *Wave interference* [27]

coherent when emitted will lose its phase relation after a certain amount of time. The distance travelled before becoming incoherent is called coherence length ($L_C$) and it depends, among other factors, on the source and the purity of the light (i.e. how large is the light frequency spectrum). Examples of incoherent sources (for which the pulse is spread in the frequency domain) are light bulbs and the Sun. LEDs can be considered as partially coherent sources ($L_C \simeq 10$ mm) while lasers are usually categorized as coherent light sources ($L_C$ up to 400 m) [18].

## 2.8 Absorption and emission

So far light has been considered as electromagnetic waves. However, many phenomena could not be explained by considering light only as a wave, giving rise to the wave-particle duality [24]. In quantum mechanics the concept of photon has been introduced. A photon is a massless quantum of energy which is considered as the building block of the electromagnetic radiation, such as the electron is the the building block of the electric current. A photon carries a precise amount of energy and a specific momentum which are defined as (de Broglie hypothesis)

$$E = h\nu = \hbar\omega \tag{2.45}$$

$$\bar{p} = \hbar\bar{k} \tag{2.46}$$

Where $\hbar = {}^{h}/_{2\pi}$ is called reduced Planck constant.

To explain the interaction between light and matter, the concept of energy levels has to be introduced. Given an atom, the electrons occupy only specific quantized orbitals, each one with its own energy (increasing while moving away from the nucleus), as can be seen in figure 2.7. In particular, only a certain number of electrons can settle in a single orbital and therefore the

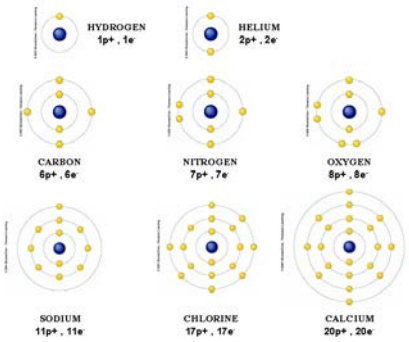


Figure 2.7: *Atomic orbital, examples* [29]

more electrons an atom has the more energy levels are occupied. Following the Aufbau principle, the electrons tend to fill the lowest available energy orbitals [28].

When numerous atoms are closely packed together, as in common materials, the orbitals of the different atoms mix together creating energy bands in which the electrons can settle. The most important bands in photonic applications are the last one occupied by electrons (called valence band) and the first empty one (called conduction band) [30]. Electron transport (current) takes place in the conduction band where the electrons can physically move from an empty state to the other. The energy difference between these two bands is called energy gap (or band gap), such that $E_G = E_C - E_V$ with $E$ the energy of the band. A distinction can be made regarding the electric properties, namely conductors are materials in which the energy gap is zero (and as a consequence electrons can easily move to the conduction band and start flowing), semiconductors display a small energy gap (the current can still flow but not as smoothly) and insulators encompass materials whose energy gap is exceedingly large (leading to little to no current flowing through), as depicted in figure 2.8.

In particular, electrons can be promoted from a lower energy state to a higher energy one by providing the right amount of energy $E_G$. The energy can be supplied by different sources, among which there are photons. In fact, a photon with energy $h\nu = E_G$ can be absorbed in the material after clashing with an electron in the valence band, which is subsequently promoted to the conduction band. The photon thus disappears reducing the overall light intensity [30]. The inverse process is called emission and entails an already excited electron which decays to the valence band after emitting a photon, as can be seen in figure 2.9.

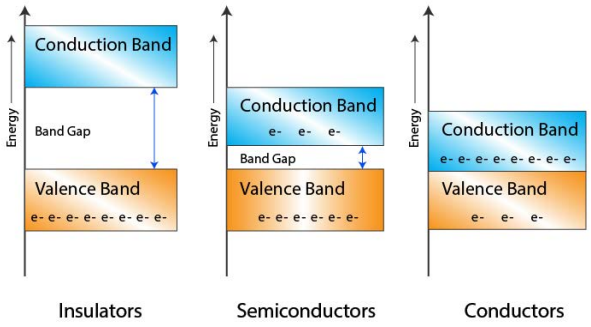


Figure 2.8: *Energy bands for different materials* [31]

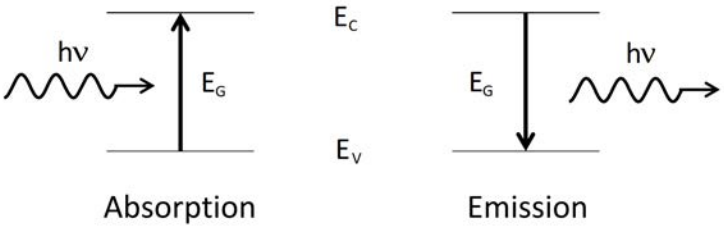


Figure 2.9: *Absorption and emission* [18]

## 2.9 Scattering

Scattering is a phenomenon that describes how the light is deflected when hitting localized particles called scatterers. Scatterers can be anything ranging from molecules to density fluctuations in a medium otherwise homogeneous. There are two main kinds of optical scattering: elastic, in which case the wavelength of the scattered light is the same as the one of the incident light (there is no loss of energy to the scatterer) and inelastic, in which case the scatterer is given or taken some energy from the light that therefore experiences a spectrum shift [32]. Well-known elastic events are Rayleigh, Mie and geometric scattering, while examples of inelastic phenomena are Raman, Brillouin and Compton scattering. In general it is possible to model the scattering as the absorption of the light (because the scatterer is driven into oscillatory motion) followed by an instantaneous re-emission of the photon, which will have the same energy of the incoming one in the case of elastic scattering or different otherwise [33]. The direction of propagation, however, will most likely be different (see figure 2.10 to have an illustration).

When it comes to elastic scattering, the main discerning parameter is the relation between the wavelength of the light and the size of the scatterer. In

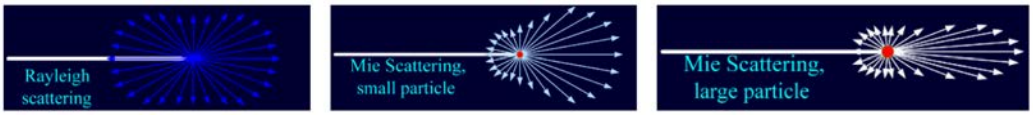


Figure 2.10: *Elastic scattering* [18]

particular, given $k$ the wavenumber and $a$ the size of the particle, we can distinguish [18]

- When $ka << 1$ it is Rayleigh scattering;
- When $ka \sim 1$ it is Mie scattering;
- When $ka >> 1$ it is geometric scattering.

Geometric scattering can be solved macroscopically with a geometrical approach. In figure 2.10 Rayleigh and Mie scattering are shown. In particular, Rayleigh scattering is called isotropic, since the photon can be deflected everywhere around the scatterer with equal probability. On the other hand, Mie scattering is forward-pointing, meaning that the most probable scattering direction is opposite to the direction of the incoming photon.

Raman and Brillouin scattering are examples of inelastic scattering in which part of the energy is conveyed to the medium. They originate from the interaction of the light with phonons (vibration of the crystal). In particular, Raman scattering involves optical phonons while Brillouin acts on acoustical ones. The incoming light interplays with the vibrational and rotational energy levels of the medium losing or gaining energy which is usually dissipated in heat. In figure 2.11 Raman scattering is compared to Rayleigh scattering. Stokes scattering is a specific case in which the light at the output has lower energy compared to the one at the input (and it is more probable since the medium can be in the ground state) while anti-Stokes scattering happens in the opposite situation, being therefore less probable since it requires the medium to be already pre-excited to some extent (as in figure 2.11 it is already in the 1st vibrational state before the arrival of the photon) [34].

Finally, Compton scattering refers to the clash between a photon and a charged particle, usually an electron [35]. As in the case of Rayleigh and Brillouin scattering, it can entail a red shift of the light or, in the unlikely inverse case, an increase in the photon energy.

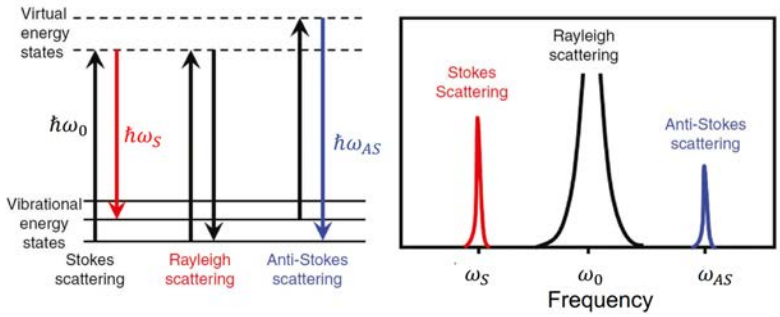


Figure 2.11: *Raman and Rayleigh scattering* [18]

## 2.10 Nonlinear effects

With reference to linear media, as described in section 2.1.1, the electric displacement field vector can be written as [19]

$$\bar{D}(\bar{r}) = \varepsilon_0 \bar{E}(\bar{r}) + \bar{P}(\bar{r}) = \varepsilon_0(1+\chi)\bar{E}(\bar{r}) = \varepsilon_0 \varepsilon_r \bar{E}(\bar{r}) \tag{2.47}$$

Where $\bar{P}(\bar{r}) = \varepsilon_0 \chi \bar{E}(\bar{r})$ is called polarization density (or polarization) and it expresses the density of permanent or induced electric dipole moments in a given dielectric material. $\chi = \varepsilon_r - 1$ is the electrical susceptibility, which shows how much the medium reacts to the applied field in terms of position, orientation and shape of the molecules.

It is found, however, that the polarization density is not a linear function of the electric field which is more precisely described by a Taylor series expansion as in

$$\bar{P}(\bar{r}) = \varepsilon_0 \chi^{(1)} \bar{E}(\bar{r}) + \varepsilon_0 \chi^{(2)} \bar{E}^2(\bar{r}) + \varepsilon_0 \chi^{(3)} \bar{E}^3(\bar{r}) + ... \tag{2.48}$$

Where the n-th order nonlinear optical susceptibility $\chi^{(n)}$, which depends on the specific material, is a tensor that usually becomes smaller as $n \to +\infty$ being therefore negligible except for extremely high power densities. For this reason no practical nonlinear effect had been studied before the advent of the laser in the 60s [36]. The nonlinear processes that can be described by equation (2.48) are also called parametric. The word parametric denotes a process in which the initial and final quantum-mechanical states of the system are identical (and therefore ruling out phenomena such as emission or absorption) and they pertain the real part of the refractive index (see section 3.6) [37]. Furthermore, energy and momentum are always conserved (since no energy is transferred to the medium) [37]. This last requirement results in a tight constraint called phase matching ($\Delta E = 0$, $\Delta \bar{k}(\bar{r}) = 0$) and is shown in figure 2.13. When not in the phase matching condition, the likelihood of a

parametric nonlinear process to take place rapidly plummets. Normal media cannot achieve such a condition because of dispersion (see section 3.4) and as a consequence birefringent materials are used instead. Birefringence means that the refractive index is dependent on the polarization and direction of the incoming light (it is also called anisotropy, see 2.1.1).

Among the most important nonlinear effects are the Pockels effect and the Kerr effect. These phenomena refer to the distortion of the position, orientation and shape of molecules and electron clouds of the crystal, creating electric dipoles. The refractive index can be written as a function of the electric field (only the amplitude matters and it will thus be simply denoted as the scalar $E$) [33]:

$$n(E) = n_0 - \frac{1}{2}\mathcal{P}n_0^3 E - \frac{1}{2}\mathcal{K}n_0^3 E^2 - ... \tag{2.49}$$

Here $\mathcal{P}$ [m/V] represents the Pockels effect while $\mathcal{K}$ [$m^2/V^2$] stands for the third order nonlinearity named Kerr effect. Higher order parameters are usually not considered since they are generally negligible. In particular, we have that $\mathcal{P} = -\frac{\chi^{(2)}}{n_0^4}$ spans from $10^{-14}$ to $10^{-12}$ m/V while $\mathcal{K} = -\frac{\chi^{(3)}}{n_0^4}$ ranges from $10^{-18}$ to $10^{-14}$ $m^2/V^2$ [33], [38]. It is immediately noticeable that the Pockels effect is exceedingly more effective at modulating the refractive index since it is a lower order nonlinearity. However, while dealing with centrosymmetric materials (such as silicon), $n(E)$ must be an even-symmetric function since invariance to the reversal of $E$ is required and therefore they only react to the square of the applied field [38]. Pockels effect is commonly used in optical modulators (see section 4.3.2).

Directly stemming from the Kerr effect, another nonlinear effect called self-focusing takes place when the power density is extremely high [39]. Following equation (2.49), the refractive index increases with the electric field in the case of positive $\chi^{(3)}$. Neglecting the Pockels effect, we can write

$$n(I) = n_0 + n_2 I \tag{2.50}$$

With $n_2 = \frac{\chi^{(3)}}{2n_0}$ called second-order nonlinear refractive index.

As it is thoroughly explained in 3.2, the light tends to be confined in the medium with the higher refractive index and therefore a positive feedback is established. In fact, when the light beam starts converging towards its axis due to the Kerr effect the field intensity snowballs inducing an even greater converging rate.

Self-Phase Modulation (SPM) occurs in media subjected to self-focusing. In figure 2.12 a Gaussian ultrashort light pulse is shown. SPM affects the frequency of the pulse, namely the front shifts towards lower frequencies and

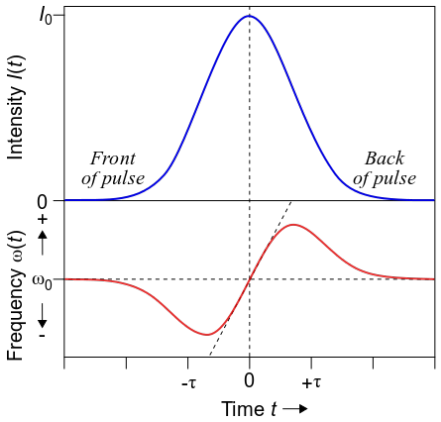


Figure 2.12: *SPM in the case of a Gaussian pulse*

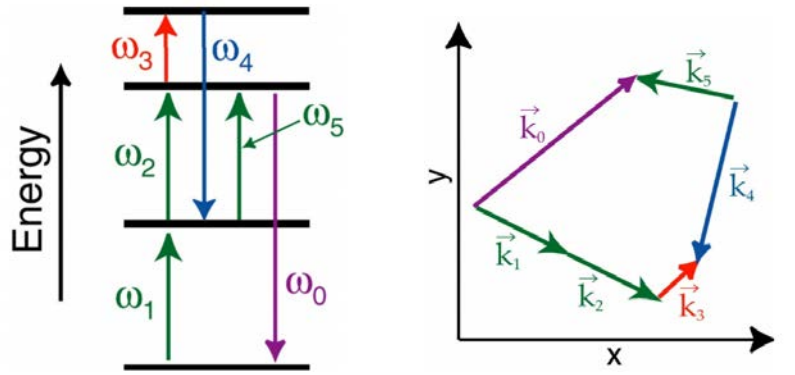


(a) $\omega_1 + \omega_2 + \omega_3 - \omega_4 + \omega_5 = \omega_0$ (b) $\bar{k}_1 + \bar{k}_2 + \bar{k}_3 - \bar{k}_4 + \bar{k}_5 = \bar{k}_0$

Figure 2.13: *Complex six-waves mixing process and phase-matching conditions: energy (a) and momentum (b)* [40]

the back towards higher ones while the peak (the center of the Gaussian shape) remains unchanged.

Another important category of nonlinear effects is called frequency mixing. In this case, the input light (monochromatic or not) interacts with the medium via "virtual" energy levels and recombines creating light at different frequencies, as can be seen in figure 2.13.

Among the most important three-wave mixing processes (entailing only $\chi^{(2)}$ and therefore extremely more probable than four- ($\chi^{(3)}$) or n-wave mixing ($\chi^{(n-1)}$)) we have the Difference-Frequency Generation (DFG) shown in figure 2.14 and the Sum-Frequency Generation (SFG) depicted in figure 2.15. The latter is also called Second-Harmonic Generation (SHG) in the specific case

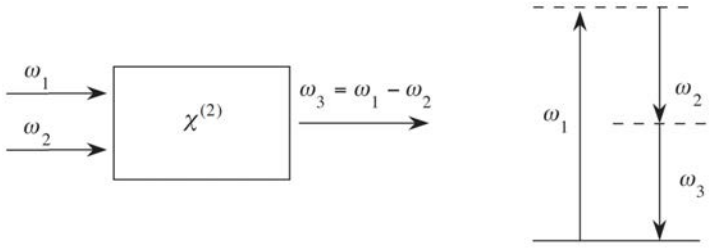


Figure 2.14: *Difference-Frequency Generation* [41]

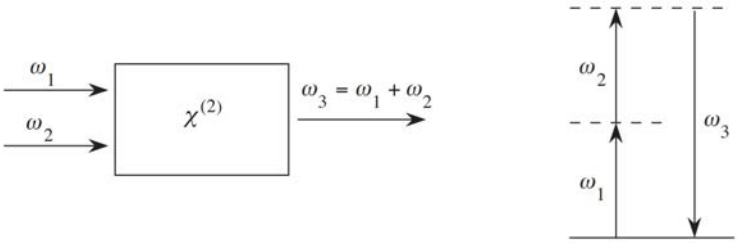


Figure 2.15: *Sum-Frequency Generation* [41]

in which $\omega_1 = \omega_2 = \omega$.

Another nonlinear effect takes place when Raman and Brillouin scattering are stimulated by injecting light at the right frequency (the difference between the phonon and the signal energy). This gives rise to third-order nonlinear effects based on $\chi^{(3)}$ which are employed in spectroscopy and light amplification.

Finally, a non-parametric process is presented. Two-Photon Absorption (TPA) occurs when two photons (of the same or different energy) are absorbed simultaneously in order to excite an electron to a higher energy level which is the sum of the energies of the two individual photons. Since it requires two photons, its likelihood is not comparable to the regular single-photon absorption. The effect is based on the imaginary part of $\chi^{(3)}$ (since it involves absorption) and as such it is not parametric [42]. TPA can cause unwanted attenuation of the light even in media that are presumed to be invisible to the light and has therefore to be avoided.

# Chapter 3

# Propagation in Dielectric Media

## 3.1 Boundary conditions

When an electromagnetic wave crosses two different regions as depicted in figure 3.1, some boundary conditions must be fulfilled in order to connect the fields in the two areas. These are directly derived from Maxwell's equations and show [18]

$$\hat{n} \times (\bar{E}_2 - \bar{E}_1) = 0 \tag{3.1}$$

$$\hat{n} \times (\bar{H}_2 - \bar{H}_1) = \bar{J}_s \tag{3.2}$$

$$\hat{n} \cdot (\bar{D}_2 - \bar{D}_1) = \sigma_s \tag{3.3}$$

$$\hat{n} \cdot (\bar{B}_2 - \bar{B}_1) = 0 \tag{3.4}$$

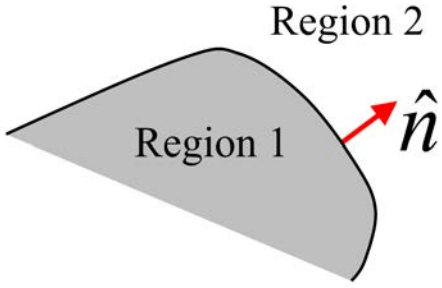


Figure 3.1: *Boundary between two different regions 1 and 2. $\hat{n}$ is always normal to the border* [18]

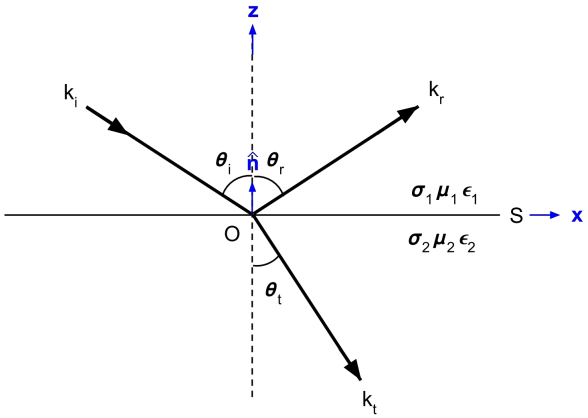


Figure 3.2: *Light incident to an interface, reflection and refraction. $\hat{y}$ is considered orthogonal to the plane $\hat{x} - \hat{z}$* [43]

Where $\bar{J}_s$ and $\sigma_s$ are the surface current density and the surface charge density at the boundary respectively. In absence of charges and currents, these conditions require both the tangential components of the electric and the magnetic field to be continuous ($\bar{E}_{t1} = \bar{E}_{t2}$, $\bar{H}_{t1} = \bar{H}_{t2}$), as well as the normal electric and magnetic displacement ($\bar{D}_{n1} = \bar{D}_{n2}$, $\bar{B}_{n1} = \bar{B}_{n2}$).

## 3.2 Snell's Law

The propagation of light through dielectric media is made possible by a property called Total Internal Reflection (TIR), which is a particular condition stated by Snell's Law. A reflection involves a modification of the direction of the wave propagation due to a variation in the refractive index (and consequently in the speed of propagation, see section 2.1.2). When the so-called incident (incoming) light hits an interface S between two different media of refractive indices $n_1$ and $n_2$, part of it is reflected and the remaining transmitted (refracted), as can be seen in figure 3.2.

Since in the case of incident and reflected light the medium is the same, the two angles $\theta_i = \theta_t$ are equal (and therefore it is also called specular reflection).

Snell's Law states that

$$n_1 \sin(\theta_i) = n_2 \sin(\theta_t) \tag{3.5}$$

TIR occurs when $\theta_t$ becomes 0, meaning that $\sin(\theta_t) = 1$, yielding

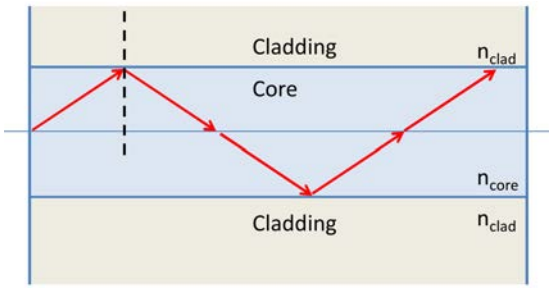


Figure 3.3: *Waveguide propagation* [44]

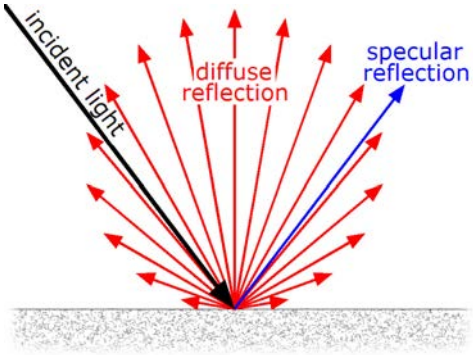


Figure 3.4: *Specular and diffuse reflection* [45]

$$\theta_C = \arcsin(\frac{n_2}{n_1}) \tag{3.6}$$

When the incidence angle $\theta_i$ exceeds the critical angle $\theta_C$ there is no transmission of light which is all bounced again into the first medium. The more $n_1$ is larger than $n_2$ the smaller the critical angle is, allowing larger amounts of light to be completely reflected, as in figure 3.3.

It is important to notice, however, that specular reflection (calculated via Snell's law) occurs only with smooth surfaces, such as mirrors or polished glass. When the surface is rough and the imperfections have size larger than the wavelength, diffuse reflection takes place. In this case, the light is backscattered in all directions (see section 2.9), as depicted in figure 3.4. As a consequence, polished surfaces are extremely important to maintain control over light propagation and avoid losses, as discussed in more detail further on (see section 5.2.2).

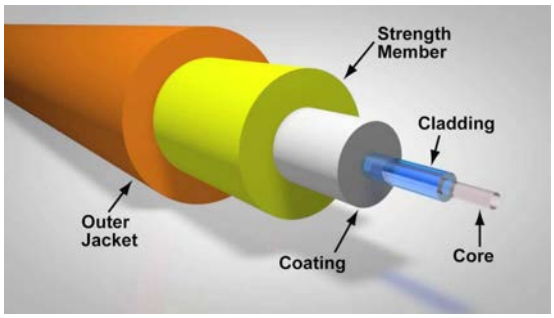


Figure 3.5: *Typical optical fiber cable* [50]

## 3.3 Waveguides

### 3.3.1 Introduction and materials

By employing the TIR effect it is therefore possible to obtain light propagation in a certain direction provided that the incident angle is small enough and that the propagation (active) region (the core) has a higher refractive index compared to the enveloping one (the cladding) which transversely surrounds the core. Once these conditions are met, light is effectively piped and channeled. Different materials and shapes have been successfully employed for light transmission.

For instance, optical fibers (figure 3.5) have been utilized since the 80s due to their inherent advantages over copper. Among the others, an extremely high bandwidth together with strikingly low intrinsic losses (down to 0.2 $^{\mathrm{dB}}/_{\mathrm{cm}}$ in the C-band) [46]. Moreover, they are impervious to electromagnetic interference, lightweight and durable [46]. For these reasons, the replacement of common copper wires with optical links is taking place in Fiber-To-The-Home (FTTH) broadband network architectures to ensure better Internet connections to customers [47]. Optical fibers are commonly made of silicon dioxide ($SiO_2$) with a slight doping in the core in order to ensure a small $\Delta n = n_{co} - n_{cl}$ (in the case of 1550 nm light, $n_{co} \simeq 1.466$ and $n_{cl} \simeq 1444$, with a difference of $\simeq 1.5\%$ [33]), but when top notch performances are not required, as in the case of low-speed, short-reach applications, Plastic Optical Fibers (POFs) are preferable in virtue of their lower cost [48], [49].

However, the core can also be made of silicon ($Si$), whose refractive index is exceedingly larger ($\simeq 3.47$). Nowadays silicon photonics is growing in popularity since it allows the integration of both electronic and photonic components in the same device by employing well-established and efficient lithographic techniques. Thus, it results in smaller footprints and less expen-

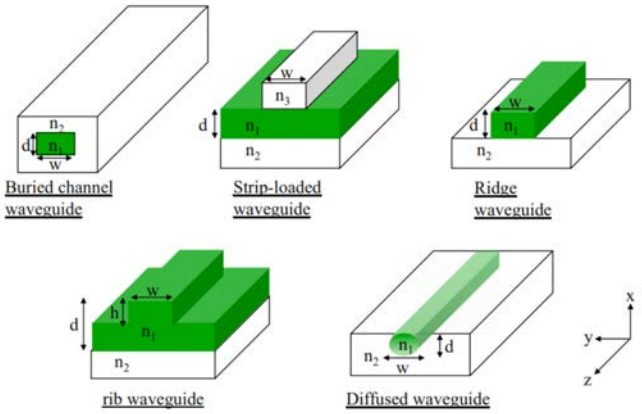


Figure 3.6: *Different silicon waveguides. The green volume is the core* [51]

sive products [1]. Different configurations have been used in the industry. The main ones are summarized in figure 3.6.

### 3.3.2 Optical modes

When considering waveguides, the propagation of light is not alike the case studied in section 2.1 because the medium cannot be considered homogeneous. In particular, the solutions of Maxwell's equations satisfying all the boundary conditions for a certain waveguide are called guided optical modes, such that their spatial distribution does not change while propagating along the longitudinal direction ($\hat{z}$ in figure 3.6). Each mode has its distinct phase velocity, group velocity, cross-sectional intensity distribution and polarization. The characteristics of a waveguide are determined by the transverse profile of its refractive index along the physical dimensions $h, w$ and $d$ as in figure 3.6, while they do not depend on the longitudinal coordinate $\hat{z}$. A further simplification can be made in the case of planar (2D) waveguides, in which the optical confinement occurs only in one transverse direction, the other being extended enough to be considered infinite for practical purposes. In the case of regular non-planar (3D) waveguides (such as optical fibers), the confinement takes place in both the transverse directions, such that the refractive index is written as $n(x, y)$. The electric and magnetic field of a particular mode as regards monochromatic light can be written as

$$\bar{E}_m(\bar{r}) = \bar{E}_{0m}(x, y)e^{i\beta_m z} \tag{3.7}$$

$$\bar{H}_m(\bar{r}) = \bar{H}_{0m}(x, y)e^{i\beta_m z} \tag{3.8}$$

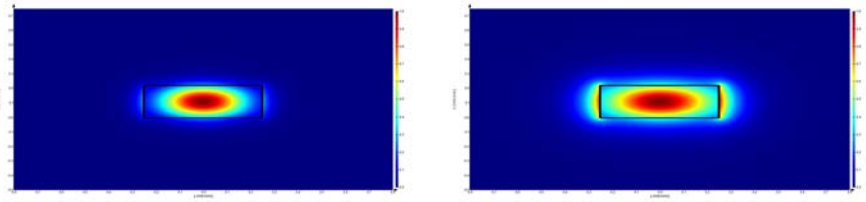

(a) Strong confinement (b) Weak confinement

Figure 3.7: *Comparison between strong (left) and weak (right) confinement for a silicon waveguide. Image processed using Lumerical*

Where $E_{0m}(x,y)$ and $H_{0m}(x,y)$ are the mode field profiles in the cross section of the waveguide, $m$ is the mode index and $\beta_m = \frac{2\pi n_{eff,m}}{\lambda}$ is the propagation constant which can be considered as the propagation vector $\bar{k}$ when dealing with unguided radiation in a homogeneous medium. The refractive index varies along the transverse coordinates, but it is possible to consider an effective refractive index $n_{eff}$ acting as a sort of weighted average calculated along the transverse directions. The averaged index is bounded by $n_2, n_3 < n_{eff} < n_1$, being $n_2$ and $n_3$ the refractive indices of the cladding regions (a particular situation is found when $n_2 = n_3$, in which case the waveguide is called symmetric) and $n_1$ is the refractive index of the core. In particular, if $n_{eff} \simeq n_1$, the mode is said to be tightly confined, while when $n_{eff} \simeq n_2, n_3$ it is weakly confined, as shown in figure 3.7. In fact, since the wave is not point-like but is instead extended over space, it is not entirely contained in the core. The overlap with the cladding cannot be neglected, such that the structure cannot be considered homogeneous. The percentage of the electromagnetic radiation which is flowing in the core is represented by the confinement factor $\Gamma$, defined as

$$\Gamma \triangleq \frac{P_{core}}{P_{total}} = \frac{\iint_{core} |E_{0m}(x,y)|^2 \, \partial x \partial y}{\iint_{-\infty}^{\infty} |E_{0m}(x,y)|^2 \, \partial x \partial y} \tag{3.9}$$

Usually, high order modes are less confined in the waveguide, resulting in a smaller $n_{eff}$. The concept of modes pertains the spatial distribution of the fields inside the waveguide and as such they are also polarization-dependent, being them TE, TM or HEM. Examples of TE and TM modes are shown in figure 3.8. In a real case scenario, however, no pure TE or TM modes can be retrieved and they are therefore referred as quasi-TE and quasi-TM modes.

Examples of modes propagating in an optical fiber are displayed in figure 3.9. It is immediately noticeable that when the order of the mode increases, so does the complexity of the field spatial distribution, with increasing number

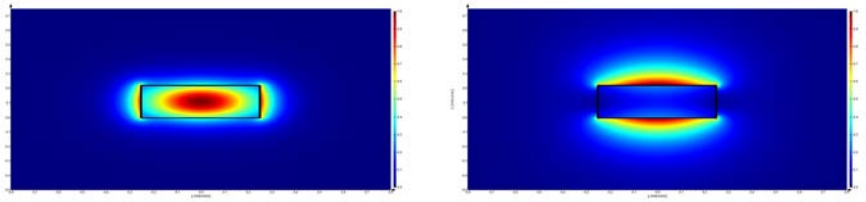

(a) TE polarization (b) TM polarization

Figure 3.8: *Comparison between TE (left) and TM (right) polarization for a silicon waveguide. Image processed using Lumerical*

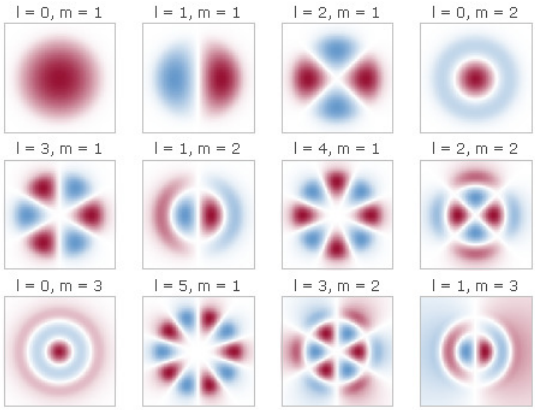


Figure 3.9: *$LP_{lm}$ modes in an optical fiber. As $l$ and $m$ increase, so does the number of nodes (points in which the field drops to zero, the white areas). $l$ refers to the transverse behavior of the mode, $m$ to its concentric shape* [52]

of points of maxima and minima.

The lateral distribution of the modes propagating in a waveguide is plotted in figure 3.10. It is possible to distinguish the nodes when the field amplitude drops to zero.

Since the concept of optical modes refers to a spatial distribution of the fields, they are greatly affected by the physical dimensions of the waveguide. In figure 3.11 the effective refractive index of different modes is drawn compared to the width of the waveguide. It can be seen that if the waveguide is too narrow they are not excited (1.44 is the lowest value of the effective refractive index such that the mode is confined within the waveguide).

It is possible to derive an analytical expression for the number of modes propagating in a silicon waveguide [54]. Let us define a dimensionless parameter

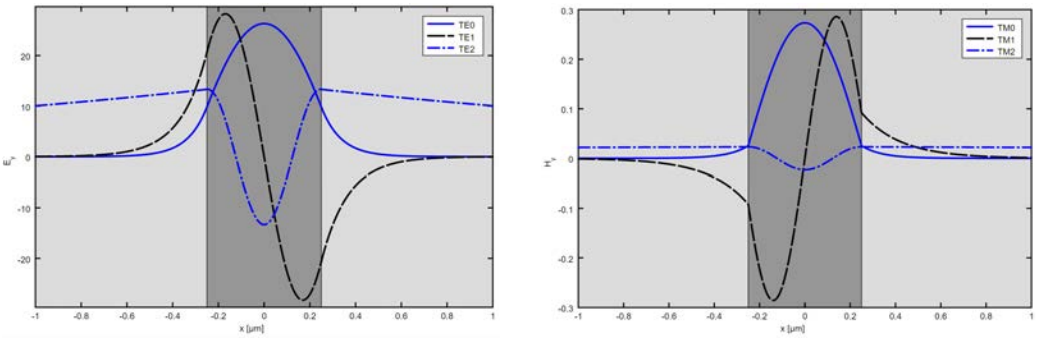


(a) TE modes (b) TM modes

Figure 3.10: *Lateral field distribution of the first three modes in the case of a symmetric planar waveguide ($n_1 = 3.45$, $n_2 = n_3 = 1.45$)* [53]

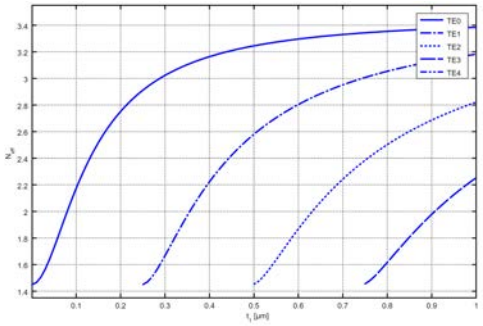


Figure 3.11: *TE modes and their effective refractive index versus waveguide width* [53]

$$\delta \triangleq \frac{n_3^2 - n_2^2}{n_1^2 - n_3^2} = \frac{n_3^2 - n_2^2}{NA} \tag{3.10}$$

Where $NA$ is called numerical aperture. The parameter provides a measure of the waveguide symmetry, being 0 if $n_3 = n_2$. In addition, to calculate the amount of non-radiating modes, one needs to define the V-number (also called normalized frequency) so that

$$V \triangleq \frac{2\pi}{\lambda} d\sqrt{NA} \tag{3.11}$$

And a reference parameter $V_m$ that is

$$V_m = \frac{m\pi}{2} + \frac{1}{2}\tan^{-1}(\sqrt{\delta}) \tag{3.12}$$

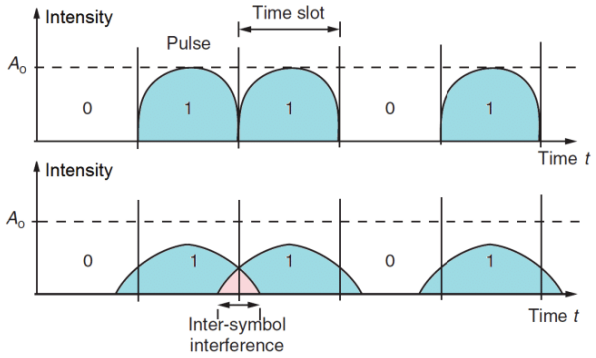


Figure 3.12: *Intersymbol interference* [55]

$$V_m = \frac{m\pi}{2} + \frac{1}{2}\tan^{-1}\left(\frac{n_1^2}{n_3^2}\sqrt{\delta}\right) \tag{3.13}$$

Where relation (3.12) is valid in the case of TE polarization, while relation (3.13) is valid with TM polarization.

Moreover, the number of allowed mode is the largest value of $m$ for which $V_m < V$. As a result, as regards symmetric silicon waveguides ($\delta = 0$) there will only be one mode propagating as long as $V < \frac{\pi}{2}$.

With reference to optical fibers (whose core is made of silicon dioxide), the condition to have monomodal propagation is $V < 2.405$ [33].

## 3.4 Dispersion

Dispersion, also known as pulse broadening, is a phenomenon that takes place in every dielectric medium and results in the spread of the input optical pulse in the time domain after covering the channel distance. It is due to the dependence of the propagation constant on different parameters, such as the optical mode considered (modal dispersion), the specific wavelength (chromatic dispersion) or the polarization of the wave (polarization mode dispersion). Dispersion will ultimately reduce the bandwidth of a transmission link because, when considering a stream of bits, spreading the pulses means creating an overlap with the adjacent bit to the point where the two are no more distinguishable, which requires a relaxation of the bitrate. This occurrence is called InterSymbol Interference (ISI) and can be visualized in figure 3.12.

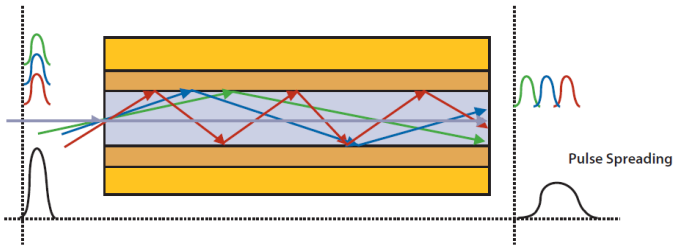


Figure 3.13: *Modal dispersion* [56]

### 3.4.1 Modal dispersion

Modal dispersion is the expression used to underline that the propagation of light inside a waveguide depends on the particular mode which is excited. In fact, as stated in section 3.3.2, distinct modes have dissimilar levels of confinement leading to different propagation constants which are related to the separated paths that these modes travel in the waveguide, as can be seen in figure 3.13. The red mode has a lower propagation constant since it is more skewed and the optical length is increased. As a consequence, at the end of the channel it is received after the green and blue ones, therefore spreading the signal in time. Modal dispersion is especially present in optical fibers and can be limited by engineering the refractive index profile of the medium [33] or by employing single-mode devices.

### 3.4.2 Chromatic dispersion

So far in chapter 3 only monochromatic light sources have been considered. However, real life signals are made of pulses comprising a wide range of frequencies (see section 2.6). As already anticipated in section 2.5, every medium responds differently to light of different colors. This property is called dispersion (as introduced in section 2.1.1).

Let us consider a generic signal in the frequency domain and a certain optical channel used to transmit the pulse, as [33]

$$S_{OUT}(\omega) = H(\omega)S_{IN}(\omega) \tag{3.14}$$

Where $S_{IN}(\omega)$ is the signal at the beginning of the channel, $S_{OUT}(\omega)$ is the signal at the end of the channel while $H(\omega) = A_0 e^{i\varphi(\omega)}$ is the transfer function of the channel, such that $A_0$ is mainly related to the attenuation and $e^{i\varphi(\omega)}$ represents the phase. Thus, in the time domain we have (Fourier transform)

$$S_{OUT}(t) = \int_{-\infty}^{\infty} S_{OUT}(\omega)e^{-i\omega t}d\omega = \int_{-\infty}^{\infty} A_0 S_{IN}(\omega)e^{i\varphi(\omega)}e^{-i\omega t}d\omega \tag{3.15}$$

By taking the Taylor expansion of the phase when considering the central frequency $\omega_0 = 0$ in order to focus only on the behavior around it (base-band approach), the phase becomes

$$\varphi(\omega) \simeq \varphi(0) + \omega\frac{d\varphi(\omega)}{d\omega} \mid_{\omega=0} + \frac{1}{2}\omega^2\frac{d^2\varphi(\omega)}{d\omega^2} \mid_{\omega=0} + ... \tag{3.16}$$

Such that

$$S_{OUT}(t) = A_0 \int_{-\infty}^{\infty} S_{IN}(\omega)e^{i\varphi_0}e^{i\omega\varphi_1}e^{i(\frac{1}{2}\omega^2\varphi_2)}...e^{-i\omega t}d\omega \tag{3.17}$$

Where $\varphi_0 = \varphi(0)$ is the first order term, $\varphi_1 = \frac{d\varphi(\omega)}{d\omega}$ [s] is the second order term, $\varphi_2 = \frac{d^2\varphi(\omega)}{d\omega^2}$ [$s^2$] is the third order term (which represents dispersion) and so on and so forth. When the transmission distance is short or the bandwidth really small it is possible to stop at the first term, obtaining [33]

$$S_{OUT}(t) = A_0 \int_{-\infty}^{\infty} S_{IN}(\omega)e^{i\varphi_0}e^{-i\omega(t-\varphi_1)}d\omega = A_0 e^{i\varphi_0}S_{IN}(t-\varphi_1) \tag{3.18}$$

$\varphi_1$ is also called group delay ($\tau_g$) because it represents the amount of time that the signal needs to completely traverse the link. In this case the Heaviside non-distortion conditions hold true because the pulse only experiences attenuation and phase changes [57], maintaining its shape throughout the entire channel.

However, when transmitting over long distances or when short pulses are considered, the previous approximation is no longer valid and $\varphi_2 = \frac{d\tau_g}{d\omega}$ has to be introduced [33]. In particular, by writing $\varphi(\omega) = \beta(\omega)z$ with $z$ length of the channel and $\beta(\omega)$ propagation factor dependent on the wavelength, one obtains

- $\tau_g = \frac{d\varphi(\omega)}{d\omega} = \frac{d\beta(\omega)}{d\omega}z$, meaning that the group delay increases linearly with distance;
- $v_g = \frac{z}{\tau_g} = \frac{1}{d\beta(\omega)/d\omega}$ [m/s] is the velocity at which the signal propagates through the channel;

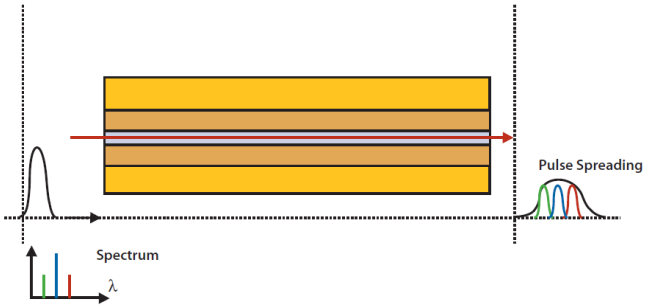


Figure 3.14: *Chromatic dispersion* [58]

- $\varphi_2 = \frac{d^2\varphi(\omega)}{d\omega^2} = z\frac{d^2\beta(\omega)}{d\omega^2} = \beta_2 z$ where $\beta_2$ $[^{s^2}/_{m}]$ is the chromatic dispersion coefficient per unit length (also called Group Velocity Dispersion (GVD)).

Therefore different wavelengths travel at different velocities inside the waveguide, resulting in a broadened output pulse, as can be seen in figure 3.14.

Furthermore, it is possible to write the propagation constant as

$$\beta(\omega) = n_{eff}(\omega)\frac{\omega}{c} \tag{3.19}$$

Where $n_{eff}(\omega)$ represents the response of the medium to the specific frequency, such that in figure 3.15 the so-called dispersion diagram ($\beta(\omega)$ versus $\omega$) for a generic symmetric waveguide is retrieved. Here $n_2$ represents the refractive index of the core while $n_3$ that of the cladding. The two solid black lines stand for the linear response of the propagation vector to the frequency while the red one takes alos into consideration the nonlinear variation of the effective refractive index. The figure shows how long wavelengths are overlapping further with the cladding (and consequently their effective refractive index is lower) while short wavelengths are more tightly confined resulting in larger effective refractive indices (a concept similar to those explored in section 3.3.2 regarding the propagation difference between distinct modes [1]).

### 3.4.3 Polarization mode dispersion

Polarization Mode Dispersion (PMD) arises in optical fibers when they do not have a perfectly circular core cross-section. Random imperfections due to the fabrication process alter the propagation of the light accordingly to its polarization, since the fields react to every small alteration of the physical

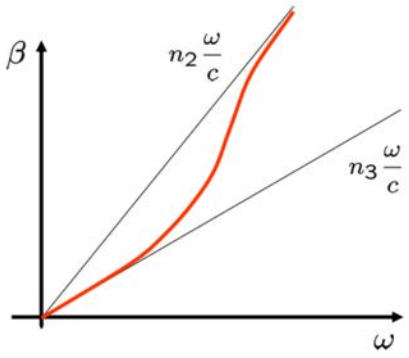


Figure 3.15: *Dispersion diagram* [51]

structure of the medium they are travelling in. Hence, two different polarizations will result in slightly different propagation constants which in turn will lead to an expansion of the pulse at the receiving end [54].

## 3.5 Coupling

As seen in section 3.3, the optical mode is not entirely confined in the core and as a result the light leaking in the cladding can be coupled to that of a different waveguide (cross-talking). When the optical pulse tails interact, the so-called optical modes are created. The two waves are no longer single entities but they have to be considered as a whole new system.

Let us consider the simple case of two straight waveguides. In figure 3.16 on the left the two waveguides are not coupled (it happens when the gap is large) while on the right an even ($E$, green in the figure) and an odd ($O$, red in the figure) supermode are created. These two supermodes compose a linear combination of the pulses in the single waveguides.

In particular, the pulse number 1 (in the decoupled waveguides case) can be written as $E + O$ while the pulse number 2 (again in the decoupled waveguides case) as $E - O$. These two supermodes are symmetric around the waveguide axis (which will be called $\hat{z}$, while the orthogonal plane will be defined by $\hat{x}$ and $\hat{y}$) and their propagation constants are slightly different, such that $\beta_E \neq \beta_O$. The smaller the gap, the more the two constants are different, while as regards decoupling the two parameters will be identical.

The even supermode can be written as

$$\bar{E}_E(x,y,z) = \begin{cases} \xi(x,y)e^{-i\beta_E z} & \text{in 1} \\ \xi(x,y)e^{-i\beta_E z} & \text{in 2} \end{cases} \tag{3.20}$$

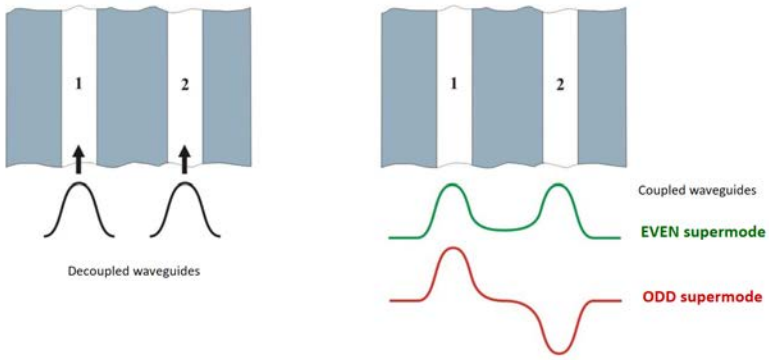


Figure 3.16: *Decoupling (left) and coupling (right)* [33]

While the odd is

$$\bar{E}_O(x,y,z) = \begin{cases} \xi(x,y)e^{-i\beta_O z} & \text{in 1} \\ -\xi(x,y)e^{-i\beta_O z} & \text{in 2} \end{cases} \tag{3.21}$$

Consequently, the field in a generic position along $\hat{z}$ is [33]

$$\bar{E}_T(z) = a_E\bar{E}_E(z) + a_O\bar{E}_O(z) \tag{3.22}$$

With $a_E$ and $a_O$ balancing coefficients which depend on the pulse first sent through the coupled system. Consider the case in which no light is sent through 2, obtaining $a_E = a_O = 1$.

Thus, the total field is

$$\bar{E}_T(z) = \bar{E}_E(z) + \bar{E}_O(z) = \begin{cases} \xi(x,y)\{e^{-i\beta_E z} + e^{-i\beta_O z}\} & \text{in 1} \\ \xi(x,y)\{e^{-i\beta_E z} - e^{-i\beta_O z}\} & \text{in 2} \end{cases} \tag{3.23}$$

Which, after defining $\Delta\beta = \frac{\beta_E - \beta_O}{2}$ and $\beta_A = \frac{\beta_E + \beta_O}{2}$, becomes

$$\bar{E}_T(z) = \begin{cases} \xi(x,y)e^{-i\beta_A z}\{e^{-i\Delta\beta z} + e^{i\Delta\beta z}\} = 2\xi(x,y)\cos(\Delta\beta z)e^{-i\beta_A z} & \text{in 1} \\ \xi(x,y)e^{-i\beta_A z}\{e^{-i\Delta\beta z} - e^{i\Delta\beta z}\} = -2i\xi(x,y)\sin(\Delta\beta z)e^{-i\beta_A z} & \text{in 2} \end{cases} \tag{3.24}$$

In particular, it is possible to notice that the two components are 90° out of phase (because of the $i$ factor) and that in the case of decoupled waveguides ($\Delta\beta = 0$) there is no light propagating in 2.

As a result, the total power can be written as

$$P = |\bar{E}_T(z)|^2 \propto \begin{cases} \cos^2(\Delta\beta z) & \text{in 1} \\ \sin^2(\Delta\beta z) & \text{in 2} \end{cases} \tag{3.25}$$

The optical power is therefore flowing from one waveguide to the other, even if the light is only launched in one of them.

## 3.6 Attenuation

In a waveguide the light always experiences losses (see section 2.2). Let us take a waveguide section of length $\Delta z$ and calculate the optical power drop along this portion of the channel. One can write [33]

$$P(z + \Delta z) = P(z) - \alpha \Delta z P(z) \tag{3.26}$$

Where $\alpha$ is the attenuation coefficient (see section 2.2). In dB it is $\alpha_{dB} = 10 \log_{10}(e) \cdot \alpha = 4.343\alpha$ [$^{\text{dB}}/_{\text{m}}$] [51]. After approximating it becomes

$$P(z + \Delta z) \simeq P(z) + \frac{dP(z)}{dz} \Delta z \tag{3.27}$$

Yielding

$$\frac{dP(z)}{dz} = -\alpha P(z) \tag{3.28}$$

Which can be solved as

$$P(z) = P(0)e^{-\alpha z} \tag{3.29}$$

With $P(0)$ the initial power injected in the waveguide.

In particular, the attenuation coefficient comprises the loss due to absorption (see section 2.8), scattering (see section 2.9) and impurities which are always present in the waveguide, no matter the accuracy of the fabrication process.

The loss can be contained in the refractive index by considering also its imaginary part, as in $\underline{n} = n + ik$ where $k$ is called extinction coefficient and it represents the loss. In this case it is possible to write [59]

$$\alpha = \frac{4\pi k}{\lambda} \tag{3.30}$$

# Chapter 4

# Modulators

Modulators are important devices in photonics and as such they are also paramount in silicon photonics. Their main feature is the ability to turn a light signal on and off in order to convey a sequence of bits and as a result they allow digital communications. In this chapter, at first an outline of the concept is drawn. Afterwards, the Mach-Zehnder Modulator (MZM) is presented and the main modulating techniques are shown and explained. Finally, some of the most important modulator parameters are listed.

## 4.1 Introduction

Modulation is of crucial importance in telecommunications since it is the backbone of every digital communication. It consists in altering the signal at the transmitter so that the receiver can distinguish between different states and recreate the original message. Different kinds of digital modulation are possible. For instance, in the case of Amplitude-Shift Keying (ASK) the data is represented as variations in the amplitude of a carrier wave. When the modulation regards the frequency, meaning that the information is transmitted through discrete frequency changes of the carrier, the modulation is called Frequency-Shift Keying (FSK). The third major class of digital modulation techniques entails a series of changes in the phase of the signal, leading to the so-called Phase-Shift Keying (PSK).

In optical communications, though, the modulation is mostly binary, meaning that the signal is either "on" or "off", reproducing the bits "1" and "0" respectively. The most employed technique is called On-Off Keying (OOK) which represents the simplest form of the ASK modulation. "On" means that the light is sent while "off" means the lack of the signal [60].

The data is usually sent by means of a laser, whose focused and coherent

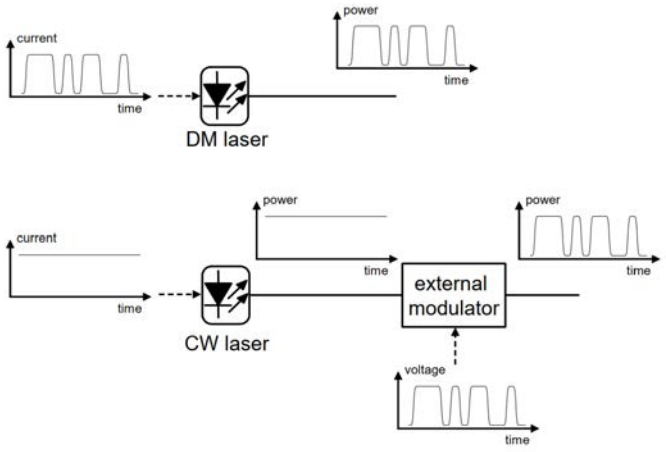


Figure 4.1: *Direct and external modulation of the laser source* [61]

light allows long-haul communication links over optical fibers without the need to restore the optical signal repeatedly [33]. In order to modulate the data, it is possible to work directly on the laser, meaning changing its injection level, or to rely on an additional component which constructs the flow of bits while the laser is kept at a steady state. The former is called direct modulation while the latter is named external modulation (figure 4.1).

The main drawback of employing an external modulation is the greater complexity of the system due to the presence of a second device which increases the footprint and it is not always directly built on the laser chip. However, direct modulation entails more numerous and serious downsides. For starting, the laser needs some time to adjust to the driving signal, meaning there will be a certain transient regime which ultimately bounds the bitrate to less than 10 Gbps [61]. Two are the possibilities: if the zero level is put above the threshold, such that the diode is always kept in the lasing condition, there will be little distinction between the two states unless the current for the "on" level is extremely high; if the zero is put below the threshold instead, the device switching time will become dependent on the carrier spontaneous recombination time, which is exceedingly slow. In figure 4.2 this phenomenon can be understood by looking at the ripples of the transmitted signal which are due to the oscillations of the laser [62]. Another disadvantage of a directly-modulated laser is a phenomenon called chirp, which consists of small variations in the emitted spectrum over time for the same pulse (the frequency becomes time-dependent) and it is due to the slight change in the physical properties of the laser while varying the current [63].

As a result, external modulation is preferable in the vast majority of cases. The modulator receives a constant radiation level coming from the laser as

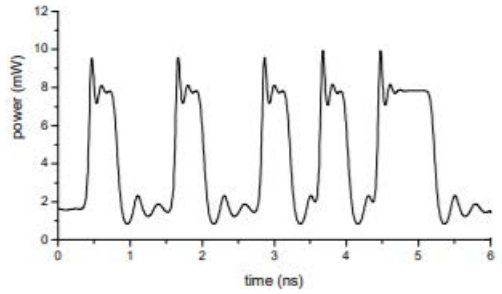


Figure 4.2: *Transient behavior of the laser under direct modulation* [61]

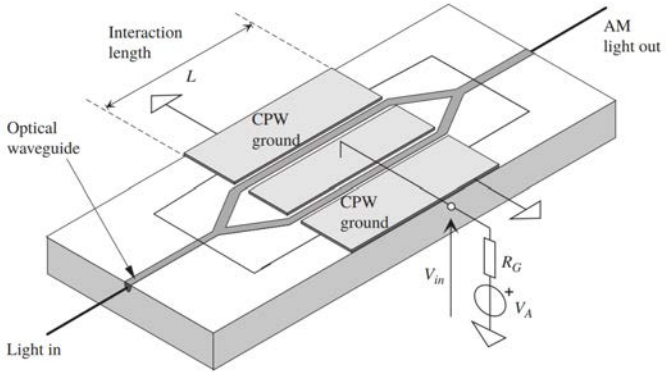


Figure 4.3: *Mach-Zehnder Modulator* [61]

the input and, taking as the driving signal a varying voltage, turns the light into a flow of bits.

## 4.2 Mach Zehnder Modulator

When considering external modulation, the most popular device employed is the MZM, which is sketched in figure 4.3. The MZM is a two-branches device such that the light after recombining is amplitude-modulated. The physical process behind is the destructive interference (see section 2.7): in the two branches the light undergoes a phase shift due to an applied voltage $\Delta\varphi(V)$ (the phase shift can be achieved with different techniques as further explained in sections 4.3.2 and 4.3.3) such that when the two flows reunite they are out of phase and cancel each other out.

The output power can be written as [64]

$$P_{OUT} = P_{IN}\cos^2(\Delta\varphi(V)) = P_{IN}\cos^2(\frac{\pi}{2}\frac{V}{V_\pi}) \tag{4.1}$$

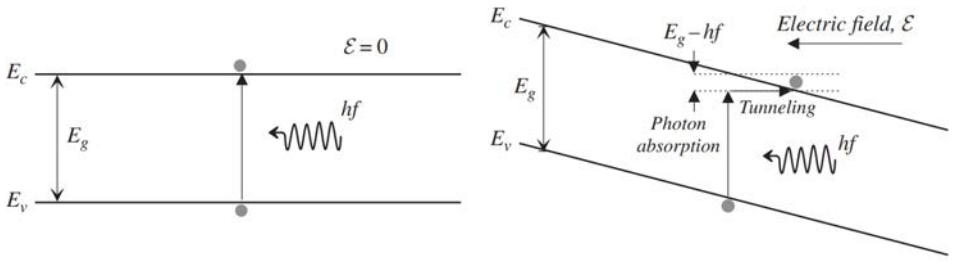


Figure 4.4: *Franz-Keldysh effect* [61]

Where the half-wave voltage $V_\pi$ is the voltage necessary to obtain a $\pi$ phase shift (and thus destructive interference) yielding a complete modulation of the signal. In fact, by switching the driving voltage from 0 to $V_\pi$ the output signal is brought to 0.

An improvement of the MZM of figure 4.3 is represented by the so-called push-pull configuration, in which the modulation occurs in both arms with opposite bias. The main advantages of this method are the lack of chirp and the reduction of $V_\pi$ [64]. Moreover, one of the two branches usually presents a small physical delay of $\Delta L$ to enhance the sensitivity [65].

## 4.3 Modulation techniques

Three are the main modulation techniques currently employed to cause a phase shift in the light signal by means of an applied voltage. They are listed below, together with a phenomenon which results in the variation of the optical signal but that is usually considered as noise.

### 4.3.1 Electro-absorption

Electro-absorption makes use of the so-called Franz-Keldysh effect. This effect takes place when an electric field is applied to a semiconductor. In band theory it is known that a bias bends the valence ($E_V$) and the conduction bands ($E_C$), as displayed in figure 4.4. Let us consider the case of a photon with slightly less energy compared to the energy gap ($E_G$). In standard conditions no absorption could take place since electrons and holes are too far apart in energy. However, when biased, a certain degree of overlap between the photon and the electron wavefunctions is retrieved, leading to a non-negligible absorption probability due to the tunnel effect (Fermi's golden rule [24]), which is larger the more the applied voltage [66].

This red-shift of the absorption band-edge makes the material turn from

transparent to absorbant for photons carrying the right amount of energy and consequently, by modulating the voltage applied, it is possible to reduce (ideally shut down) the light signal passing through a piece of semiconductor, therefore implementing the OOK modulation. As of 2018, the ER of such a modulator is around ∼10 dB [33]. The main advantage is that it can be directly integrated in the source and does not require a MZM since it is already an amplitude modulation, which is different from the next phenomena presented in 4.3.2 and 4.3.3. Moreover, it is not sensitive to polarization [33].

### 4.3.2 Electro-refraction

Electro-refraction is mainly based on the Pockels effect. By taking equation 2.49 and crossing the contribution due to the Kerr effect (which is significantly weaker) one obtains

$$n(E) = n_0 - \frac{1}{2}\mathcal{P}n_0^3 E \tag{4.2}$$

The propagation constant $\beta$ of a standard wave can therefore be written as [33]

$$\beta(E) = \frac{2\pi n(E)}{\lambda_0} = \beta_0 - \frac{2\pi}{\lambda_0} \cdot \frac{1}{2}\mathcal{P}n_0^3 E \tag{4.3}$$

Such that the phase $\varphi$ is represented by

$$\varphi(V) = \varphi_0 - \frac{\pi}{\lambda_0}\mathcal{P}n_0^3\frac{L}{d}V = \varphi_0 - \pi\frac{V}{V_\pi} = \varphi_0 + \Delta\varphi(V) \tag{4.4}$$

Where $L$ is the length of the modulator (see figure 4.3) and $d$ is the distance between the electrodes used to apply the bias.

The Pockels effect, however, only arises in crystalline solids lacking inversion symmetry, which unfortunately is not the case of silicon. As a consequence, other materials have been studied and in particular the most popular electro-refraction modulator is made of Lithium Niobate ($LiNbO_3$), which shows an extremely high Pockels coefficient (such that $\chi^{(2)} \simeq 360$ $^{\text{pm}}/_{\text{V}}$ [67]). Furthermore, the ER is as high as 25 dB and bit rates of more than 10 Gbps are achievable [33]. On the other hand, these devices entail many drawbacks. For instance, they cannot be directly integrated into an electronic circuit nor built out of the well-known Complementary Metal-Oxide-Semiconductor (CMOS) which ensures quality, low cost and efficiency. Moreover, they are bulky and their massive footprint is usually detrimental in small devices. Furthermore, they require a large driving voltage leading to a higher power consumption [65], [67], [68].

As a result, studies have been carried out on how to obtain a second-order susceptibility in centro-symmetric materials. In particular, it has been proven that it is possible to break the crystal symmetry by applying a mechanical stress due to the deposition of a straining layer (usually $SiN$ or $Si_3N_4$) on top of the silicon waveguide so that a finite Pockels coefficient is generated [65]. By engineering the cross section of the waveguide and the deposition process it is possible to achieve results close to that of Lithium Niobate, corresponding to $\Delta n \simeq 3.5 \times 10^{-5}$ for an applied voltage of 30 V [1].

### 4.3.3 Plasma dispersion effect

A third phenomenon that can be employed to modulate light signals is the variation of the refractive index due to the presence of carriers in the optical path, also called free carrier concentration variation. In [69] the authors extensively studied the relation between the behavior of the light and the concentration of carriers, resulting in the well-know Soref-Bennett relations for the refractive index ($n$) and loss ($\alpha$), which are

$$\Delta n = -\frac{e^2\lambda_0^2}{8\pi^2 c^2 \varepsilon_0 n} \cdot \left(\frac{\Delta N_e}{m^*_{ce}} + \frac{\Delta N_h}{m^*_{ch}}\right) \tag{4.5}$$

$$\Delta \alpha = -\frac{e^3\lambda_0^2}{4\pi^2 c^3 \varepsilon_0 n} \cdot \left(\frac{\Delta N_e}{m^*_{ce}\mu_e} + \frac{\Delta N_h}{m^*_{ch}\mu_h}\right) \tag{4.6}$$

Where $e = 1.602 \times 10^{-19}$ C is the electron elementary charge, $m^*_{ce}$ and $m^*_{ch}$ are the conductivity effective mass of electrons and holes respectively, $\mu_e$ and $\mu_h$ are the electron and hole mobilities respectively. $\Delta N_e$ and $\Delta N_h$ are the variation in the electron and hole concentrations in the channel respectively.

The two parameters are related by the so-called Kramers-Kronig relation [70]

$$\Delta n(\omega) = \frac{c}{\pi} \mathrm{P} \int \frac{\Delta\alpha(\omega')\partial\omega'}{\omega'^2 - \omega} \tag{4.7}$$

Where P is the Cauchy principal value.

In the case of silicon and around the reference wavelength $\lambda_0$=1550 nm, they become [71]

$$\Delta n = -8.8 \times 10^{-22} \Delta N_e - 8.5 \times 10^{-18} \Delta N_h^{0.8} \tag{4.8}$$

$$\Delta \alpha = 8.5 \times 10^{-18} \Delta N_e + 6 \times 10^{-18} \Delta N_h \tag{4.9}$$

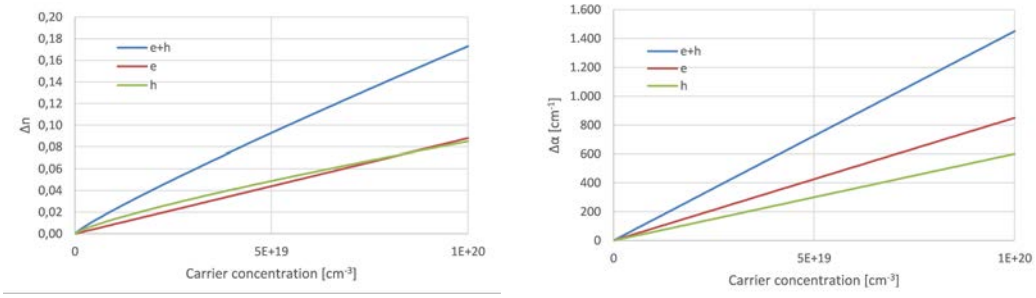


(a) $\Delta n$ (b) $\Delta\alpha$

Figure 4.5: *Soref-Bennett parameters versus carrier concentration*

In figure 4.5 the parameters have been calculated using MATLAB. In particular, a distinction is made between the contribution of the electrons ($e$ in the plot) and holes ($h$ in the plot). It is possible to recognize that the hole contribution is preferable since it allows a more efficient modulation of the refractive index (up to carrier concentrations close to $10^{20}$ which are never achieved anyway) coupled with a less detrimental loss increase.

As a consequence, in the presence of a carrier concentration of $\Delta N_e = \Delta N_h = 10^{18}$ cm$^{-3}$, which is easily feasible (see for instance figure 6.23), the refractive index change would be around $3 \times 10^{-3}$ and as such considerably larger compared to that achieved by means of the Pockels effect.

### 4.3.4 Thermo-optic effect

The refractive index of the optical material is not constant with respect to temperature oscillations. For instance, in [72] the authors have determined the dependence of the refractive index on the temperature for silicon at a wavelength of 1523 nm in a temperature range spanning from 300 to 550 °K, which is

$$\frac{\partial n}{\partial T} = 9.48 \times 10^{-5} + 3.47 \times 10^{-7}\, T - 1.49 \times 10^{-10}\, T^2 \ [\mathrm{K}^{-1}] \qquad (4.10)$$

In particular, at 300 °K the thermo-optic coefficient is foud to be around $2 \times 10^{-4}$ [K$^{-1}$] and therefore not negligible. Due to the fact that thermo-optic effects are extremely slow (of the order of ms [73]), however, they are not useful for modulation purposes. On the contrary, they can be detrimental since a device might spontaneously heat up during operation, leading to oscillations of its optical properties. Moreover, there is a direct correlation

between temperature and energy gap, which can be a serious issue in certain devices. The correlation can be expressed with Varshni formula as [74]

$$E_G = E_0 - \alpha \frac{T^2}{T + \beta} \tag{4.11}$$

Where $E_0$ is the value of the bandgap at 0 °K while $\alpha$ and $\beta$ are fitting parameters that depend on the specific material.

## 4.4 Parameters

The most important FOMs in the case of modulators are listed and explained below.

### 4.4.1 Insertion Loss

The Insertion Loss (IL) accounts for the total amount of power which is lost when coupling the device to a waveguide or optical fiber. It can be expressed as

$$IL = 10 \log_{10}(\frac{P_{in}}{max\{P_0\}}) \text{ [dB]} \tag{4.12}$$

Where $P_{in}$ is the optical input power and $P_0$ is the optical output power.

### 4.4.2 Extinction Ratio

The Extinction Ratio (ER) is defined as the ratio between the maximum and minimum optical output power. It can be written as

$$ER = 10 \log_{10}(\frac{P_{max}}{P_{min}}) \text{ [dB]} \tag{4.13}$$

### 4.4.3 Optical Modulation Amplitude

The Optical Modulation Amplitude (OMA) expresses the difference between the maximum and the minimum optical power levels, and reads

$$OMA = P_{max} - P_{min} \text{ [W]} \tag{4.14}$$

It can also be expressed as a function of the ER as

$$OMA = 2P_{avg} \frac{ER - 1}{ER + 1} \text{ [W]} \tag{4.15}$$

Where $P_{avg} = {}^{(P_{max}+P_{min})}/_{2}$ is the average optical power considering a perfectly balanced flow of bits (50% "0", 50% "1").

### 4.4.4 Half-wave voltage

The half wave voltage $V_\pi$ is the voltage necessary to achieve a complete modulation of the signal, meaning switching from "0" to "1" (see section 4.2).

### 4.4.5 Modulation Efficiency

Given a modulator of length $L$, meaning that the active region subjected to the applied voltage has size $L$, it is possible to define the modulation efficiency $V_\pi L$ [V $\cdot$ cm] which is one of the most useful FOMs when it comes to modulators comparison, since the efficacy of the device does not depend only on the voltage applied but also on the physical length of the active area.

# Chapter 5

# Ring Resonators

The main topic of this chapter is ring resonators. They are among the most promising optical network devices in silicon photonics. They serve a large variety of purposes and combine direct integration in the well-known CMOS technology with optical capabilities and advantages (such as speed and bandwidth). Furthermore, their footprint is extremely low and they are highly tunable.

First, ring resonators are described and their main properties and parameters discussed. Afterwards, the main fabrication methods are introduced and finally their most important application presented.

## 5.1 Introduction and parameters

A ring resonator (or racetrack when not perfectly round) comprises an optical waveguide which is looped back on itself, as shown in figure 5.1 where a 5 $\mu$m radius ring coupled to two waveguides has been imaged with a Scanning Electron Microscope (SEM).

As a result, the light travelling inside the waveguide undergoes interference since it interacts with itself after a full loop. The interference can be both destructive or constructive according to the wavelength and the particular structure of the ring. In the case of destructive interference the propagation for that specific wavelength is denied, while in the other case it can travel inside the ring until it becomes negligible due to attenuation. Apart from the ring, one or more waveguides are coupled to the device so that light can be injected in the circular channel.

In figure 5.2 a generic ring resonator is shown. In A (left) the ring resonator is coupled only to one waveguide and the configuration is called all-pass. In B (right) there are two waveguides attached to the opposite sides

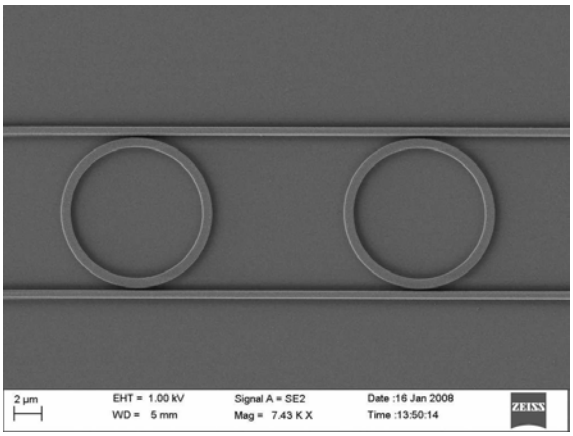


Figure 5.1: *SEM image of two ring resonators* [75]

of the ring, assembling an add-drop ring resonator. In chapter 6 only the former configuration is studied.

The parameters presented in figure 5.2 refer to the physical properties of the device. For instance, $a$ is the single-pass amplitude transmission, containing both propagation (linear) and coupling losses, the latter pertaining the coupling region between waveguide and ring (its values are calculated in 6.2). In particular, it can be written as

$$a = e^{-\frac{\alpha_{tot} L}{2}} \tag{5.1}$$

With $\alpha_{tot}$ [$^1/_{\text{cm}}$] the total power attenuation coefficient of the ring and $L$ [cm] the round trip length of the ring. $r$ is the self coupling coefficient, that is, the amount of light flowing in the waveguide which is not coupled to the ring while $k$, the cross coupling coefficient, represents the amount of light which is not transmitted to the other side of the waveguide (their calculations are made in section 6.2) [12]. In the case of ideal coupling regions (no loss), it has to be that $r^2 + k^2 = 1$ since they must sum to unity, representing a percentage [7].

The condition to be fulfilled in order to obtain constructive interference in the ring is

$$\lambda_{res} = \frac{n_{eff} L}{m},\ m \in \mathcal{N} - \{0\} \tag{5.2}$$

Only the resonant frequencies $\lambda_{res}$ (plus a certain offset given that the spectrum is never a delta function) are found in the ring.

By assuming Continuous Wave (CW) operation and neglecting backreflections in the bus waveguide (which are found to be really low, see the loss

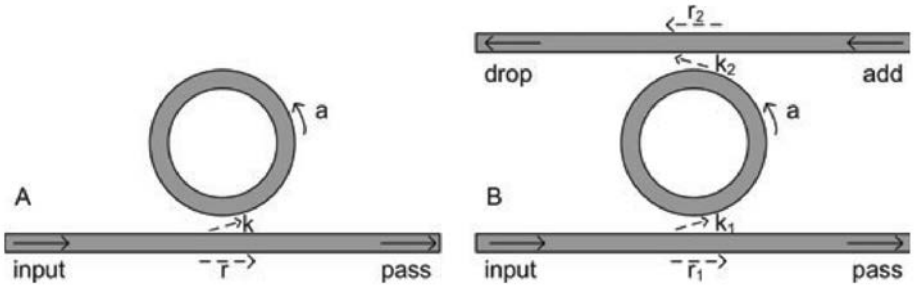


Figure 5.2: *Ring resonator and parameters* [7]

in section 6.2), the ratio between transmitted and input field in the case of all-pass rings can be written as [7]:

$$\frac{E_{pass}}{E_{input}} = e^{i(\pi+\phi)}\frac{a - re^{-i\phi}}{1 - rae^{i\phi}} \tag{5.3}$$

Where $\phi = \beta L$ is the single-pass phase shift. To obtain the intensity transmission, equation (5.3) has to be squared, obtaining

$$T = \frac{I_{pass}}{I_{input}} = \frac{a^2 - 2ra\cos(\phi) + r^2}{1 - 2ar\cos(\phi) + (ra)^2} \tag{5.4}$$

A peculiar phenomenon appears with reference to critical coupling, in which the transmission at resonance drops to 0. Critical coupling is the condition for which the coupled power is equal to the power loss in the ring, and therefore $(1 - a^2) = k^2$ leading in the case of ideal couplers to $r = a$ [76]. The other conditions are called undercoupling, when the injected power is less than the loss in the ring ($r > a$), and overcoupling, when the injected power overcomes the total amount of loss ($r < a$).

In figure 5.3 some of the most important spectral parameters for ring resonators are presented.

The Full Width at Half Maximum (FWHM) is a common parameter used to describe the spectral broadening of the resonance. The lower the FWHM the more selective and "notch-like" is the filter, being it able to react to a small amount of frequencies only. In the case of all-pass ring resonators it can be expressed by [7]

$$\text{FWHM} = \frac{(1 - ra)\lambda_{res}^2}{\pi n_g L\sqrt{ra}} \text{ [m]} = \frac{(1 - ra)c}{\pi n_g L\sqrt{ra}} \text{ [Hz]} \tag{5.5}$$

From the equation above it is possible to notice that the parameter increases with increasing linear loss and decreases when the ring has a large radius.

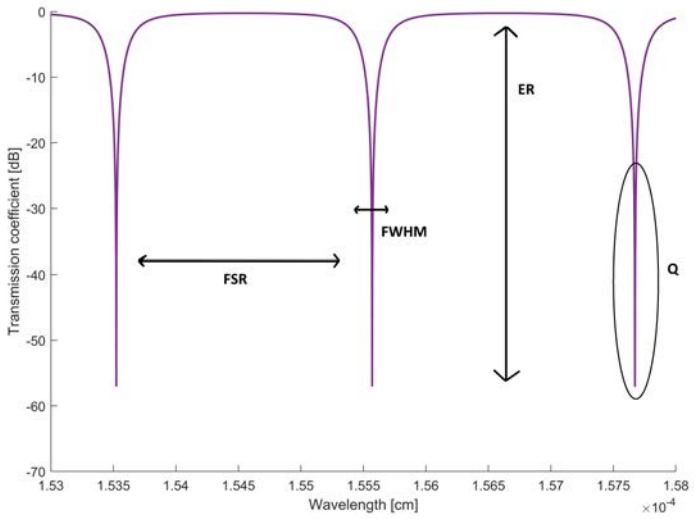


Figure 5.3: *Output spectrum of an arbitrary ring resonator*

Another important indicator of the quality of the ring resonator is the Free Spectral Range (FSR), which is used to express the distance between two consecutive resonant dips. It can be written as [7]

$$\text{FSR} = \frac{\lambda_{res}^2}{n_g L} \text{ [m]} = \frac{c}{n_g L} \text{ [Hz]} \tag{5.6}$$

The FSR depends heavily on the length of the ring, with large ones displaying closer resonances. In most applications the FSR is required to be large and therefore small rings are preferable. Small rings are particularly easy to fabricate out of silicon because of the high refractive index difference leading to a tight confinement of the mode inside the waveguide (see section 3.2).

Furthermore, the finesse is defined as the ratio of FSR and resonance width as

$$\text{Finesse} = \frac{\text{FSR}}{\text{FWHM}} = \frac{\pi\sqrt{ra}}{1-ra} \tag{5.7}$$

The finesse represents the number of round trips that a light signal is able to complete inside the ring before its initial energy is reduced by $1/e$ . As a consequence, it is directly dependent on the linear loss and thus on the length of the silicon loop.

Similar to the finesse is the quality factor ($Q$). It is defined as

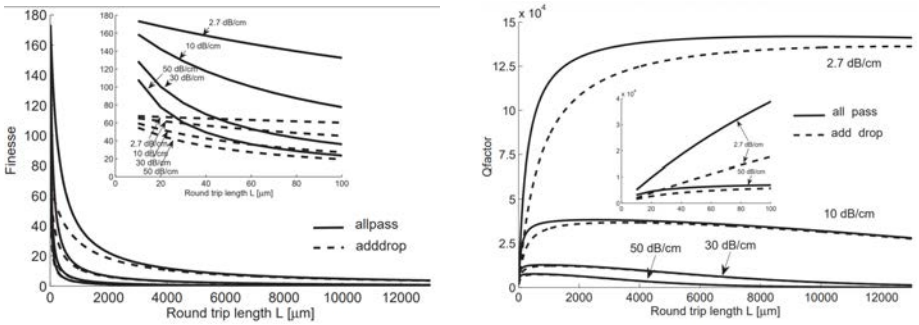


(a) Finesse (b) Quality factor

Figure 5.4: *Finesse and quality factor versus ring length for different linear loss parameters* [78]

$$Q = \frac{\lambda_{res}}{\text{FWHM}} = \frac{\pi n_g L \sqrt{ra}}{\lambda_{res}(1-ra)} \tag{5.8}$$

It represents the number of amplitude oscillations that the light signal performs inside the ring before its initial energy is reduced by $1/e$. It is also proportional to the ratio of the stored optical energy inside the ring and the energy loss rate [77]. In this case there is no direct dependence on the length of the ring (covered by $L$ at the numerator) while the reliance on the linear loss remains.

In figure 5.4 finesse and quality factor are plotted against the round trip length of the ring and their response to ring radius and loss is clearly noticeable.

The last parameter is the ER (see section 4.4.2) which relates to the difference in dB between the maximum and the minimum transmission (at resonance), that is

$$\text{ER} = 10\log_{10}(\frac{T_{max}}{T_{min}}) \tag{5.9}$$

## 5.2 Physical properties and fabrication process

### 5.2.1 Fabrication

One of SOI ring resonators main advantage is the ease of fabrication. Since they are built out of silicon, the well-known and efficient technologies used in integrated electrical circuits can be employed [79]. The devices are usually carved on a silicon wafer on which lithographic techniques are applied in

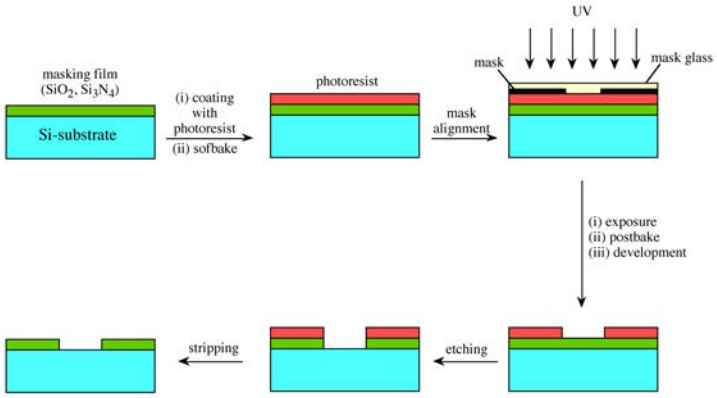


Figure 5.5: *Lithographic process* [80]

order to shape the bulk silicon into a specific pattern depending on the device that is being built. The production process can be subdivided in four main categories: film deposition, patterning, etching and, if need be, doping. The schematic of a common lithographic process can be seen in figure 5.5.

Among the different methods for growing layers of a certain material, Plasma Enhanced Chemical Vapor Deposition (PECVD) is mainly used to deposit a thin film of a given substance by virtue of chemical reactions caused by plasma reacting gases [81]. While PECVD is commonly utilized in the industry because of its speed, it does not provide a high degree of accuracy, which is the reason why another technique called Molecular-Beam Epitaxy (MBE) is preferable when high precision is required. MBE takes place in a high vacuum environment in which single molecules of a specific material are shot one after the other into a target position in the substrate, obtaining an exceedingly high accuracy, while the downside is the low deposition rate [82]. Silica layers can also be obtained by direct oxidation of the silicon after air exposure (passivation) [83].

To model the target layer accordingly to the specific outline of the device a chemical photoresist layer is applied on the wafer by means of spin coating. On top of the resist a photomask of a given shape is then deposited [84]. The sample is subsequently shined with Ultraviolet (UV) light (UV lithography) in the case of low-accuracy mass-producted devices or exposed to excited electrons (electron beam lithography) to obtain sub-10 nm resolutions [85]. The photoresist layer not protected by the photomask changes its chemical composition so that it can be developed, meaning that it reacts with a suitable chemical (called developer), and it is subsequently easily removed (positive resist), while when the resist is negative the removed part is the

one which was not exposed to the high energy radiation.

Etching is the supervised ablation of certain areas of the wafer in order to dispose of unwanted lumps of material, to free space for a subsequent deposition or simply to polish a surface so to obtain a pure boundary and consequently limiting scattering, loss and recombination [85]. The two main etching techniques are called dry etching (employing plasma) and wet etching (utilizing a liquid chemical reactant). The ablating agent only reacts with areas of the device not covered by the photoresist which therefore allows the fabrication of customly designed devices. Afterwards, the remaining photoresist is removed, usually with a liquid solution called "resist stripper" that causes the resist to detach from the substrate.

Finally, a paramount step in nanofabrication is doping, that can be carried out before the photoresist removal or afterwards if no specific doping profile is needed. To dope silicon, foreign ions (Group III elements -primarily Boron- in the case of p-doping or Group V elements -primarily Phosphorus- in the case of n-doping) are utilized. First, the wafer is annealed (exposed to high temperatures for a suitable amount of time and subsequently cooled down) to allow dopant atoms to attach and penetrate into the bulk. Ion implantation and diffusion doping are the most common doping methods. In the case of diffusion, dopant atoms are introduced at the wafer surface and from there they diffuse in the silicon by sheer concentration imbalance creating a doping gradient rapidly decreasing while moving away from the surface [86]. When it comes to ion implantation, the dopant ions are accelerated and made to impinge on the wafer surface. The penetration depth depends on the energy of the single ion and since it is a statistical process a certain doping gradient is still recovered, even though it is concentrated in the bulk and not on the surface [87]. However, particular care must be taken since high energy ions can deal damage to the device.

### 5.2.2 Physical properties

SOI ring resonators entail high contrast waveguides, since at the usual communication wavelengths (around 1550 nm) $n_{Si} \simeq 3.477$ while $n_{SiO_2} \simeq 1.444$ [88]. The high contrast results in tight confinement of the optical mode and as a consequence allows compact bends without overly compromising the loss. As already pointed out in figure 3.8, TE modes are mainly overlapping with the cladding via the lateral sidewalls of the waveguide. These vertical sidewalls are rough surfaces because usual polishing methods (such as etching, see section 5.2.1) are not effective when the surface is not horizontal with respect to the plane of the wafer. As a consequence, it is paramount to lessen their interaction with the optical mode, for instance by reducing the

height of the waveguide, which in turns means having to increase the width to allow the first mode to propagate (see section 3.3). Another possibility is to use TM polarized light that extends mostly over the smooth horizontal surfaces of the waveguide (see figure 3.8). However, TM modes are loosely bound to the waveguide and since they interplay more extensively with the cladding they cannot be used in the case of tight bends due to the fact that the radiation loss would be detrimental [7].

Another consequence of the high contrast is a massive dispersion, such that the group index is almost twice as large as the effective index (for comparison, see figure 6.44 (b) and figure 6.45 (a)) [7]. Furthermore, they are also extremely sensitive to dimensional variations.

For all these reasons, common waveguide cross sections for ring resonators span from 400 to 500 nm in width and between 200 and 250 nm in height [8], [13], [89], [90]. This particular size allows monomodal propagation, limiting the detrimental effects caused by a multimode configuration (see sections 3.3 and 3.4).

The calculation of the linear loss is somewhat arduous since it depends heavily on wavelength, waveguide structure and fabrication process, such that values ranging from 2 to 20 $^{\mathrm{dB}}/_{\mathrm{cm}}$ have been recovered [13], [51], [91], [92].

## 5.3 Applications

Ring resonators can be used in a large variety of different applications and have therefore been extensively studied in academic and scientific enviroments because of their versatility. Follows a list of the main fields in which ring resonators have proven to be extremely important.

### 5.3.1 Sensing

For starting, due to their high sensitivity to the variation of the physical parameters, they are successfully employed for sensing purposes. In particular, the resonance peak shifts abruptly with the coupling, the loss and the effective refractive index of the resonant structure. By changing any of those properties the frequency spectrum of the ring is greatly affected and the resulting variation can be studied to understand its cause. For instance, they can be used as a strain sensor in order to directly relate to physical deformations. In [93] the authors claimed a sensitivity of $\simeq 0.6$ $^{\mathrm{pm}}/_{\mu\epsilon}$ meaning that a shift of the resonant wavelength of 0.6 pm can be achieved by applying 1 $\mu\epsilon$. Moreover, rings are also influenced by thermal oscillations so that it is

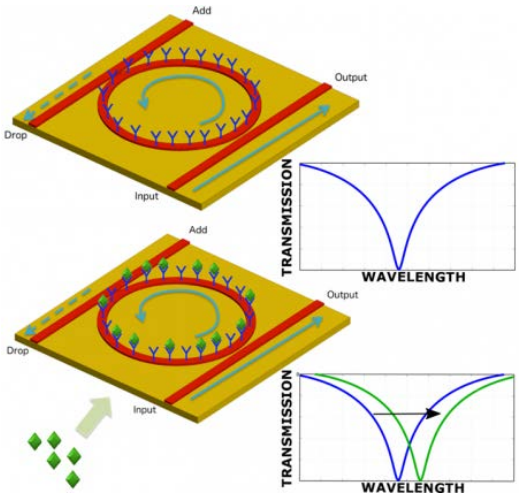


Figure 5.6: *Biosensing* [96]

possible to achieve sensitivities up to 230 $^{\mathrm{pm}}/_{^{\circ}\mathrm{C}}$, which means that a shift of 230 pm in the resonant wavelength is achievable with just 1 °C variation [94]. Important applications are also found in biology when it comes to label-free biosensors set up to detect the presence of a specific analyte. They consist of a ring resonator with a surface which is chemically modified by adding receptor molecules that are selective to the analyte to be detected. The ring is later flooded with a liquid solution and the spectral response retrieved. The spectrum of the ring is different whether in the solution the analyte is present or not (figure 5.6) and its impact on the resonance peaks depends on its concentration, allowing more accurate and less expensive measurements compared to other techniques that need labeling of the analyte [95]. The sensitivity of the device can be measured by considering how much the adhering analyte increases the thickness of the waveguide. For instance, in [78] a waveguide of size 480×220 nm is considered and the authors claim that for practical values of the thickness the response is linear. In particular, it is found as 0.158 $^{\mathrm{nm}}/_{\mathrm{nm}}$ in the case of TE mode and 0.290 $^{\mathrm{nm}}/_{\mathrm{nm}}$ in the case of TM mode, which can be explained with the reduced waveguide confinement of the latter.

### 5.3.2 Optical buffer

Additionally, ring resonators are traditionally utilized as optical buffers. CROW systems of different rings coupled together (high order ring resonators) are effective to obtain optical delay lines in photonic integrated circuits, since near resonance the optical intensity inside the ring is extremely

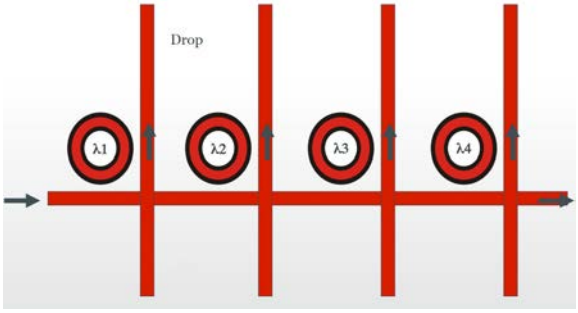


Figure 5.7: *Ring resonator DEMUX* [77]

high. The time delay-bandwidth product is given by [7]

$$T_{CROW} = \frac{N}{2\pi} \tag{5.10}$$

Where $N$ is the order of the filter (that is, the number of cascaded rings). The delay thus obtained can be as large as 200 ps for filters of order 40, as claimed in [97].

### 5.3.3 MUX/DEMUX

Another important application of ring resonators is the multiplexing/demultiplexing of the signal in the case of WDM or DWDM coding. These modulation techniques consist on strikingly enhancing the data rate of an optical channel by sending simultaneously light at different frequencies provided that the spectrum of the signal is clearly resolvable. In particular, when it comes to WDM the light pulses (called channels) are separated by 100 GHz (namely, $\simeq 0.4$ nm at $\lambda = 1550$ nm) while for DWDM it is 50 GHz (that is, $\simeq 0.8$ nm at $\lambda = 1550$ nm) [33]. As can be seen in figure 5.7, by employing rings with different resonant peaks as a DEMUX system it is possible to redirect a particular channel to its specific detector and, as a consequence, successfully demodulate the input signal [98]. However, the rings are exceedingly prone to fabrication defects and as a result they have to be thoroughly tested before being used for such purpose. Moreover, high order filters provide an improved spectral behavior since they display a more uniform pass band over a wider wavelength range, besides the improved ER outside the desired bandwidth [7].

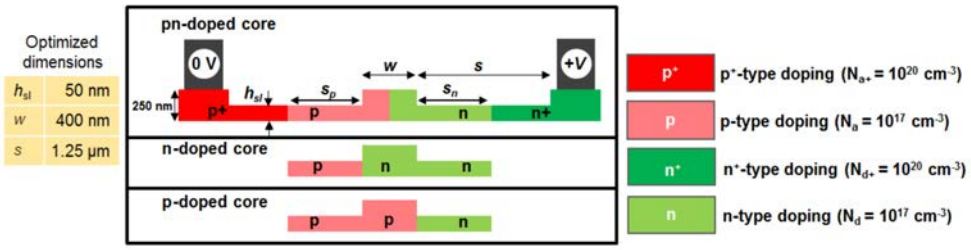


Figure 5.8: *Carrier depletion modulator* [99]

### 5.3.4 Ring modulator

The last application of ring resonators presented is the modulation, which is the topic of the thesis and will be further discussed in chapter 6. A silicon ring modulator is used as an OOK modulated device in which the operating wavelength is close to the resonance peak such that high ERs can be obtained with just a relatively small shift of the dip due to a variation in the optical properties of the waveguide. To do so, high slopes (low FWHM) rings are needed, resulting in high $Q$ and finesse. On the other hand, if this parameter is too large, the overall switching time of the device will be negatively affected being it dependent on how fast the optical power inside the ring is dissipated [7]. In particular, the 3 dB cut-off frequency can be written as [11]

$$f_{3dB} = \frac{f_{OPT} \cdot f_{EL}}{\sqrt{f_{OPT}^2 + f_{EL}^2}} \tag{5.11}$$

Where

$$f_{OPT} = \frac{c}{Q(0\,V) \cdot \lambda_{res}(0\,V)} \tag{5.12}$$

Is the optical component stemming from the lifetime of the photons in the waveguide ($Q$ and $\lambda_{res}$ are considered at zero bias applied) while

$$f_{EL} = \frac{1}{2\pi RC} \tag{5.13}$$

Is the standard bandwidth of the electric circuit due to the RC constant of the device and as such it strongly depends on the physical size of the device.

Among the FOMs in the case of ring modulators, $V_\pi L$ is widely considered as one of the most important parameters to be taken into considereation (see section 4.4.5) and can be expressed as [99]

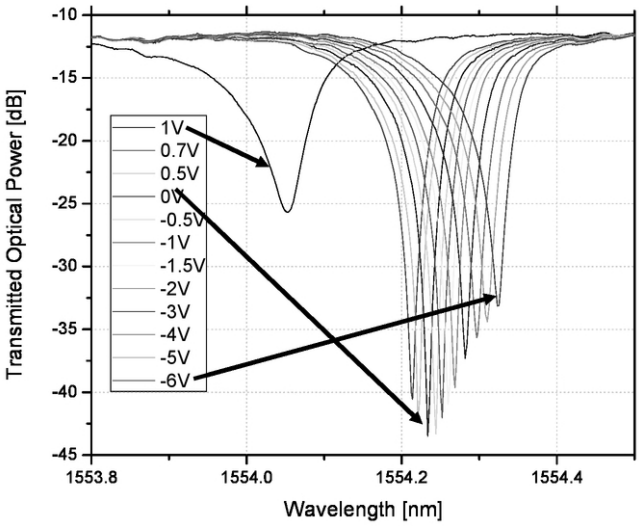


Figure 5.9: *Output spectrum of a depletion mode ring modulator versus bias* [101]

$$V_\pi L = \frac{\lambda \cdot V}{2 \cdot \Delta n_{eff}} \tag{5.14}$$

The modulation occurs by virtue of the refractive index variation (plasma dispersion effect), which is caused by the oscillation of the carriers in the waveguide due to the swing of the applied voltage (see section 4.3.3). Two are the main techniques employed: carrier injection and carrier depletion.

In the case of carrier depletion the ring cross section of the horizontal junction version can be seen in figure 5.8. The main structure is a PN diode whose doping concentration extends over the waveguide core, which can be mixed (top), n-only (middle) or p-only (bottom). Better performing modulators utilize the so-called vertical junction, in which the p and n areas are put one on top of each other [100].

The device operates in depletion mode, meaning that, when a reverse voltage is applied, the space charge region becomes larger and therefore less carriers are found in the waveguide, causing a variation in the refractive index. The spectrum thus obtained can be seen in figure 5.9. When the voltage is negative, the modulation results in a slight red-shift of the resonant frequency followed by a mild ER decrease.

Positive voltages are usually the case for injection mode modulators, based on PIN diodes in which the intrinsic layer (which is actually slightly doped) extends over the waveguide. As can be seen in figure 5.9, positive voltages lead to a blue-shift of the resonant wavelength and a steep decrease

of the ER. The modulation is much more effective since the intrinsic region is flooded with carriers (the diode is turned on, in particular when $V$ is larger than 0.7 V in figure). The downside is that a current is flowing in the device and the bandwidth is much smaller since it depends on the minority carriers lifetime (resulting in bandwidth of around 1 GHz [71]), while in the former case it depends on the junction capacitance discharge which is much faster (with modulation speed up to 20 GHz [71]) [7]. Consequently, if the goal is to obtain an effective modulation with a small $V_\pi L$ it is better to resort to carrier injection. On the other hand, if the focus is on the speed of the device, one better resort to carrier depletion.

A possible improvement of the pin modulator is by means of pre-emphasis, which consists on using two different bias levels to speed up the modulation frequency. Results of the order of tens of GHz are retrieved in [102].

# Chapter 6

# Simulation Results and Discussions

This chapter presents the main results obtained in this thesis work. The programs used are primarily MATLAB and Lumerical. In particular, Lumerical provided the simulation for what regards the physical parameters of the ring modulator, such as coupling coefficient, flowing current and effective refractive index, while MATLAB made the analysis of the data possible in order to retrieve the output spectrum of the device and the calculation of the most important parameters, such as FSR, finesse and$V_\pi L$. MATLAB was also employed to code and implement the effective refractive index method. As regards the data, it was collected for different configurations of the device. Among the different parameters considered, the lateral slab height, the intrinsic region width, the lateral slab width, the doping concentration and the ring bend.

## 6.1 Effective index method

The effective index method, as presented in [103] and [104], is a numerical process useful to calculate the effective refractive index of a given waveguide. It is based on the subsequent approximations of different areas of the waveguide by calculating their partial refractive indices and consequently merging the sub-waveguides thus obtained in order to retrieve the final refractive index. First, the columns ($n_1 - n_4 - n_7 \rightarrow n_{eff,1}$, $n_2 - n_5 - n_8 \rightarrow n_{eff,2}$ and $n_3 - n_6 - n_9 \rightarrow n_{eff,3}$) are considered and afterwards the remaining rows ($n_{eff,1} - n_{eff,2} - n_{eff,3} \rightarrow n_{eff}$) are elaborated (consider a subdivision of the waveguide as in figure 6.1, where the optical waveguide of size $w \times t$ is in the central area $n_5$) .

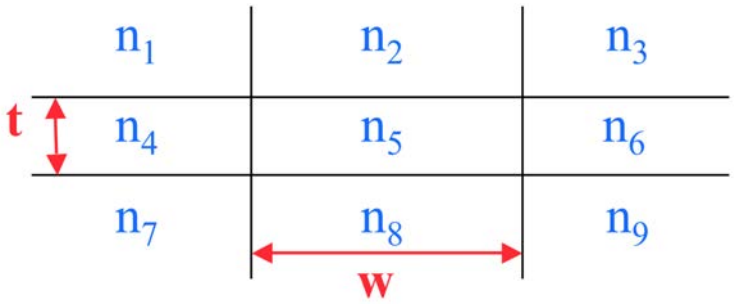


Figure 6.1: *Waveguide subdivided in small regions* [103]

This method has been implemented in MATLAB in the case of a rib waveguide whose cladding is made of air ($n = 1$) or $SiO_2$ ($n = 1.44$) at 1550 nm wavelength. The waveguide is made of silicon with $n = 3.45$. The refractive index is extracted sweeping over different lateral heights, ranging from 50 to 110 nm while the waveguide itself is 220 nm high and 460 nm wide. In figure 6.2 the transcendental equation to be solved is shown with reference to an air cladding for the central column (made up of $SiO_2$, $Si$ and air).

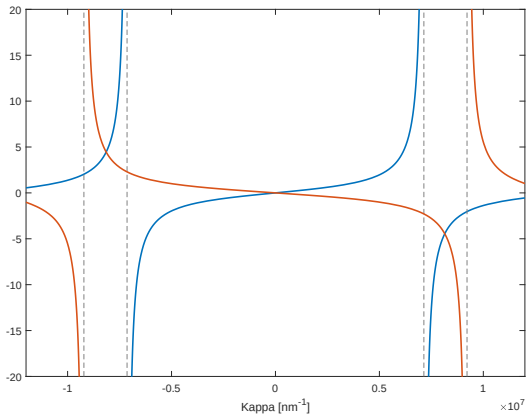


Figure 6.2: *Transcendental equation solved in the case of air as cladding*

As can be seen in figure 6.3, with increasing slab height the effective refractive index grows as well, being the refractive index of the waveguide larger than the one in the surroundings. At the same time, it is clearly noticeable that, having an air cladding (whose refractive index is the lowest), the overall refractive index of the waveguide is significantly lower for all the configuration tested, with values spanning from $-1.7\%$ for the lowest slab height considered to $-1.05\%$ in the case of the 110 nm slab height.

The results are realistic and can be compared, for instance, with those retrieved in Lumerical and shown in figure 6.40. Another comparison can be drawn with [105], where, however, the authors considered a strip waveguide and therefore the values are lower, namely spanning from 2.36 at $\lambda = 1550$ nm.

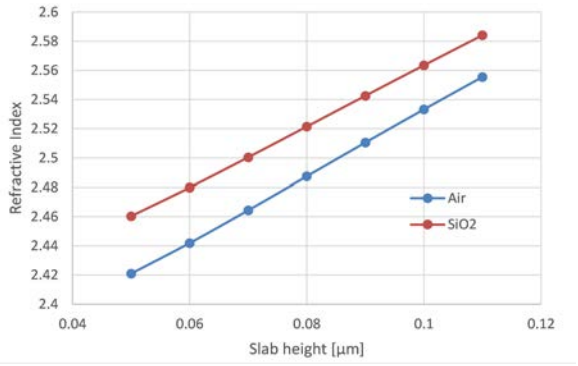


Figure 6.3: *Results plotted as a function of the slab height in the case of air and silicon dioxide cladding*

## 6.2 Coupling coefficient

To calculate the coupling coefficient between the straight waveguide acting as the input/output channel for the system and the ring, the Lumerical FDTD simulator has been used. The model employed is shown in figure 6.4 in relation to strip waveguides. In particular, the waveguides considered are both $460 \times 220$ nm. In the case of the rib configuration, the lateral slab has a height of 70 nm.

As regards the mode solver, a fine mesh has been set up in the area between the two waveguides in order to achieve a greater accuracy in the calculation, and the signal launched in the input waveguide has a bandwidth ranging from 1500 to 1600 nm, as can be seen in figure 6.5, consequently covering the main transmission window (C-band). The actual simulation area does not entail the entire ring/waveguide structure but only a section, so that the calculation proceeds faster without affecting the final results.

In figure 6.6 the behavior of the rib waveguide is analyzed taking into consideration a certain wavelength only, namely 1556 nm. It can be seen that the self-coupling coefficient $R = |r|^2$ decreases both with the reduction of the coupling distance (as explained theoretically in section 3.5 due to a stronger overlap between the evanescent fields) and with more sizeable rings,

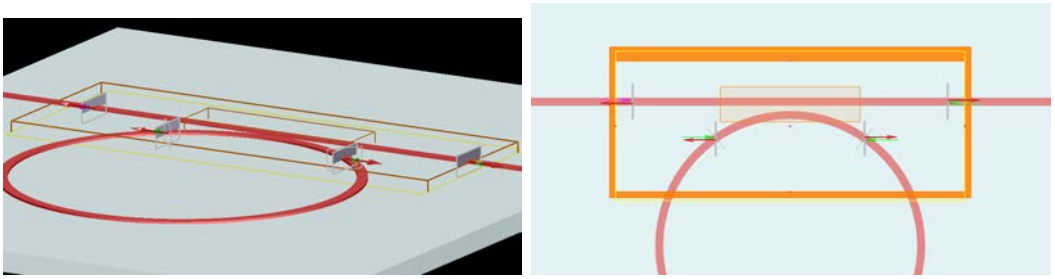

(a) Side view of the model (b) Top view of the model

Figure 6.4: *Model built with Lumerical. The oxide cladding has been disabled for examination purposes*

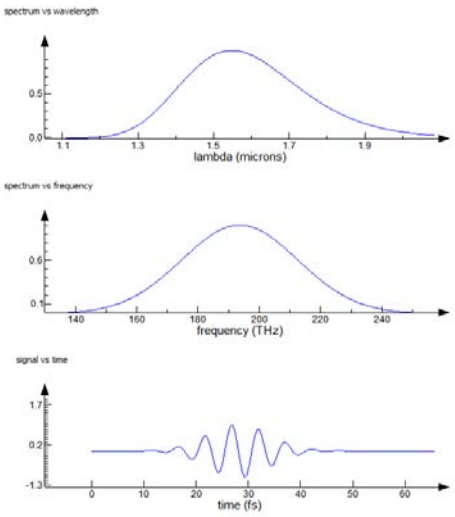


Figure 6.5: *Signal launched, details*

because the effective coupling length is larger when the ring waveguide takes longer to bend away. On the other hand, as expected, the cross-coupling coefficient $K = |k|^2$ behaves in the opposite way.

In figure 6.7 the light intensity is plotted along the structure. The top branch is the straight waveguide while the bent bottom one is the input channel of the ring resonator. It is clearly noticeable that when it comes to long radii and small gaps the amount of light coupled is remarkably larger (namely, around 50%) than in the other case, that is, with a small ring and large gap between the waveguides (namely, around 1%).

When a comparison with the wavelength is made, it is found that shorter wavelengths result in a lesser coupling, as expected from the theory (section 3.4.2). The result of such a comparison can be found in figure 6.8.

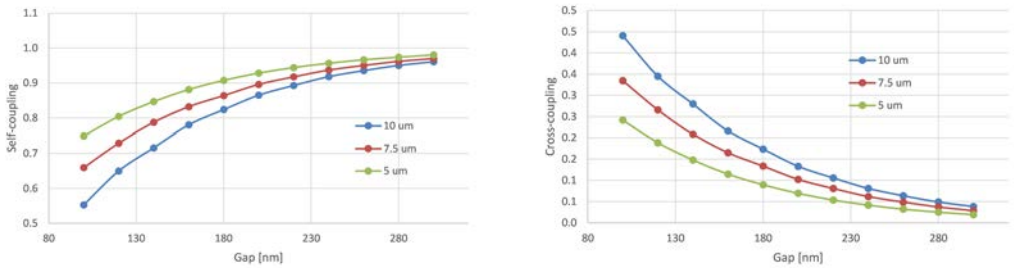


(a) Self-coupling coefficient (b) Cross-coupling coefficient

Figure 6.6: *Coupling coefficients in the case of a rib waveguide versus the gap distance between the two waveguides for different bend*s

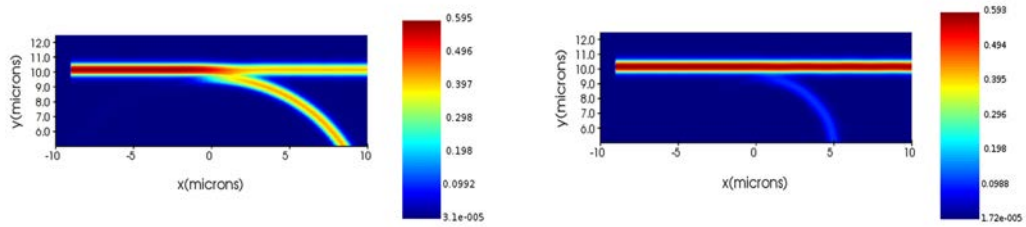


(a) 10 $\mu$m radius ring and 100 nm gap (b) 5 $\mu$m radius ring and 300 nm gap

Figure 6.7: *Light propagation in the structure for different configurations*

It is interesting to find the amount of loss in the coupling region. In a lossless coupler we would have $R + K = 1$, but in this case the result is quite different and can be seen in figure 6.9. The loss is found to increase when the cross-coupling coefficient is larger, meaning in the case of small gaps and long wavelengths. Overall though, it is really low, spanning from 0.9% for small gaps and radii to less than 0.1% when the coupling distance is large.

Afterwards, the analysis of the difference between rib and strip waveguides is carried out. As depicted in figure 6.10, the rib waveguide is significantly more efficient at coupling compared to the other one, the reason being the direct dielectric connection between the two waveguides and the consequent spread of the light towards the adjacent channel. The behavior is enhanced especially when the gap gets smaller.

Finally, with reference to strip waveguides, a comparison between the coupling coefficient and the wavelength is charted in figure 6.11. The improvement in coupling capability is strongly determined by the gap width, as for the rib waveguide; however, it is much more wavelength dependent than

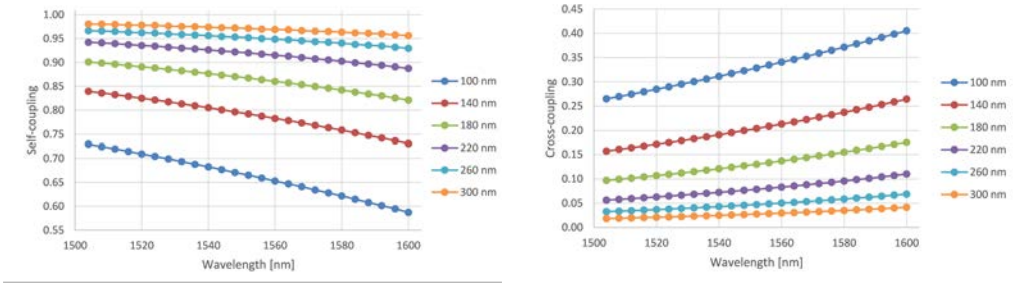


(a) Self-coupling (b) Cross-coupling

Figure 6.8: *Coupling coefficients in the case of a rib waveguide versus the wavelength considered in the case of a ring with radius 7.5 $\mu m$*

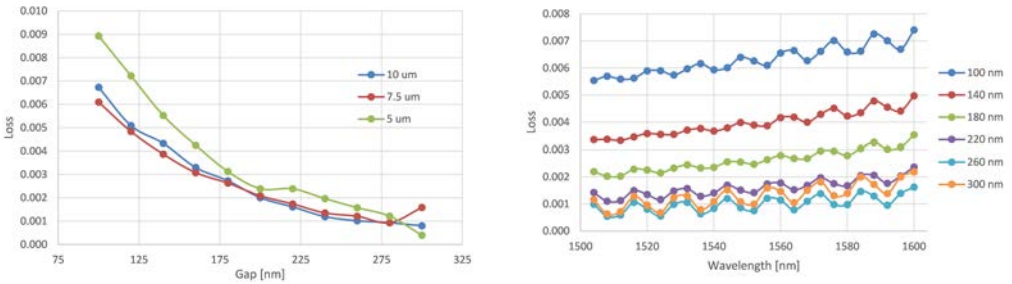


(a) Loss vs gap (b) Loss vs wavelength

Figure 6.9: *Loss due to the coupling region in the case of a ring with radius 7.5 $\mu m$*

in the other case, as the curve has a remarkably steeper slope as a function of the wavelength.

Similar results can be found in [7]. Here the coupling is between two waveguides which are not bent; however, the same pattern can be extracted, with a minor coupling in relation to short wavelengths and gaps. In addition, by comparing the cross-coupling coefficient per length with the values extracted in this thesis work, a certain affinity can be observed (for instance, as regards the 195 nm gap it is around 0.11 $^1/_{\mu m}$ and when considering that the ring is large in size the results are comparable).

## 6.3 Mode overlap

When a waveguide is bent, the mode profile experiences a certain degree of mismatch due to the curvature of the waveguide, resulting in higher losses

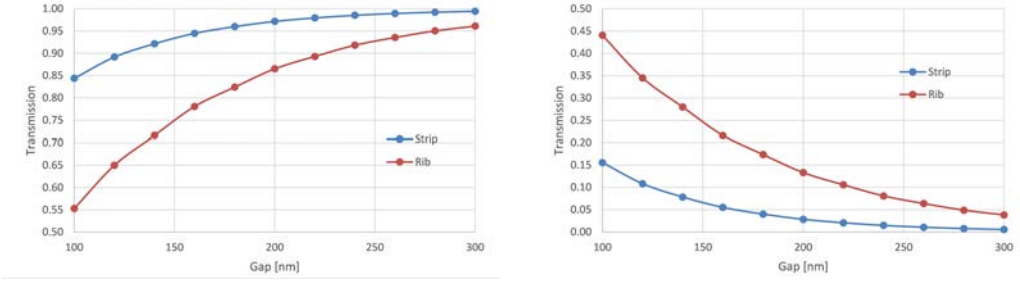


(a) Self-coupling coefficient (b) Cross-coupling coefficient

Figure 6.10: *Coupling coefficients for 1556 nm light and a 10 $\mu$m radius ring in the case of strip and rib waveguides*

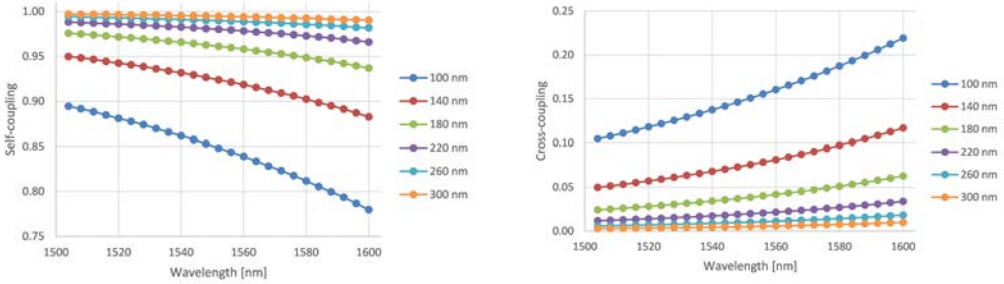


(a) Self-coupling coefficient (b) Cross-coupling coefficient

Figure 6.11: *Coupling coefficients for different wavelengths and gaps in the case of a strip waveguide*

because of leakage in the cladding. In figure 6.12, the difference between a straight waveguide and a bent one with radius 5 $\mu$m is presented. The bent waveguide tends to expel the light, which results in a defective match.

The overlap coefficient, displayed in figure 6.13, tells how much the mode is faithful to its original shape. The calculation is made by analyzing a quasi-TE mode at 1550 nm while varying the silicon area of the structure, namely the height and the width of the lateral slabs. In particular, the more the light is allowed to laterally spread, the more it is prone to optical mismatch when the ring radius is reduced and therefore for 1 $\mu$m lateral slabs more data points are collected in order to increase the quality of the result.

As regards the actual loss due to the bending mismatch, the calculation is carried out looking at the following formula

$$Loss\,[dB] = -20\log_{10}(overlap)$$

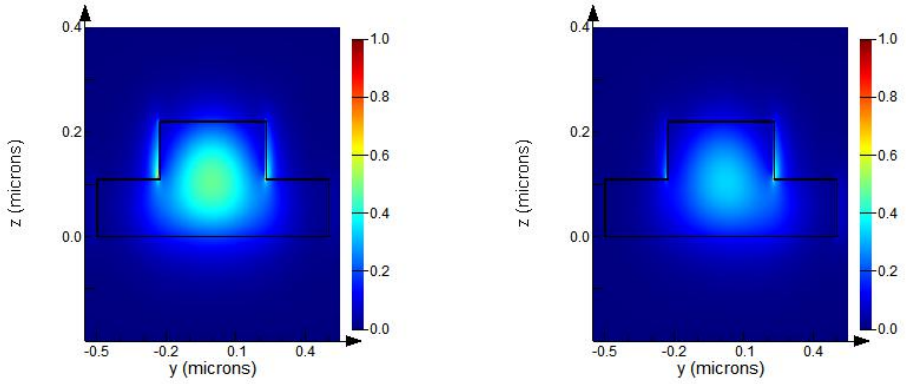


(a) Straight waveguide (b) Bent waveguide with radius 5 $\mu$m

Figure 6.12: *Field pattern difference in the case of a straight and of a bend waveguide for a 1 $\mu$m wide and 110 nm high slab*

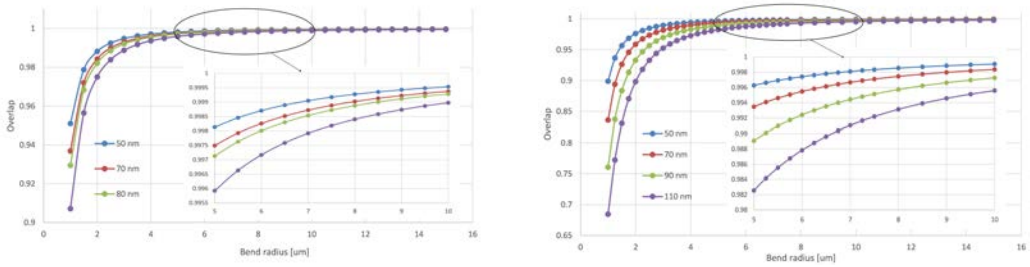


(a) 700 nm slab width (b) 1 $\mu$m slab width

Figure 6.13: *Mode overlap versus ring radius for different heights of the lateral slab*

And the results are plotted in figure 6.14.

As we can see, the losses are quite low and almost constant for radii down to 5 $\mu$m, size at which they snowball reaching, for certain configurations, 3 dB, which is half the transmitted power. Consequently, we can conclude that rings with radii as small as 5 $\mu$m are still viable in terms of loss, with great increase of the FSR and other important parameters. In particular, the loss at common radius lengths (7-10 $\mu$m) are close to the ones considered in [7] (around 0.04 dB), proving the accuracy of the calculation.

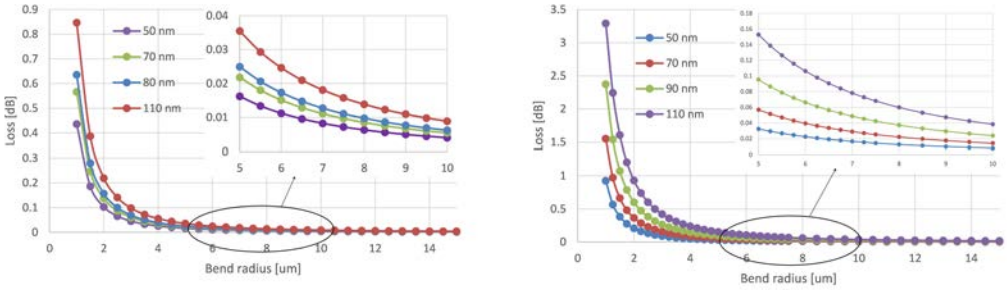


(a) 700 nm slab width

(b) 1 $\mu$m slab width

Figure 6.14: *Loss versus ring radius for different heights of the lateral slab*

## 6.4 Modulator

In this section, the modulating component of a silicon ring resonator is studied with respect to different physical parameters. The modulator chosen is the carrier-injection-based pin diode and as such the applied voltage is positive. The structure, that can be seen in figure 6.15, is a cross section of the ring (the raised structure in the center of figure 6.15 (a)) and it comprises two electrodes (anode and cathode, in dark grey in figure 6.15 (a)) arranged on top of two highly doped silicon pedestals. The silicon regions are conterminous with two smaller elongated silicon slabs connecting together at the center (where the waveguide is placed) and the background material is $SiO_2$. As regards the physical dimensions, the optical waveguide has height $L$ of 450 nm and width $T$ of 220 nm. The lateral slab height $h$ is initially set to 110 nm while the width $w$ is 1.7 $\mu$m. Lastly, the device is studied as it was straight (no bend applied in MODE solver).

The procedure employed to simulate and analyze the behavior of the modulator is the following. First, with Lumerical DEVICE, the carrier distribution and consequently the variation in the refractive index (see section 4.3.3) are calculated for a fine grid of points around the central waveguide by sweeping over a range of voltages to simulate the current flowing in the pin diode. Other parameters that are saved in this step are the charge density (both in the structure in its entirety and the value in the waveguide) and the current density. Afterwards, the refractive index distribution is loaded on Lumerical MODE where calculations related to light propagation in the device are carried out. The values of the refractive index for different levels of the applied voltage are retrieved in this step. From the refractive index one can directly derive the difference in the refractive index and the loss caused by the carriers in the channel.

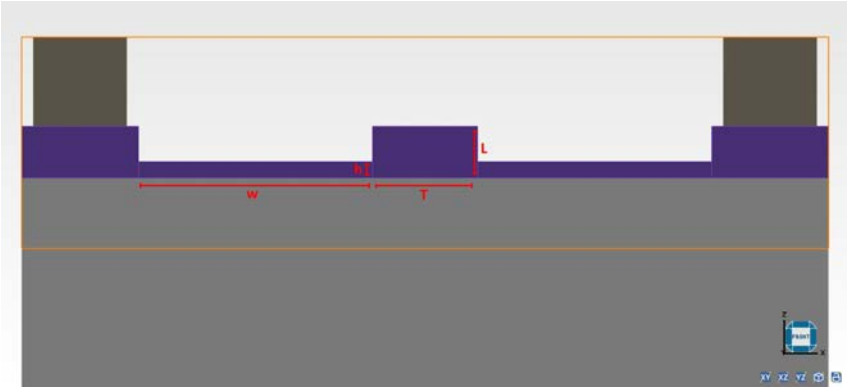


(a) DEVICE version

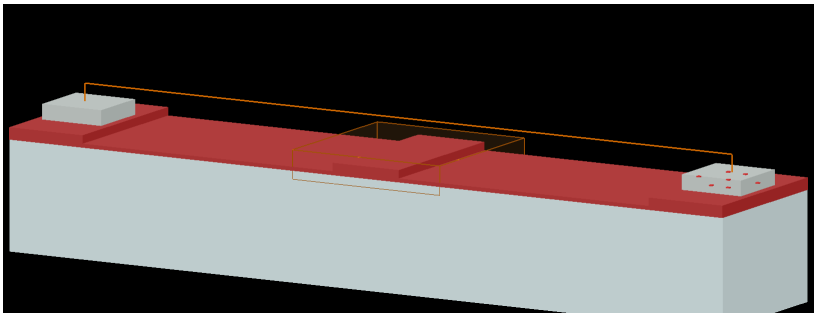

(b) MODE version

Figure 6.15: *Device under studying. The cladding has been removed for clarity purposes*

### 6.4.1 Intrinsic region width

The first parameter to have been studied is the width of the intrinsic region. In this particular case, the doping is set to be homogeneous in different areas, as explained in table 6.1.

The background doping is set to a lower value compared to other simulation setups found on the Lumerical website (with value of $10^{15}$) because that level of doping was seemingly too high for being an intrinsic region (which is usually only lightly doped). However, a further analysis has been carried out sweeping over different background dopings in section 6.4.5 for a different model structure. The contact regions are heavily doped since they are touching the metal electrodes and a low series resistance has to be achieved.

The constant doping model is not realistic but it is a good starting point to evaluate the performance of the device in order to choose the best configuration possible. Starting from section 6.4.4, however, the constant doping has been substitute with a more realistic diffusion doping profile. A glimpse

Table 6.1: *Doping concentration*

| Region | Concentration | Type |
|---|---|---|
| Contact region | $10^{20}$ | n/p |
| Slab region | $10^{18}$ | n/p |
| Background | $10^{13}$ | n |

of the doping distribution around the waveguide is provided in figure 6.16 for different voltage levels.

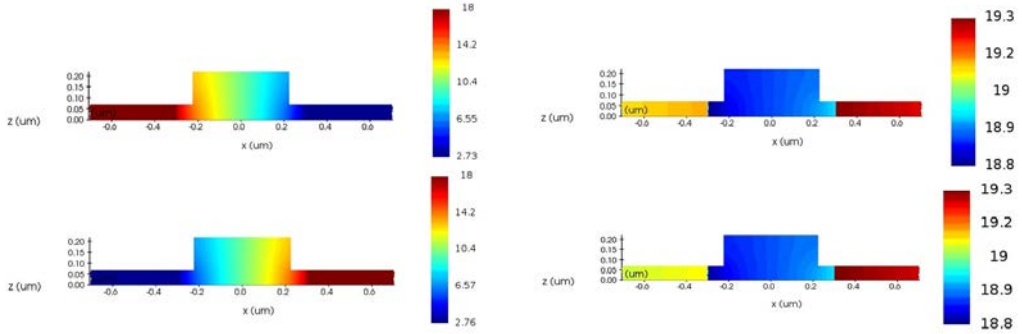


(a) 0 V applied (b) 2 V applied

Figure 6.16: *Doping profile in dB at the center of the device. n doping on top, p doping at the bottom*

Another unrealistic parameter is the voltage, here spanning from 0 to 3 V, which is an overly high value with respect to the physical size of the ring and the objective of the modulation. Starting from section 6.4.4, however, the sweep has been reduced spanning from 0 to 2 V, which is more practical.

First of all, the results obtained by using DEVICE are analyzed in figure 6.17. The charge density (since the monitor used is 2D) is retrieved considering both the entire structure (a) and focusing on the waveguide area (b). The behavior resembles that of a diode since we have a steep increase in the carriers when the voltage exceeds 0.75 V, which is arguably the threshold voltage of the diode.

Afterwards, by using MODE, the refractive index is retrieved and in figure 6.18 its modulation is presented for both real (n) and imaginary (represented by the linear loss factor $\alpha$) part. As we can see in (a), the refractive index difference increases when the intrinsic region width is reduced, because there is more current flowing in the device leading to a greater carrier concentration.

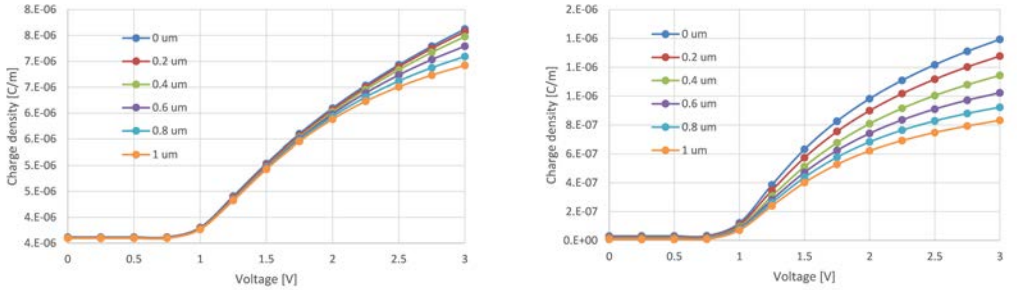


(a) Charge density in the entire device (b) Charge density around the waveguide

Figure 6.17: *Charge density in the device versus the applied bias*

However, the modulation in the case of 1 V applied is small compared to the others because the diode is still not fully turned on, as it is more evident in (b) where the diode influence on the data is clear, since the values are really low up to 0.75 V and increase rapidly afterwards. In particular, the focus on the low voltage regime is highlighted in the inset. Here it is possible to notice that the loss due to the carriers when there is no to little voltage applied depends heavily on the width of the intrinsic region. For modulation purposes, the loss at 0 V should be as low as possible, and therefore in light of the data collected all the subsequent measurement will employ a structure for which the intrinsic region width is 0.6 $\mu$m.

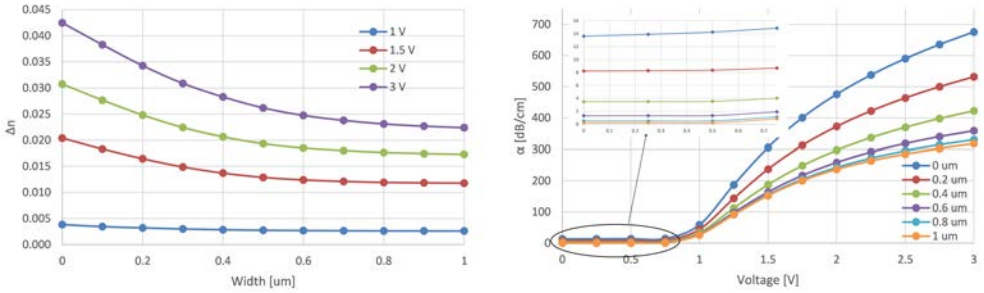


(a) Variation in n versus intrinsic region width for different voltages (b) Linear loss versus applied voltage for different intrinsic region widths

Figure 6.18: *Refractive index change and loss with focus on the intrinsic region width and its variation*

### 6.4.2 Lateral slab height

The next step, once the intrinsic region width has been set to 600 nm, is to determine the best height of the lateral slabs. All the remaining modeling parameters are taken equal to the previous step, except for the background doping which is now n type. In figure 6.19 the current density is plotted against the voltage applied and the different slab heights. As expected, the behavior is still diode-like with threshold somewhere around 1 V. It is immediately noticeable that higher lateral slabs result in an increased current and charge density (since the current monitor is in 2D) present in the device. It is also important to point out that the dependence of the charge density on the sweeping parameter is more pronounced in this case than in the previous analysis, due to the larger length of the lateral slabs compared to the increased number of carriers due to a narrowing of the intrinsic region.

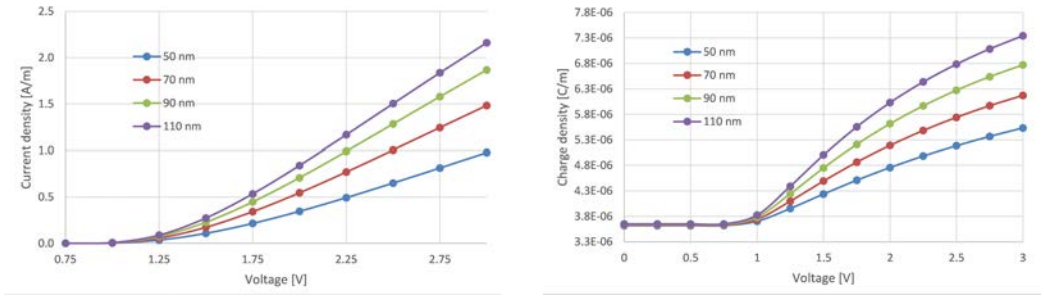


(a) Current versus voltage

(b) Charge density (in the entire device) versus voltage

Figure 6.19: *DEVICE results for different slab heights*

As regards MODE, figure 6.20 depicts the behavior of the refractive index with different heights and voltages applied. Again, the real part of the refractive index is better modulated when high currents flow and therefore with high lateral slabs. At the same time, however, we can see that when the slabs allow the light to spread more, the overlap with the carriers is larger and therefore the loss at low bias (below threshold) increase (b). This again is the major discriminating factor ruling out overly high lateral slabs, responsible also for an increase in the current and the charge in the device and consequently worsening the speed and the energy consumption of the device. Because of this, a reasonable slab height of 70 nm is chosen for the next steps.

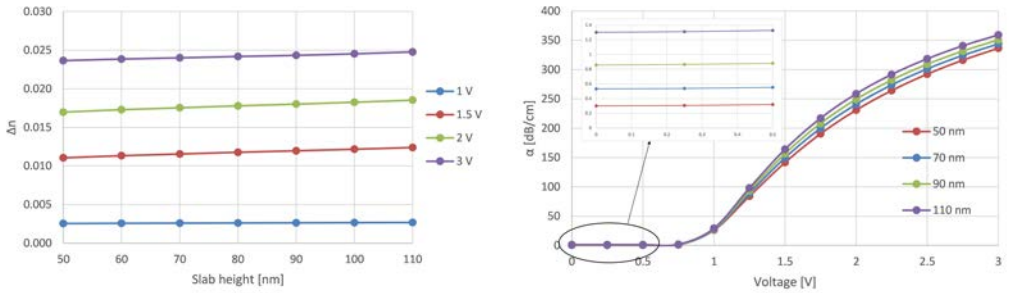


(a) Difference in n due to different heights and voltage

(b) Linear loss versus applied voltage for different slab heights

Figure 6.20: *MODE results for different slab heights*

### 6.4.3 Slab width

In this case the current flowing in the device is higher than in the previous two sections and as a consequence additional voltage steps have been employed in order to let the CHARGE simulator in DEVICE converge, for a total of 25 data points (instead of the previous 13). The width range spanned in this simulation goes from 0.7 to 1.7 $\mu$m.

As regards DEVICE, the charge density is plotted in figure 6.21. The results are consistent with the previous calculations.

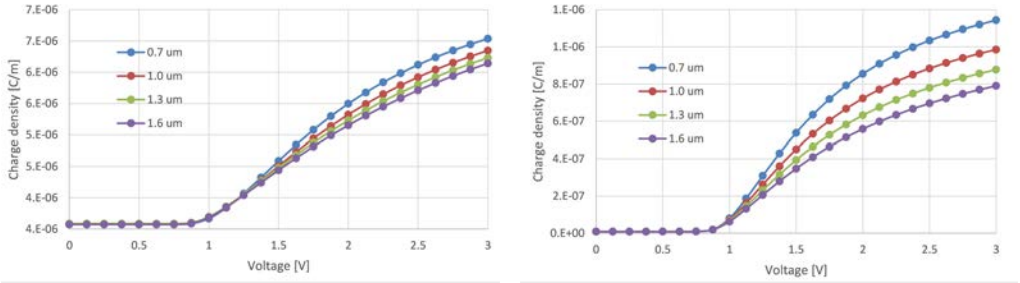


(a) Charge density of the entire device

(b) Charge density around the waveguide

Figure 6.21: *Charge density versus voltage for different widths*

With MODE the refractive index variation and loss are evaluated as can be seen in figure 6.22. First of all, in (a) it can be seen that by reducing the distance between waveguide and electrodes the modulation capability strongly increases. At the same time, in (b), the linear loss follows the same principle, but for widths of less than 1 $\mu$m it becomes prohibitive at small bias (at 0.7 $\mu$m we have almost four time the loss experienced at 1 $\mu$m). For

this reason the next steps evaluate the behavior of the device for larger slab widths.

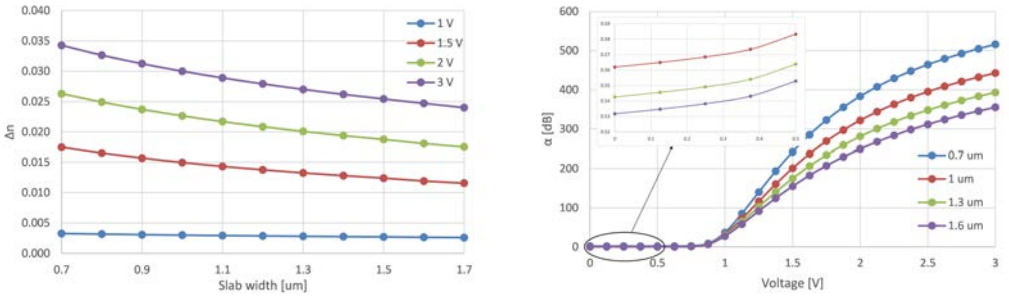


(a) Variation of n versus slab width for different voltages

(b) Linear loss versus voltage for different slab widths

Figure 6.22: *MODE analysis of the device*

### 6.4.4 Doping concentration

A further improvement can be represented by a more realistic doping profile. DEVICE allows to set up a diffusion kind of doping starting from a surface (see section 5.2.1). In this section, the background doping is still set as constant and its type and concentration are the same as the previous steps. However, doping diffusion has been simulated starting from the contact region and the lateral slab. In particular, the diffusion profile has been set to Gaussian and the doping intensity spans from $10^{19}$ to $1.5 \cdot 10^{20}$ cm$^{-3}$ in the case of the contact doping and from $10^{17}$ to $1.5 \cdot 10^{18}$ cm$^{-3}$ in the case of the slabs (from now on, 0.1 to 1.5 using as reference concentration (that is, 1) the case $10^{18} - 10^{20}$ cm$^{-3}$). Three different slab widths have been analyzed, namely 1 $\mu$m, 1.35 $\mu$m and 1.7 $\mu$m (shorter versions have previously been discarded in section 6.4.3). In figure 6.23 the doping profile of the area around the waveguide is charted with reference to the longest slab and for different voltage levels.

To show the general behavior of such a device, in figure 6.24 and 6.25 the electrical and optical main properties for the 1.35 $\mu$m case are shown (the behavior of the other two configurations is alike). In particular, it is immediately noticeable that an increase in the doping corresponds to a more effective modulation (figure 6.25 (a)) and consequently a more pronounced linear loss (figure 6.25 (b)). At the same time, as expected, both the current and the charge density in the waveguide increase (figure 6.24 (a) and (b) respectively), although for the former a quite noticeable saturation can be seen

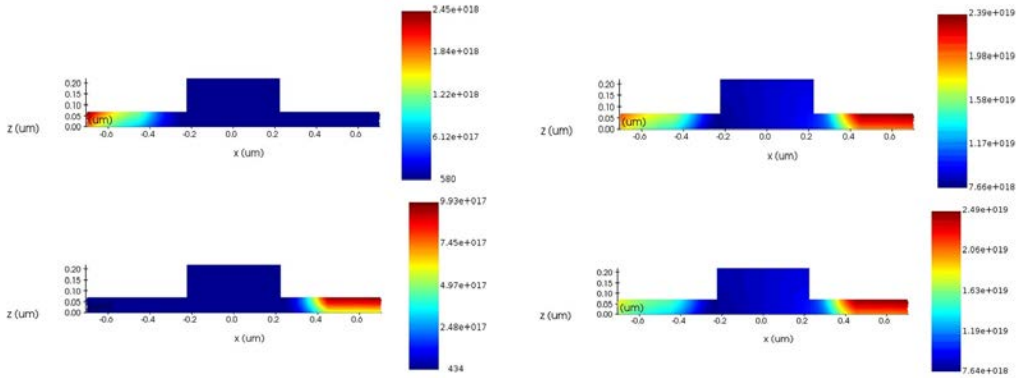

(a) 0 V applied (b) 2 V applied

Figure 6.23: *Diffused doping profile in the center of the device. n doping on top, p doping at the bottom*

for high values of the doping concentration (when more than 1.1). Interestingly enough, it seems that the slope of the curve representing the variation of the refractive index decreases with a bias larger than 1.5 V, indicating a possible saturation of the device at high voltages.

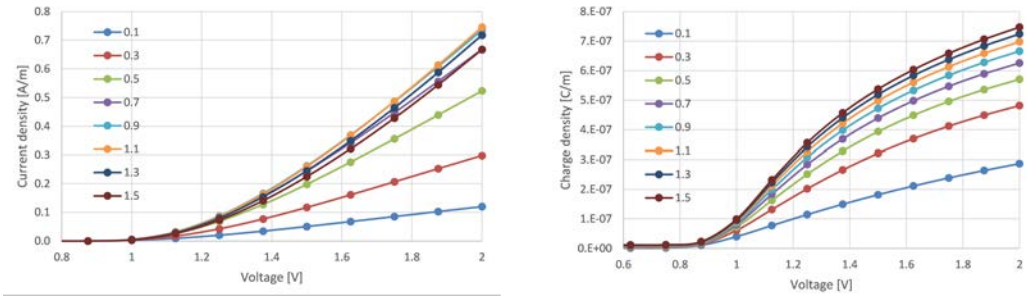


(a) Current density versus voltage for different doping levels (b) Charge density in the intrinsic region versus voltage for different doping levels

Figure 6.24: *DEVICE data in the case of a 1.35 μm wide lateral slab (values in the legend to be multiplied by* $10^{18}$ *or* $10^{20}$ *accordingly to the region)*

At the same time, when depicting the optical properties versus the doping concentration, one can deduce that the modulation capability flattens with high level of doping as well (figure 6.26). In particular, in (a) the plotted modulation capability shows a steep increase when the doping level is low, but it quickly stabilizes (especially when less voltage is applied). In (b), the linear loss shows a similar behavior.

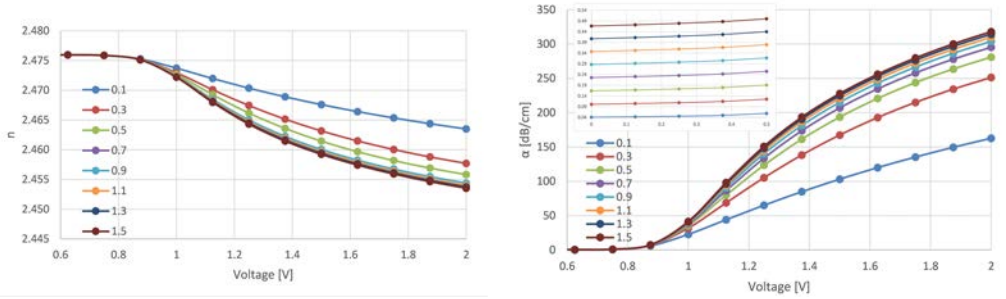


(a) Variation in n versus voltage for different doping levels

(b) Linear loss versus voltage for different doping levels

Figure 6.25: *MODE data in the case of a 1.35 $\mu m$ wide lateral slab (values in the legend to be multiplied by $10^{18}$ or $10^{20}$ accordingly to the region)*

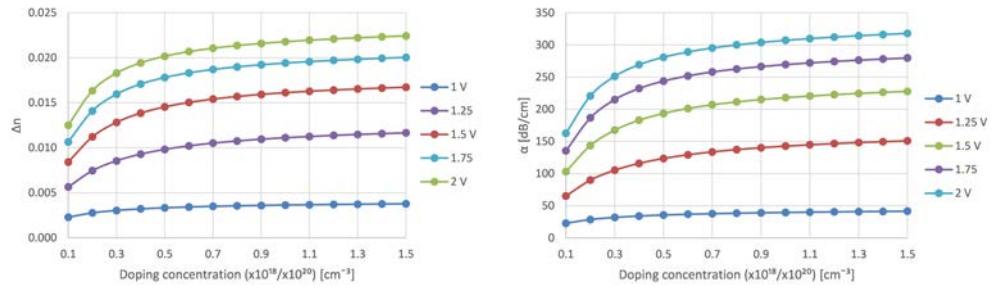


(a) Variation in n at different bias

(b) Linear loss at different bias

Figure 6.26: *Optical properties displayed versus doping concentration*

From the results above, as a rough approximation it is possible to claim that a bias higher than 1.5 V does not result in a significant modulation advantage and it is therefore to be ruled out. Nevertheless, below 1.5 V the diode is not fully on and a much larger improvement can be achieved by increasing the voltage. Analogously, in the case of the doping concentration, when it is below a certain threshold a large gain is recovered by increasing the diffusion intensity while if it is excessive it will be close to useless modulation-wise but detrimental when it comes to the loss at zero bias (see the inset in figure 6.25 (b)) and the total amount of charge in the device (figure 6.24 (b)). Moreover, at the same time the current behavior becomes erratic (figure 6.24 (a)), therefore meaning that high doping profiles have to be avoided.

It is also important to point out that the results obtained so far are compatible with the ones previously retrieved with a costant doping profile, but they are slightly worse due to the more realistic doping profile which

results in an overall less efficient modulation. Moreover, they are aligned to the Soref-Bennett equations (4.8) and (4.9) when substituting the carrier concentration of the formulae with an arbitrary reference value stemming from the concentration bar of figure 6.23.

The next step comprises the comparison between the three different widths. In figure 6.27 the linear loss at 0 and 1.5 V is considered. In particular, in (a) the loss is strikingly lower in the case of longer slabs. Interestingly, there is virtually no difference between the 1.35 $\mu$m and the 1.7 $\mu$m configurations. For useful doping concentrations in (b) the behavior is still the predicted one, with increasing loss while decreasing the waveguide/contact distance; however, once again the largest difference is found between 1.0 and 1.35 $\mu$m.

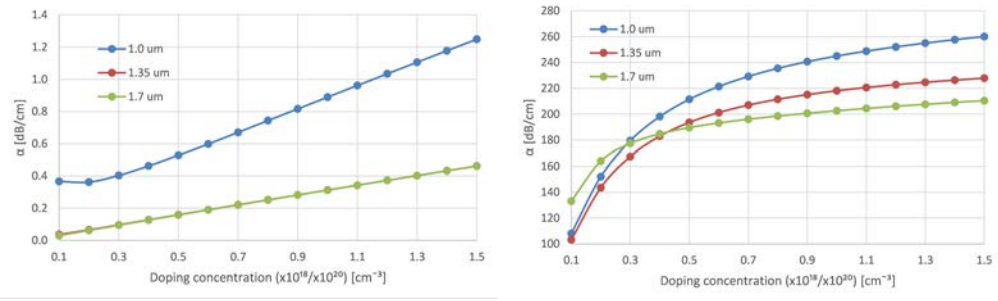


(a) Linear loss at 0 V

(b) Linear loss at 1.5 V

Figure 6.27: *Linear loss versus doping concentration for different widths considered*

In figure 6.28 the real part of the refractive index is analyzed at two different bias levels. Considering (a), it is possible to point out that there is almost no difference between the two longest devices. Furthermore, at very low doping concentration the 1.7 $\mu$m version has the upper hand compared to both the others and retains the advantage over the 1.35 $\mu$m long slabs up to doping levels of 0.9. When the diode is fully turned on at 1.5 V (b), however, the medium-sized device catches up earlier at concentrations around 0.4. The short slabs have definitely the advantage, even though at the expense of a higher overall loss.

Consequently, the current output of the device is studied in figure 6.29. The curves are similar for both devices, even though the scale in the y-axis is of course different. As already pointed out by looking at figure 6.24, at high doping concentrations the current behavior is somewhat erratic since it shows an interesting decrease which is less pronounced at high bias or short size of the device. In particular, the 1.0 and 1.35 $\mu$m versions display a quite similar behavior and are preferable in this regard considering that higher currents

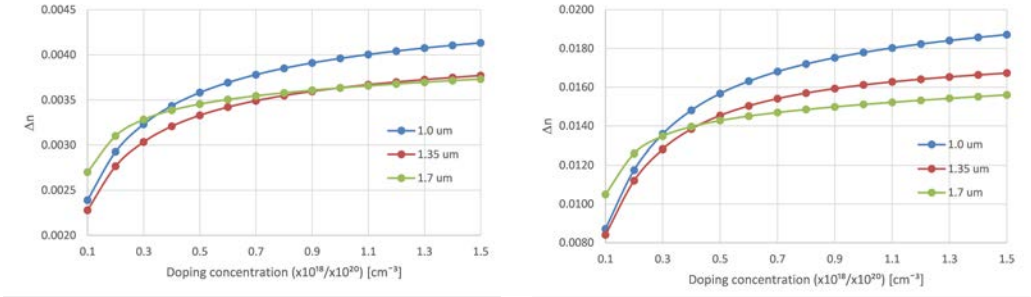


(a) 1 V applied (b) 1.5 V applied

Figure 6.28: *Variation in n versus doping concentration for different widths*

result in less series resistance and thus increasing the modulation speed of the device, although the downside is a more detrimental power consumption.

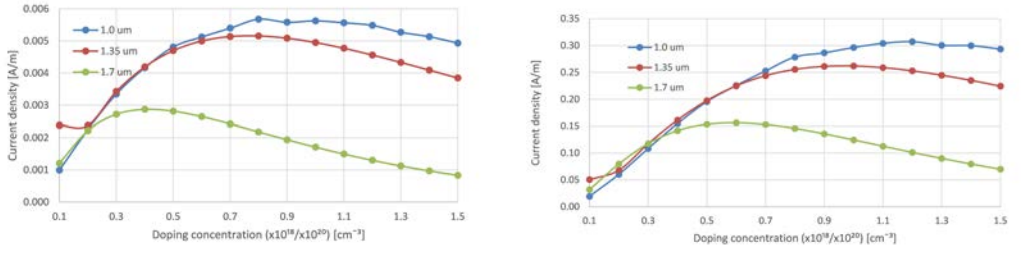


(a) 1 V applied (b) 1.5 V applied

Figure 6.29: *Current versus doping concentration for different widths*

As regards the charge, figures 6.30 and 6.31 show the charge density around the intrinsic region and the structure in its entirety respectively. Clearly, a larger device has the drawback of a sizeable amount of charge, resulting in a more deleterious RC constant. As expected, denser doping concentrations increase the amount of charge. It is interesting to point out that both the 1.35 and 1.7 $\mu$m configurations are fairly similar and the amount of charge is quite comparable.

Afterwards, the resistivity and capacitance of the junction are calculated for the 1.35 $\mu$m wide slab version and the result is reported in figure 6.32. When comparing with [89], the capacitance is seen to be similar, while the resistance (calculated by considering a ring of radius 7.5 $\mu$m) is 3 to 4 orders of magnitude different. However, when compared to [8] or the results obtained in [106], the resistivity is found to be $\simeq$ 0.1 V·cm which corresponds to the values depicted in (b). It is not clear why such a discrepancy in the data

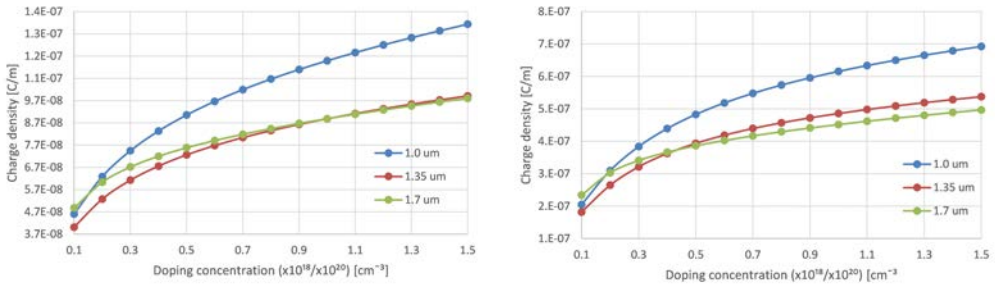


(a) 1 V applied (b) 1.5 V applied

Figure 6.30: *Charge around the intrinsic region versus doping concentration for different widths*

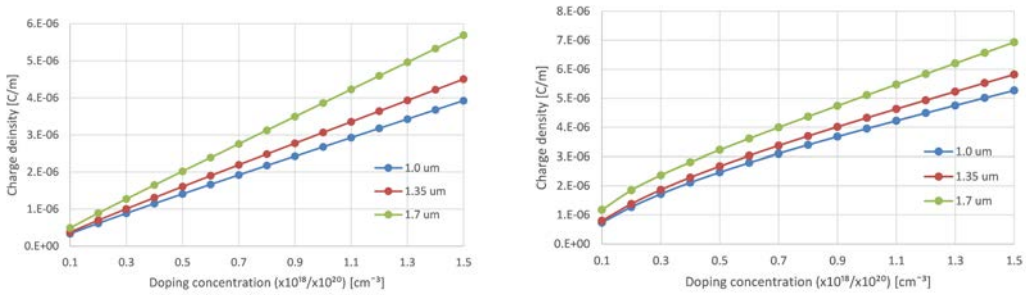


(a) 1 V applied (b) 1.5 V applied

Figure 6.31: *Charge in the entire device versus doping concentration for different widths*

is retrieved, however the electrical bandwidth calculated with formula (5.13) appears to be overly low when considering the RC constant recovered with the data shown in figure 6.32.

Subsequently, some important parameters, such as quality factor, finesse, FWHM, FSR, $V_\pi L$ and ER are addressed and discussed. The data has been collected by means of MATLAB scripts. To retrieve the data, the formulas presented in sections 4.4 and 5.1 have been employed by considering a 7.5 $\mu$m long radius (a more thorough analysis of the influence of the bending on the device is carried out in section 6.4.6). Some parameters have been chosen regarding the physical structure of the device. For instance, the usual linear loss of the silicon waveguide has been set to 4.343 $^{\mathrm{dB}}/_{\mathrm{cm}}$, which is an educated guess (see section 5.2.2). At the same time, the active region in which the modulation takes place has been limited to 65% of the total ring perime-

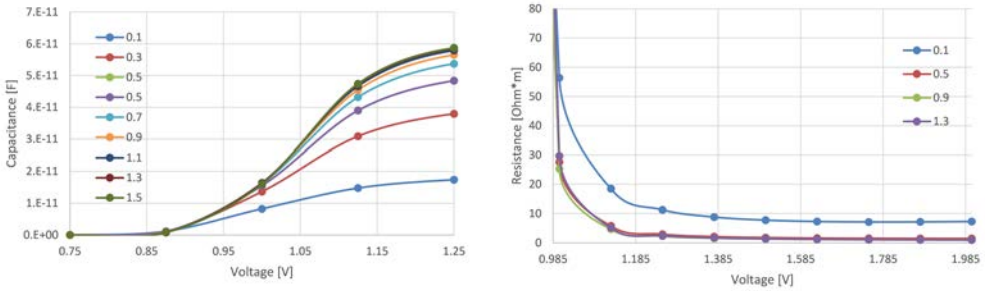


(a) Capacitance per meter (b) Resistivity

Figure 6.32: Electrical parameters in the case of 1.35 $\mu$m wide lateral slabs

ter, to allow an easy and noise-impervious coupling with the input/output waveguide (see figure 6.47). The initial value of the self-coupling has been chosen so that to be in the critical coupling condition (and therefore equal to the single-pass amplitude transmission of the ring).

In figure 6.33 the behavior of quality factor and finesse is plotted for different doping concentrations. It can be seen that these two parameters are larger with high doping and tend to decrease rapidly as the diode turns on. A comparison can be made with [107], in which a ring of radius 6 $\mu$m is considered. The quality factor is reported there as 39.350 which is lower than the one in (a) when no bias is applied but, pointing out that the ring is smaller and considering the behavior of the quality factor with respect to the cavity length (see section 5.1), it is possible to infer that the result is achievable.

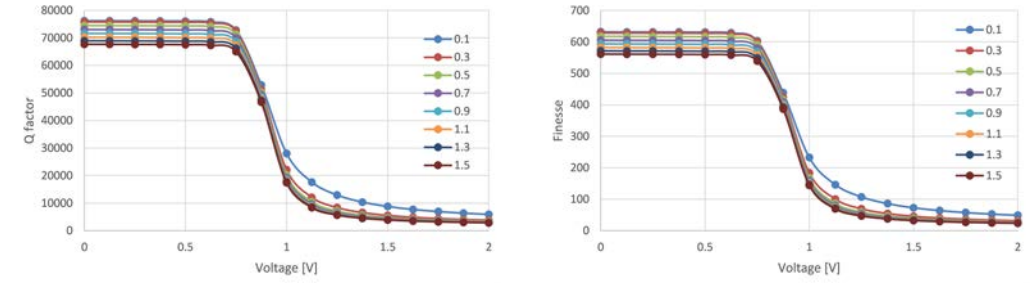


(a) Q factor for different doping levels (b) Finesse for different doping levels

Figure 6.33: *Q factor and finesse versus voltage in the case of 1.0 $\mu$m wide slabs*

Moreover, in figure 6.34 the FSR and the FWHM are shown with respect

to the doping concentration and compared at different lateral slab widths. Both parameters worsen with increasing doping, the FSR being smaller (due to a slight increase in the group index) and the FWHM being larger (broader resonances). It is also important to point out that the smallest device degrades at a larger rate compared to the other two configurations that are rather interchangeable. In the case of the FWHM, in [107] it is reported a value of 0.04 nm, which is comparable with that in (b) even if the ring in said paper has a radius of 6 $\mu$m.

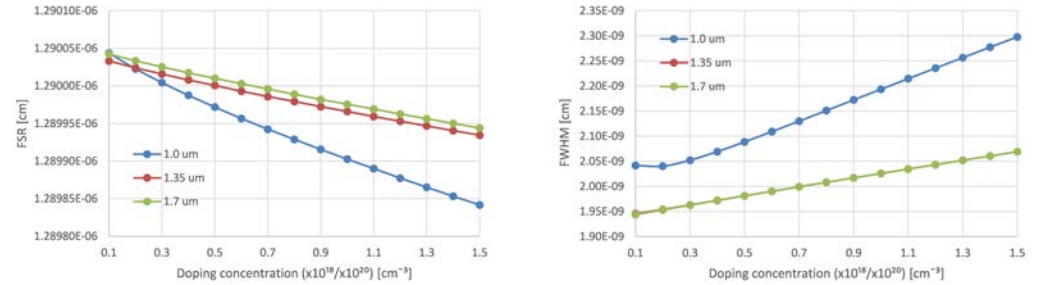


(a) FSR for different slab widths

(b) FWHM for different slab widths

Figure 6.34: *FSR and FWHM versus doping concentration*

As regards the FOM $V_\pi L$, calculated using formula (5.14), the results obtained at two different voltage levels, namely 1 V and 1.5 V, are shown in figure 6.35. The values are significantly better for the 1.5 V case, since the diode is fully turned on and the modulation more effective. As a general trend, higher doping concentrations result in better performances, with the 1.0 $\mu$m wide device obtaining the best results. The results are certainly realistically achievable, since for instance in [8] values even lower (namely 0.0025 V·cm) are reported. In [102], the modulation efficiency is revealed to be 0.011 V·cm, which is quite similar to what has been charted in figure 6.35.

The ER, calculated as the difference in dB between the peak of the resonance and the maximum value of the transmission, is depicted in figure 6.36 for two different voltage levels, namely 0.75 V and 1 V. Larger voltages are not considered since the parameter flattens quickly to small values. Interestingly, two opposite behaviors are recovered. In the case of the small bias, the ER is found to increase with the doping concentration. When the diode is properly turned on, however, it is seen to decrease. Furthermore, in figure 6.36 (a) there is a remarkable difference between the short and the long devices, the former performing better. In (b), on the other hand, they seem to behave quite similarly. A striking contrast is recovered for such a

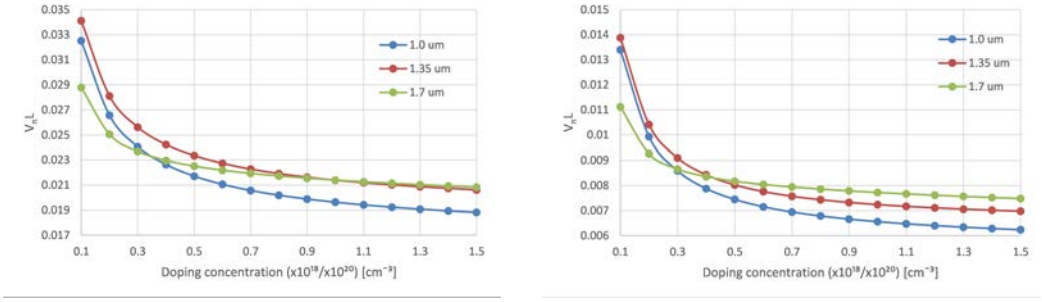


(a) 1 V applied (b) 1.5 V applied

Figure 6.35: *$V_\pi L$ versus doping concentration for different slab widths*

small bias difference, meaning that the parameter is extremely sensitive to the concentration of free carriers in the waveguide.

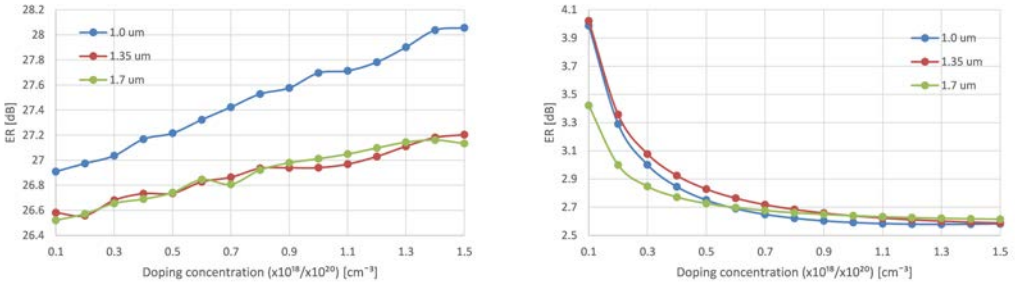


(a) 0.75 V applied (b) 1 V applied

Figure 6.36: *ER versus doping concentration for different slab widths*

In light of the previous analysis, the optimal configuration found is the 1.35 $\mu$m wide. Not only is the loss at zero bias low (figure 6.27 (a)) and the current comparable to the shorter configuration (figure 6.29), but also the total amount of charge is close to that of the 1.7 $\mu$m device (so that there would be no advantage in choosing the latter) and important parameters such as FSR and FWHM do not degrade as fast as in the shortest device. Moreover, the footprint is significantly less pronounced than in the latter case. When it comes to the applied voltage, it will be set to less than 0.9 V for the "on" state. It is true that the diode is not fully on and further bias will result in a large improvement of the refractive index action. However, based on the parameters calculated in figures from 6.33 to 6.36, the bias has to be set lower since an effective modulation is already performed at lower voltages (see figure 6.48) and these parameters generally worsen with more

bias applied. Furthermore, it is possible to lower the power consumption and the wear of the device. As regards the doping concentration, the 1.0 setup is arguably the best one because it does not suffer from excessive loss when "off" and at the same time it does not enter the regime in which the current saturates (figure 6.29 (b)).

### 6.4.5 Background doping level

Subsequently, the problem about the constant background doping level (pepi) concentration is addressed. In this regard, both n and p doping types are considered. Their concentration spans from $10^{13}$ to $1.5 \cdot 10^{14}$ cm$^{-3}$ (from now on, 1 to 15 using as reference concentration (that is, 1) the case $10^{13}$ cm$^{-3}$). It is important to point out that the background doping has effect only on the core intrinsic region because the heavily doped lateral regions are not affected by such a small variation of the carrier density.

In figure 6.37 the electrical properties are charted. In particular, the current and the charge density are plotted for both n and p background doping. However, no noticeable difference has been found, the two doping types being virtually equivalent. By increasing the doping, though, an important factor becomes noticeable: the current tends to slightly decrease.

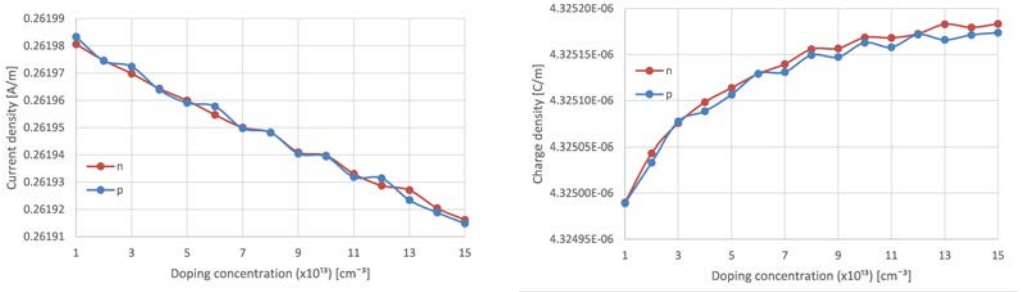


(a) Current density for both n and p doping (b) Charge density for both n and p doping

Figure 6.37: *Electrical properties at 1.5 V for different doping levels*

An interesting finding, which can be seen in figure 6.38, is that the loss at zero bias is lower in the case of p doping, the result being explained by the reduction of n carriers in the channel (which are the most effective in increasing the absorption coefficient, see figure 4.5 (b)), as depicted in (b). The data suffers from some oscillations due to inaccuracies of the solver, but the overall trend is readily extrapolated. It is important to notice, however, that at low background doping levels the two values converge.

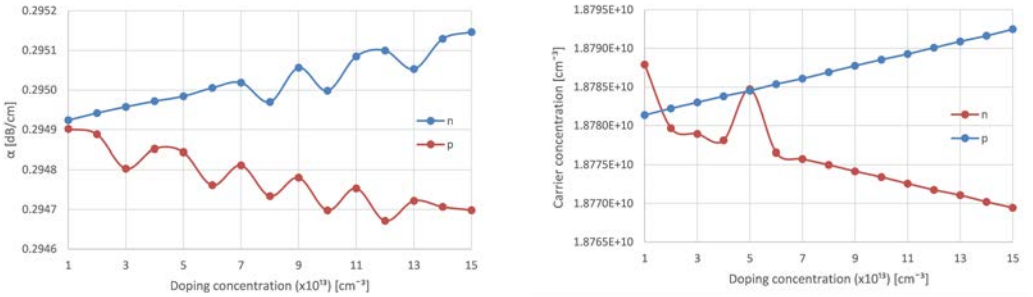


(a) Linear loss for both n and p background doping

(b) p free carrier in the intrinsic region for both n and p background doping

Figure 6.38: *Loss and carrier concentration for different doping levels*

The last observation can be made regarding the modulation capability and the variation of the real part of the refractive index. As shown in figure 6.39, in the case of low voltages there is no noticeable difference between the two types of doping. With increasing voltage, however, there is a slight advantage when using n doping. This advantage becomes more clearly detectable as the background doping concentration increases.

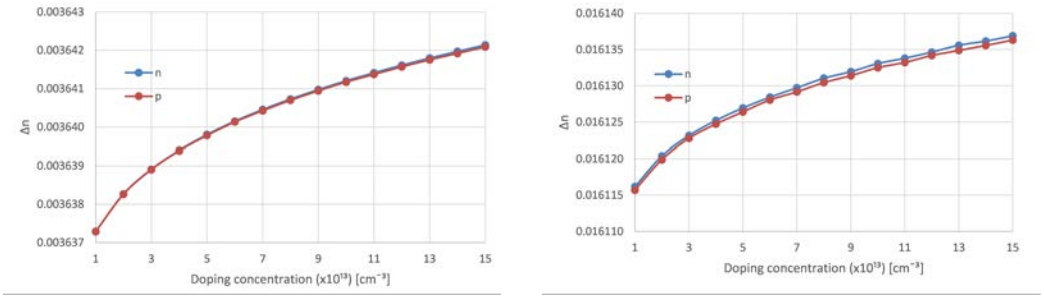


(a) 1 V applied

(b) 1.5 V applied

Figure 6.39: *Variation in n due to the background doping*

To draw a conclusion, both n and p doping have their own pros and cons. Therefore, the original background doping (as in table 6.1) is maintained for the future chapters.

### 6.4.6 Bend

In this section the calculation made with MODE is repeated considering a bent structure (to simulate a section of the ring). The bending radius spans

from 5 to 10 $\mu$m (in order to avoid overly penalizing bend losses, see section 6.3). First of all, in figure 6.40, a quick comparison between bent and straight waveguides is made. First, it is possible to notice in (a) that by increasing the bend the refractive index is lower, while its modulation is almost constant. On the other hand, in (b), the linear loss is found to be virtually the same when the diode is turned on, but it substantially differs when considering low voltages only. The reason can be found in the lower mode confinement, such that the effective refractive index depends more on the cladding (and thus yielding to its reduction) and there is less overlap between free carriers and light (which in turn results in a lesser linear loss). Therefore, as a first conclusion, a small ring looks preferable. However, one has also to consider the loss due to the bend, as in section 6.3. As a consequence, a careful balancing is needed.

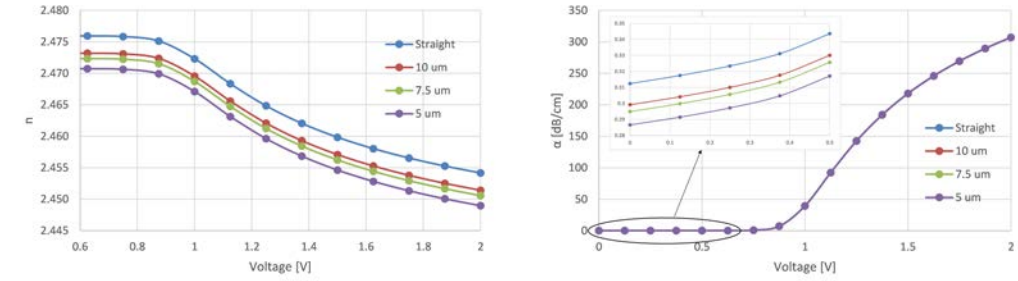


(a) Refractive index

(b) Linear loss

Figure 6.40: *n and linear loss versus voltage for different bend radius*

There is but a slight difference in the optical properties with increasing bending and therefore a direct visual comparison cannot be made. What is performed, however, is a differential analysis of the data, meaning that the difference in the refractive index and loss while decreasing the radius is performed in order to visually compare the effectiveness of considering a less sizeable device. In figure 6.41 the difference between the variation in n for different ring radii is plotted. The values are obtained by subtracting the variation of the refractive index between two consecutive radii, so that to obtain the improvement (or deterioration) of said parameter while decreasing the radius. In this case it is found that there is virtually no difference when considering the longest structures (the values are four orders of magnitude lower than the actual variation of n, see figure 6.39 (b)) to draw a comparison, while a more significative (though still small in absolute terms) gain in the modulation capability is found by diminishing the radius of the 1.0 $\mu$m wide lateral slabs. The main difference is retrieved for small radii, meaning that

the refractive index is altered more when reducing the size of the ring when it is already small.

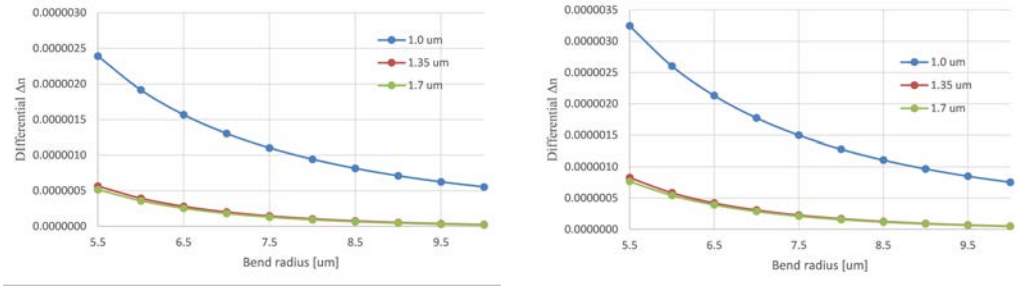


(a) 1.5 V bias (b) 2 V bias

Figure 6.41: *Differential variation in n versus the radius for different lateral slab widths*

Lastly, the differential loss is shown in figure 6.42. The procedure followed is the same as in the previous case and the results are similar as well, showing that the largest deviation is found for small rings. Here the absolute values are more significative when no bias is applied, being them around two orders of magnitude lower than the actual loss (while in the case of 1.5 V it is four). When comparing the improvement in the loss at zero bias with the increase in the overlap loss (see figure 6.14), however, they are found to still be overall negligible.

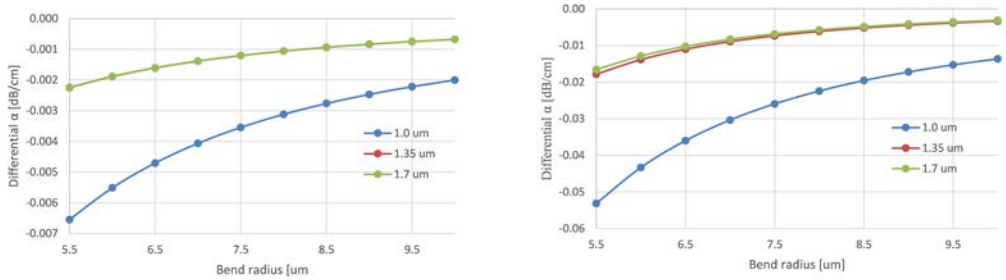


(a) 0 V applied (b) 1.5 V applied

Figure 6.42: *Differential loss versus the radius for different lateral slab widths*

To draw a cocnclusion, it is possible to claim that the analysis of the ring bend does not provide any possible significative improvement to the apparatus, whose radius has to be tuned by referring solely to overlap loss, FSR and other spectral parameters.

### 6.4.7 Frequency analysis

The last step regarding the study of the modulator is carried out by sweeping the analyzed wavelength from 1200 to 1650 nm (with 2 nm steps) in order to cover all the optical windows usually employed in optical communications (from the O-band starting at 1260 nm to the L-band ending at 1625 nm [108]). The model is the one chosen in the past sections and the main features are displayed in table 6.2. The physical properties are similar to those considered in [8] and [109].

Table 6.2: *Details of the chosen modulator*

| Property | Value |
|---|---|
| Intrinsic region width | 600 nm |
| Slab height | 70 nm |
| Slab width | 1350 nm |
| Doping concentration | $10^{18} - 10^{20}$ cm$^{-3}$ |
| Background doping (n type) | $10^{13}$ cm$^{-3}$ |
| Voltage applied | $< 0.9$ V |
| Ring radius | 7.5 $\mu$m |

When setting the MODE solver, however, a mistake has been made. With such a large bandwidth it is necessary to fit the material properties over several data points which are provided by Lumerical. Nonetheless, the fit chosen was too demanding and as a result a clearly wrong function for the imaginary part of the refractive index has been recovered, as shown in figure 6.43 (red square).

As a consequence, the data collected with reference to the imaginary part of the refractive index is not accurate since it will mirror the ghost resonance-like green curve (the real data points are the filled red squares at the bottom of the graph), as can be seen in figure 6.44 (a), where some values are surprisingly negative. At the same time, the error propagates in the calculation of the group index as well (figure 6.44 (b)).

On the other hand, however, the real part of the refractive index (green square in figure 6.43) is mostly correct except for a small lump around 1380 nm (where the huge resonance dip occurs in the case of the imaginary part). In figure 6.45 (a) n is plotted against the wavelength and it decreases steadily, as already pointed out in 3.4.2 (due to the rising overlap with the cladding).

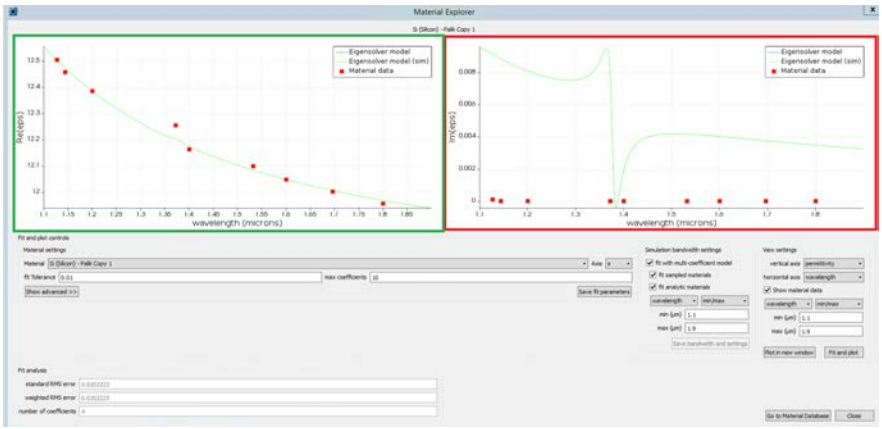


Figure 6.43: *Material settings in MODE*

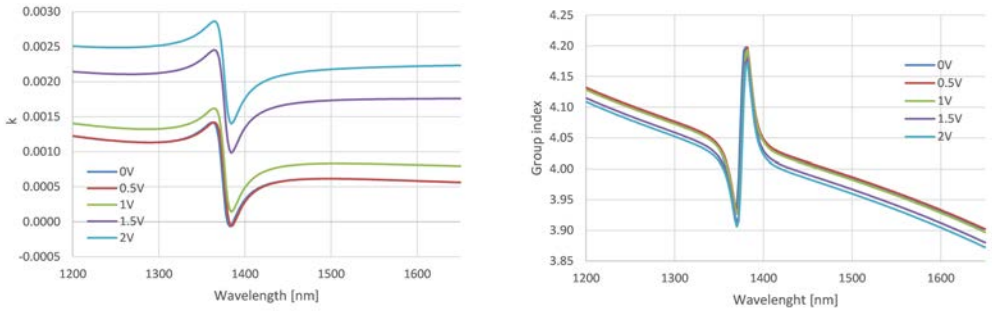


(a) k versus wavelength

(b) Group index versus wavelegnth

Figure 6.44: *Wrong parameters extraction for different voltage levels*

The result is similar to that of figure 6.40 (a), where the lesser overlap between core and propagating mode leads to a decrease in the refractive index. A comparison of the behavior can be made with [105], in which the same decline of the refractive index with the wavelength is reported. In addition, in figure (6.45) (b) the variation in the real part of the refractive index is plotted once more with reference to different widths of the lateral slabs. As expected, a small device results in a better modulation. However, with increasing wavelength it is less effective, the reason being the same as the previous case, that is, the minor ovelap between the light and the free carriers in the waveguide.

The decrease of $\Delta n$ becomes steeper with longer wavelengths and this conclusion is corroborated in figure (6.46), in which a differential analysis similar to the one carried out in section (6.4.6) is performed. First, it has to be pointed out that the oscillation is due to the misfit in the approximation

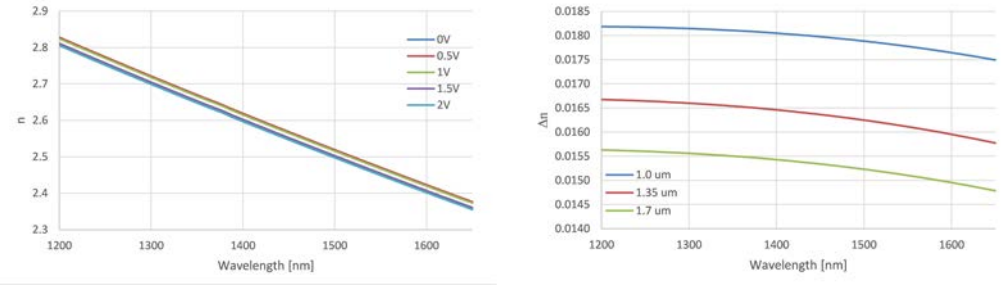


(a) n for five bias levels, 1.35 $\mu$m wide slabs (b) Variation of n at 1.5 V, different widths

Figure 6.45: *n and its varation versus wavelegth*

of the refractive index and has therefore to be overlooked. Thereafter, it can be seen that in the case of long wavelengths the improvement in the refractive index is larger while increasing the frequency in comparison with short wavelengths.

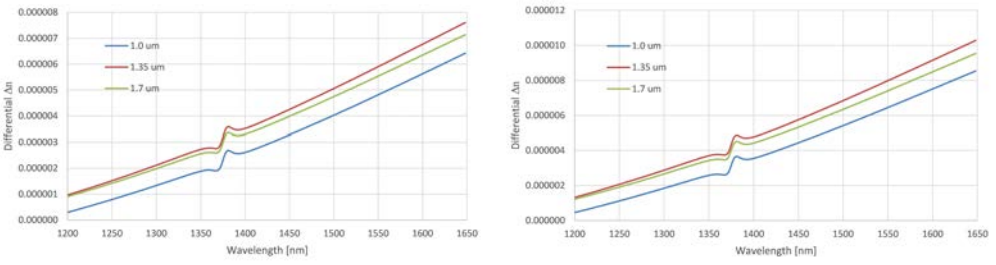


(a) 1.5 V applied (b) 2 V applied

Figure 6.46: *Differential variation in n*

### 6.4.8 Output spectrum

The ring modulator model of figure 6.47 is based on the parameters written in section 6.2 and the radius considered is the same as section 6.4.4, that is, 7.5 $\mu$m.

The output spectrum is calculated based on formula (5.4) and is shown in figure 6.48. The modulation is effective starting from 0.75 V, in which case the resonant peak is not overlapping with the one that is observable when no bias is applied. The ER is acceptable and since the diode is not fully turned on there is no massive power consumption.

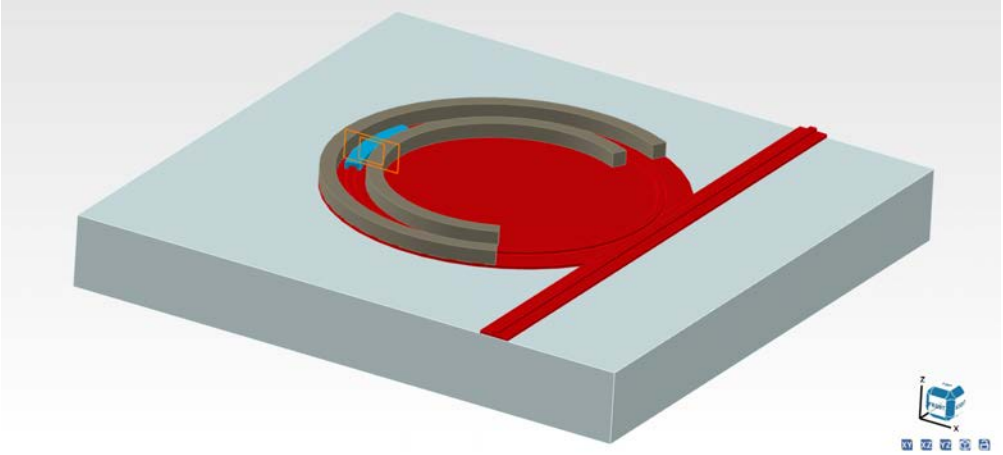

Figure 6.47: *Ring modulator*

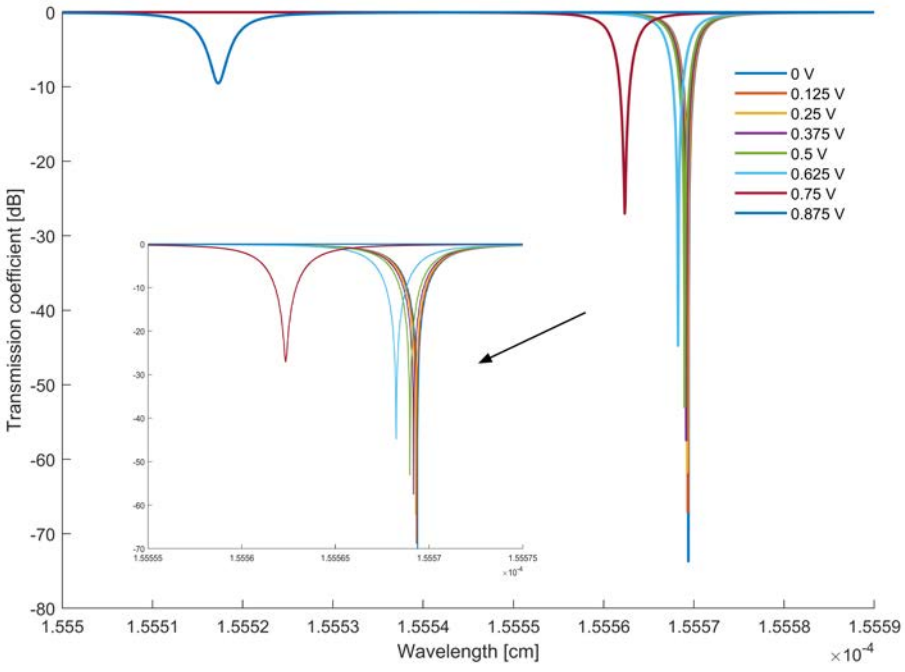


Figure 6.48: *Output spectrum*

# Chapter 7

# Conclusion

## 7.1 Summary

In this thesis work an overview of the basic electromagnetic theory and the main interactions between light and matter has been proposed, such as Maxwell's equations, light propagation, refractive index, interference, polarization and nonlinear effects. Particular focus has been given to waveguide propagation, starting from Snell's law and proceeding with an outline of mode propagation, dispersion and coupling. Follows an introductory chapter about modulators, in which the main parameters and modulation techniques are presented. In particular, the phenomenon the simulation is focused on is the plasma dispersion effect (free carrier concentration variation). Subsequently, ring resonators are thoroughly explained in terms of structure, fabrication processes, main parameters and applications, with focus on ring modulators which are the object of the thesis.

Finally, the results obtained with Lumerical and MATLAB are shown in chapter 5. First, the effective index method is used to evaluate how this parameter changes with the structure of the waveguide. An increase of the refractive index is discovered with increasing silicon area and for higher refractive index claddings. The next step is the evaluation of the coupling coefficient, which is related to the gap between the straight and bent waveguide and their structure. In particular, it is found to increase with longer radii and lower gaps, not to mention the presence of slabs which laterally spread the optical pulse. Afterwards, the impact of the radius on the optical loss has been studied. Notably, with decreasing bend radius the loss increases due to the overlap with the cladding. This gain is lesser for radii of more than 5 $\mu$m, below which it starts skyrocketing.

Finally, the ring modulator is optimized taking into account different

factors:

- First, the impact of the width of the intrinsic region is evaluated. Large widths correspond to lower modulation capabilities but at the same time the loss is less pronounced. The optimal value thus found is 0.6 $\mu$m.

- Second, the height of the lateral slabs is considered. Bulky slabs allow a larger interaction between doped areas and optical mode and, as a result, they are preferable in terms of modulation efficacy. However, the loss thus introduced is extremely high and therefore a trade-off height of 70 nm has been chosen.

- Third, the optimization has been focused on the width of the lateral slabs. Longer slabs result in a minor proximity with the electric contacts and, as a consequence, they provide low currents and poor modulations. At the same time, however, the capacitance grows due to the sheer size of the device. On the other hand, overly short slabs entail exceedingly high losses and therefore cannot be taken into consideration. The optimal value has been set to 1.35 $\mu$m.

- Fourth, the doping concentration is analyzed. In particular, the doping profile has been changed from constant to a more realistic diffusive. Low doping levels have been discarded since much improvement could be achieved with only slightly more doped areas. However, at high doping concentrations a flattening of the modulation efficiency becomes clearly noticeable while the electrical properties keep steadily worsening. The analysis of some important optical parameters has been carried out as well. In particular, the optical spectrum becomes less desirable with increasing doping while parameters mainly comprising the refractive index variation, such as the modulation efficiency $V_\pi L$, improve. Consequently, the optimal doping concentration chosen is $10^{20}$ cm$^{-3}$ for the regions in close proximity to the electric contacts and $10^{18}$ cm$^{-3}$ for the slabs in the vicinity of the optical waveguide.

- Fifth, the influence of the background doping (pepi) on the device parameters is taken into account. It is found that by increasing the doping in the intrinsic region the modulation is more effective, especially in the case of n doping, even though the result is almost negligible compared to other effects.

- Sixth, the behavior of the device due to different bend radii is studied. In particular, the effective index is seen to decrease with small radii

since the radiation is further overlapping with the cladding which has a lower refractive index. Moreover, small rings display a lower loss when not biased. It is also important to point out that, when the ring is small, there is more oscillation of the refractive index while varying the radius, both for the real and the imaginary part. Therefore, once a critical dimension is reached, not much can be gained in terms of performance by increasing the radius.

- Lastly, a frequency analysis is carried out in order to investigate the response of the device at different wavelengths. Unfortunately, a mistake has been made while fitting the material properties in Lumerical and as a result the absorption curve is plainly wrong while the group index shows an unrealistic resonance peak at certain frequencies. On the other hand, the real part of the refractive index has been fit properly and shows a decrease of the refractive index and its variation with increasing wavelength, with a steeper curve in the case of long wavelengths.

It has been found that low voltages (even less than 1 V) are already sufficient to obtain a full modulation without jeopardizing other parameters such as ER or causing an excess of current.

## 7.2 Future Works

In this thesis work no attention has been paid to thermal phenomena that usually take place in any electronic device during operation. These parasitic effects can be detrimental for the proper behavior of the apparatus since they alter its electrical and optical properties. For instance, as pointed out in 4.3.4, the temperature influences directly the refractive index, leading to shifts of the output spectrum which can completely negate the modulation by dephasing the optical wavelength from the ring resonance. As a consequence, a careful analysis of the temperature dependence has to be carried out to thoroughly investigate the operation of a ring modulator.

Furthermore, in [110] the authors present a new and improved version of equations (4.8) and (4.9), which in the case of $\lambda_0 = 1550$ nm read

$$\Delta n = -5.4 \times 10^{-22} \Delta N_e^{1.011} - 1.53 \times 10^{-18} \Delta N_h^{0.838} \tag{7.1}$$

$$\Delta \alpha = 8.88 \times 10^{-21} \Delta N_e^{1.167} + 5.84 \times 10^{-20} \Delta N_h^{1.109} \tag{7.2}$$

Therefore, the analysis should be carried through employing these two relations instead of the old and outdated ones in order to obtain a more accurate result.

Another possibility is to take advantage of the different behavior of the carriers when it comes to light modulation (see figure 4.5) by designing asymmetric devices in order to increase the contribution of the holes in the waveguide. Hence, it would be possible to achieve a better and more efficient modulation of the driving signal, increasing the refractive index variation and reducing the loss with respect to a traditional symmetric device.

# Chapter 8

# Appendix

## 8.1 App. A: Derivation of Gauss' Law

Some common properties of vector calculus are:

$$\nabla \cdot (\nabla \times \bar{a}) = 0 \quad \forall \bar{a} \in \mathbb{R}^3 \tag{8.1}$$

$$\nabla \times \nabla a = 0 \quad \forall a \in \mathbb{R} \tag{8.2}$$

Stokes' theorem states that (refer to figure 8.1 for a visual representation)

$$\oint_C \bar{a} \cdot d\bar{l} = \int_S \nabla \times \bar{a} \cdot \hat{n} \, dS \tag{8.3}$$

Where $\hat{n}$ is a versor always orthogonal to the surface $S$. $C$ is a closed line that acts as a boundary for $S$.

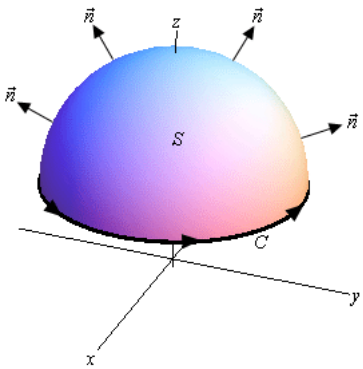


Figure 8.1: *Surface $S$ with closed boundary curve $C$* [111]

Gauss' theorem (divergence theorem) states that (refer to figure 8.2 for a visual representation)

$$\oint_S \bar{a} \cdot \hat{n} \, dS = \int_V \nabla \cdot \bar{a} \, dV \tag{8.4}$$

Where $\hat{n}$ is a versor always orthogonal to the surface.

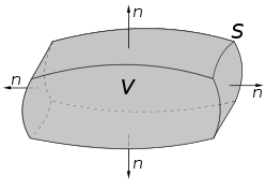


Figure 8.2: *Volume V bounded by closed surface S* [112]

Given equations (2.1) and (8.1), one can write

$$\nabla \cdot (\nabla \times \bar{e}(\bar{r}, t)) = \nabla \cdot (-\frac{\partial \bar{b}(\bar{r}, t)}{\partial t}) = -\frac{\partial}{\partial t}(\nabla \cdot \bar{b}(\bar{r}, t)) = 0$$

Therefore we can conclude that $\nabla \cdot \bar{b}(\bar{r}, t) = 0$. Furthermore, following Gauss' theorem, it is

$$\int_V \nabla \cdot \bar{b}(\bar{r}, t) \, dV = 0 \iff \oint_S \bar{b}(\bar{r}, t) \cdot \hat{n} \, dS$$

Meaning that any component for which $\bar{b}(\bar{r}, t) \cdot \hat{n}$ is positive is balanced by a component for which the dot product is negative. As a consequence, $\bar{b}(\bar{r}, t)$ is said to be a solenoidal field whose field lines are closed [18].

Once again, because of the same property (8.1), we can write

$$\nabla \cdot (\nabla \times \bar{h}(\bar{r}, t)) = \nabla \cdot (\frac{\partial \bar{d}(\bar{r}, t)}{\partial t} + \bar{j}(\bar{r}, t)) = \frac{\partial}{\partial t}(\nabla \cdot \bar{d}(\bar{r}, t)) + \nabla \cdot \bar{j}(\bar{r}, t) = 0$$

Furthermore, the circulation of the current density can be written as

$$\oint_S \bar{j}(\bar{r}, t) \cdot \hat{n} \, dS = -\frac{\partial Q_V(\bar{r}, t)}{\partial t}$$

Where $Q_V$ is the total charge contained in the volume $V$. Moreover, $Q_V(\bar{r}, t) = \int_V \rho_V(\bar{r}, t) \, dV$ is the integral of the electric charge density in the volume, yielding (the volume is considered constant in time) [17]

$$\oint_S \bar{j}(\bar{r},t)\cdot\hat{n}\,dS = -\frac{\partial}{\partial t}\int_V \rho_V(\bar{r},t)\,dV = -\int_V \frac{\partial}{\partial t}\rho_V(\bar{r},t)\,dV$$

By applying (8.4) to the left side of the equation we obtain

$$\int_V \nabla\cdot\bar{j}(\bar{r},t)\,dV = \int_V -\frac{\partial}{\partial t}\rho_V(\bar{r},t)\,dV$$

When the volume shrinks to a point we can infer that

$$\nabla\cdot\bar{j}(\bar{r},t) = -\frac{\partial}{\partial t}\rho_V(\bar{r},t)$$

Obtaining again equation (2.4).

## 8.2 App. B: Plane wave derivation (generic media)

A generic medium is a material for which the electrical conductivity is not negligible ($\sigma \neq 0$) and therefore the phasor Maxwell's equations (2.13) and (2.14) read [17]

$$\nabla\times\bar{E}(\bar{r}) = -i\omega\mu_0\bar{H}(\bar{r}) \tag{8.5}$$

$$\nabla\times\bar{H}(\bar{r}) = \sigma\bar{E}(\bar{r}) + i\omega\varepsilon\bar{E}(\bar{r}) + \bar{J}(\bar{r}) = i\omega\varepsilon_c\bar{H}(\bar{r}) + \bar{J}(\bar{r}) \tag{8.6}$$

Where $\varepsilon_c = \varepsilon - i\frac{\sigma}{\omega}$ is called complex permittivity (accounting for losses). Moreover, the Laplacian operator $\nabla^2 :\ \mathbb{R}^3 \mapsto \mathbb{R}^3$ is defined as

$$\nabla^2\bar{a} \triangleq \nabla(\nabla\cdot\bar{a}) - \nabla\times(\nabla\times\bar{a}) \tag{8.7}$$

We can further derive in the case of the electric field and $\sigma \neq 0$

$$\nabla\times(\nabla\times\bar{E}(\bar{r})) = -i\omega\mu_0\nabla\times\bar{H}(\bar{r}) = -i\omega\mu_0(i\omega\varepsilon_c\bar{E}(\bar{r})) = \omega^2\mu_0\varepsilon_c\bar{E}(\bar{r})$$

And

$$\nabla\times(\nabla\times\bar{E}(\bar{r})) = \cancel{\nabla(\nabla\cdot\bar{E}(\bar{r}))} - \nabla^2\bar{E}(\bar{r})$$

Where the canceled term is due to the fact that the source is not present in the considered region of space [17].

Combining the two lines above, one obtains again the Helmholtz equations (2.17) and (2.18).

Furthermore, by writing

$$\bar{E}(\bar{r}) = E_x(\bar{r})\hat{x} + E_y(\bar{r})\hat{y} + E_z(\bar{r})\hat{z}$$

With

$$E_i(\bar{r}) = E_i(x, y, z) = E_{oi} f_x(x) f_y(y) f_z(z)$$

Obtained by virtue of separation of the variables, we have

$$\nabla^2 E_i(\bar{r}) + \omega^2 \mu_0 \varepsilon_c E_i(\bar{r}) = 0 \;\; \forall i = x, y, z$$

$$\frac{\partial^2 Ei(\bar{r})}{\partial x^2} + \frac{\partial^2 Ei(\bar{r})}{\partial y^2} + \frac{\partial^2 Ei(\bar{r})}{\partial z^2} + \omega^2 \mu_0 \varepsilon_c E_i(\bar{r}) = 0$$

$$\cancel{E_{oi}} \frac{\partial^2 f_x(x)}{\partial x^2} f_y(y) f_z(z) + \cancel{E_{oi}} \frac{\partial^2 f_y(y)}{\partial y^2} f_x(x) f_z(z) + \cancel{E_{oi}} \frac{\partial^2 f(z)}{\partial z^2} f_x(x) f_y(y) + \\ + \omega^2 \mu_0 \varepsilon_c \cancel{E_{oi}} f_x(x) f_y(y) f_z(z) = 0$$

$$\frac{\partial^2 f_x(x)}{\partial x^2} \frac{1}{f_x(x)} + \frac{\partial^2 f_y(y)}{\partial y^2} \frac{1}{f_y(y)} + \frac{\partial^2 f(z)}{\partial z^2} \frac{1}{f_z(z)} = -\omega^2 \mu_0 \varepsilon_c$$

Since the right-hand term is a constant, the only possible solution is for the three left-hand terms to be constants as well and not functions, such as

$$\frac{\partial^2 f_i(i)}{\partial i^2} \frac{1}{f_i(i)} = s_i^2, \;\; i = x, y, z$$

Therefore we can state that

$$f_i(i) = F_{0i}^{+} e^{-s_i \cdot i} + F_{oi}^{-} e^{s_i \cdot i}$$

$$s_x^2 + s_y^2 + s_z^2 = -\omega^2 \mu_0 \varepsilon_c$$

With $F_{0i}^{+}$ and $F_{0i}^{-}$ integration constants depending on the source.
A possible solution, called plane wave solution, is given by

$$E_i(\bar{r}) = E_{0i} e^{-s_x \cdot x - s_y \cdot y - s_z \cdot z} = E_{0i} e^{-\bar{s} \cdot \bar{r}}$$

$$\bar{E}(\bar{r}) = \bar{E}_0 e^{-\bar{s} \cdot \bar{r}}$$

As in chapter 2.1.2.

## 8.3 App. C: Power balance (electromagnetic field)

In the case of lossy media ($\varepsilon_c = \varepsilon - i\frac{\sigma}{\omega}$) and starting from equations (8.5) and (8.6), we can write

$$(\nabla \times \bar{E}(\bar{r})) \cdot \bar{H}^*(\bar{r}) = -i\omega\mu_0 \bar{H}(\bar{r}) \cdot \bar{H}^*(\bar{r}) \tag{8.8}$$

$$(\nabla \times \bar{H}(\bar{r}))^* \cdot \bar{E}(\bar{r}) = (\sigma \bar{E}^*(\bar{r}) - i\omega\varepsilon \bar{E}^*(\bar{r}) + \bar{J}^*(\bar{r})) \cdot \bar{E}(\bar{r}) \tag{8.9}$$

Where $\bar{E}(\bar{r}) \cdot \bar{J}^*(\bar{r})$ [$^{\mathrm{W}}/_{\mathrm{m}^3}$] is the power volume density, we obtain, after subtracting the two equations (8.9)-(8.8)

$$(\nabla \times \bar{H}(\bar{r}))^* \cdot \bar{E}(\bar{r}) - (\nabla \times \bar{E}(\bar{r})) \cdot \bar{H}^*(\bar{r}) = \sigma|\bar{E}(\bar{r})|^2 - i\omega\varepsilon|\bar{E}(\bar{r})|^2 + \\ + \bar{J}^*(\bar{r})) \cdot \bar{E}(\bar{r}) + i\omega\mu_0|\bar{H}(\bar{r})|^2$$

That is

$$-\bar{E}(\bar{r}) \cdot \bar{J}^*(\bar{r}) = \sigma|\bar{E}(\bar{r})|^2 + i\omega(\mu_0|\bar{H}(\bar{r})|^2 - \varepsilon|\bar{E}(\bar{r})|^2) + \nabla \cdot (\bar{E}(\bar{r}) \times \bar{H}^*(\bar{r}))$$

When considering a volume V and dividing by 2 to account for the power nature of the components, the relation can be written as

$$\int_V (-\frac{\bar{E}(\bar{r}) \cdot \bar{J}^*(\bar{r})}{2})\, \partial V = \int_V \frac{\sigma|\bar{E}(\bar{r})|^2}{2}\, \partial V + i\omega \int_V (\frac{\mu_0|\bar{H}(\bar{r})|^2}{2} - \frac{\varepsilon|\bar{E}(\bar{r})|^2}{2})\, \partial V + \\ + \int_V \nabla \cdot (\frac{\bar{E}(\bar{r}) \times \bar{H}^*(\bar{r})}{2})\, \partial V$$

By employing relation (8.4)

$$\int_V (-\frac{\bar{E}(\bar{r}) \cdot \bar{J}^*(\bar{r})}{2})\, \partial V \,\textcircled{1} = \int_V \frac{\sigma|\bar{E}(\bar{r})|^2}{2}\, \partial V \,\textcircled{2} + \\ + i\omega \int_V (\frac{\mu_0|\bar{H}(\bar{r})|^2}{2} - \frac{\varepsilon|\bar{E}(\bar{r})|^2}{2})\, \partial V \,\textcircled{3} + \oint_{S_V} (\frac{\bar{E}(\bar{r}) \times \bar{H}^*(\bar{r})}{2}) \cdot \hat{n}\, \partial S_V \,\textcircled{4} \tag{8.10}$$

Where

- ① is the complex power generated by the source inside the volume;
- ② is the power dissipation due to Joule effect (active power);
- ③ is the reactive power accumulated in the volume;
- ④ is the complex power flowing through $S_V$ (the radiated power);

The active power balance reads

$$Re[\int_V (-\frac{\bar{E}(\bar{r}) \cdot \bar{J}^*(\bar{r})}{2})\ \partial V] = \int_V \frac{\sigma|\bar{E}(\bar{r})|^2}{2}\ \partial V + \oint_{S_V} Re[(\frac{\bar{E}(\bar{r}) \times \bar{H}^*(\bar{r})}{2})] \cdot \hat{n}\ \partial S_V$$

Where the left-hand term is always positive (it is a real generator) and so is the Joule component. Consequently, the active radiated power can be either positive or negative (depending on its relation with the surface).

The reactive power balance reads

$$Im[\int_V (-\frac{\bar{E}(\bar{r}) \cdot \bar{J}^*(\bar{r})}{2})\ \partial V] = \omega \int_V (\frac{\mu_0|\bar{H}(\bar{r})|^2}{2} - \frac{\varepsilon|\bar{E}(\bar{r})|^2}{2})\ \partial V + \\ + \oint_{S_V} Im[(\frac{\bar{E}(\bar{r}) \times \bar{H}^*(\bar{r})}{2})] \cdot \hat{n}\ \partial S_V$$

Where the right-most term represents the reactive irradiated power which decays rapidly with the distance from the source (it is only present in the so-called near field or Fresnel region) [17].

# Bibliography


[1] P. Damas, X. L. Roux, D. L. Bourdais, E. Cassan, D. Marris-Morini, N. Izard, T. Maroutian, P. Lecoeur, and L. Vivien, "Wavelength dependence of pockels effect in strained silicon waveguides," *Optics Express*, vol. 22, p. 22095, sep 2014.

[2] A. Narasimha, B. Analui, Y. Liang, T. J. Sleboda, S. Abdalla, E. Balmater, S. Gloeckner, D. Guckenberger, M. Harrison, R. G. M. P. Koumans, D. Kucharski, A. Mekis, S. Mirsaidi, D. Song, and T. Pinguet, "A fully integrated 20-gb/s optoelectronic transceiver implemented in a standard 0.13 um cmos soi technology," *IEEE Journal of Solid-State Circuits*, vol. 42, pp. 2736–2744, dec 2007.

[3] A. L. Lentine and C. T. DeRose, "Challenges for optical interconnect for beyond moore's law computing," in *2016 IEEE International Conference on Rebooting Computing (ICRC)*, IEEE, oct 2016.

[4] J. Jung, H. Nam, B. Lee, J. O. Byun, and N. S. Kim, "Fiber bragg grating temperature sensor with controllable sensitivity," *Applied Optics*, vol. 38, p. 2752, may 1999.

[5] H.-G. von Ribbeck, M. T. Wenzel, R. Jacob, and L. M. Eng, "Scattering near-field microscopy in the THz region using a free-electron laser," in *35th International Conference on Infrared, Millimeter, and Terahertz Waves*, IEEE, sep 2010.

[6] A. H. Hielscher, A. Y. Bluestone, G. S. Abdoulaev, A. D. Klose, J. Lasker, M. Stewart, U. Netz, and J. Beuthan, "Near-infrared diffuse optical tomography," *Disease Markers*, vol. 18, no. 5-6, pp. 313–337, 2002.

[7] W. Bogaerts, P. D. Heyn, T. V. Vaerenbergh, K. D. Vos, S. K. Selvaraja, T. Claes, P. Dumon, P. Bienstman, D. V. Thourhout, and R. Baets, "Silicon microring resonators," *Laser & Photonics Reviews*, vol. 6, pp. 47–73, sep 2011.

[8] S. Spector, C. Sorace, M. Geis, M. Grein, J. Yoon, T. Lyszczarz, E. Ippen, and F. Kartner, "Operation and optimization of silicon-diode-based optical modulators," *IEEE Journal of Selected Topics in Quantum Electronics*, vol. 16, no. 1, pp. 165–172, 2010.

[9] G. T. Reed, G. Mashanovich, F. Y. Gardes, and D. J. Thomson, "Silicon optical modulators," *Nature Photonics*, vol. 4, pp. 518–526, jul 2010.

[10] Q. Xu, S. Manipatruni, B. Schmidt, J. Shakya, and M. Lipson, "12.5 gbit/s carrier-injection-based silicon micro-ring silicon modulators," *Optics Express*, vol. 15, p. 430, jan 2007.

[11] H. Yu, D. Ying, M. Pantouvaki, J. V. Campenhout, P. Absil, Y. Hao, J. Yang, and X. Jiang, "Trade-off between optical modulation amplitude and modulation bandwidth of silicon micro-ring modulators," *Optics Express*, vol. 22, p. 15178, jun 2014.

[12] W. R. McKinnon, D. X. Xu, C. Storey, E. Post, A. Densmore, A. Delâge, P. Waldron, J. H. Schmid, and S. Janz, "Extracting coupling and loss coefficients from a ring resonator," *Optics Express*, vol. 17, p. 18971, oct 2009.

[13] Y. A. Vlasov and S. J. McNab, "Losses in single-mode silicon-on-insulator strip waveguides and bends," *Optics Express*, vol. 12, no. 8, p. 1622, 2004.

[14] S. Kasap, *Optoelectronics and Photonics: Principles and Practices*. Pearson Education Limited, 2013.

[15] C. G. Someda, *Electromagnetic Waves*. CRC Press, 2017.

[16] G. R. Fowles, *Introduction to Modern Optics (Dover Books on Physics)*. Dover Publications, 1989.

[17] M. Santagiustina, *Antennas and Wireless Propagation*. Universita degli Studi di Padova, 2018.

[18] D. De-Ceglia, *Biophotonics*. Universita degli Studi di Padova, 2018.

[19] P. Mazzoldi, M. Nigro, and C. Voci, *Fisica vol. 2 - Elettromagnetismo, onde*. Edises, 2000.

[20] "Polarization." `https://en.wikipedia.org/wiki/Polarization_(waves)`. Accessed: 2019-08-15.

[21] S. Trippe, "Polarization and polarimetry: A review," *Journal of The Korean Astronomical Society*, 2014.

[22] "GroupIndex." `https://en.wikipedia.org/wiki/Group_velocity`. Accessed: 2019-08-15.

[23] "PulseTimeFrequencyRelation." `https://www.brown.edu/research/labs/mittleman/sites/brown.edu.research.labs.mittleman/files/uploads/lecture21_0.pdf`. Accessed: 2019-08-15.

[24] M. Helm, *Quantum Mechanics for Nanoelectronics*. Technische Universitaet Dresden, 2018.

[25] A. K. Ghatak, I. C. Goyal, and A. Kumar, "Propagation of a gaussian pulse through an optical fiber: applicability of geometrical optics," *Applied Optics*, vol. 14, p. 2330, oct 1975.

[26] "GaussianPulse." `https://ufox.cfel.de/sites/sites_cfelgroups/site_cfel-ufox/content/e16281/e86791/e86828/e86829/e86833/2013_04_16UFSC_Lec_3.pdf`. Accessed: 2019-08-15.

[27] "Interference." `https://physics.stackexchange.com/questions/107286/does-interference-take-place-only-in-waves-parallel-to-each-other`. Accessed: 2019-08-15.

[28] F. Moresco, *Molecular Electronics*. Technische Universitaet Dresden, 2018.

[29] "AtomicOrbitals." `http://www231.pair.com/fzwester/courses/bis10v/week1/13atomicorbitals.html`. Accessed: 2019-08-15.

[30] M. Meneghini, *Optoelectronics for Green Technologies*. Universita degli Studi di Padova, 2017.

[31] "EnergyBands." `https://byjus.com/physics/what-are-energy-bands/`. Accessed: 2019-08-15.

[32] C. F. Bohren and D. R. Huffman, *Absorption and Scattering of Light by Small Particles*. Wiley-VCH, 1998.

[33] L. Palmieri, *Optical Network Devices*. Universita degli Studi di Padova, 2018.

[34] D. R. Solli, P. Koonath, and B. Jalali, "Inverse raman scattering in silicon," *arXiv*, 2008.

[35] R. Pratt, L. LaJohn, V. Florescu, T. Surić, B. Chatterjee, and S. Roy, "Compton scattering revisited," *Radiation Physics and Chemistry*, vol. 79, pp. 124–131, feb 2010.

[36] L. Rigamonti, "Schiff base metal complexes for second order nonlinear optics," *La chimica e l'industria: rivista della societa chimica italiana*, 2010.

[37] R. W. Boyd, *Nonlinear Optics*. ACADEMIC PR INC, 2019.

[38] J. Schmiedmayer, *Laseer Physics and Photonics*. Universitaet Heidelberg, 2002.

[39] M. Habibi and M. Davoodianidalik, "Self-focusing of high-power laser beam through plasma," in *High Power Laser Systems*, InTech, oct 2018.

[40] D. Mittleman, *Ultrafast Optics*. Brown University, 2017.

[41] R. W. Boyd, *Introduction to Nonlinear Optics*. International School of Physics "Enrico Fermi", 2014.

[42] R. Hamerly, D. Gray, C. Rogers, L. Mirzoyan, M. Namdari, and K. Jamshidi, "Optical bistability, self-pulsing and XY optimization in silicon micro-rings with active carrier removal," in *Physics and Simulation of Optoelectronic Devices XXV* (B. Witzigmann, M. Osiński, and Y. Arakawa, eds.), SPIE, feb 2017.

[43] "SnellLaw." `https://em.geosci.xyz/content/maxwell1_fundamentals/reflection_and_fraction/Snells_law.html`. Accessed: 2019-08-15.

[44] P. Horak, *Optical Fibres*. University of Southampton, 2018.

[45] "Diffusereflection." `https://en.wikipedia.org/wiki/Diffuse_reflection`. Accessed: 2019-08-15.

[46] K. Singh, "Optical fibre communication: A review," in *Singh2017OpticalFC*, 2017.

[47] A. Acakpovi and P. L. M. V. Matoumona, "Comparative analysis of plastic optical fiber and glass optical fiber for home networks," in *2012 IEEE 4th International Conference on Adaptive Science & Technology (ICAST)*, IEEE, oct 2012.

[48] Y. Koike and M. Asai, "The future of plastic optical fiber," *NPG Asia Materials*, vol. 1, pp. 22–28, oct 2009.

[49] S. Grassini, M. Ishtaiwi, M. Parvis, and A. Vallan, "Design and deployment of low-cost plastic optical fiber sensors for gas monitoring," *Sensors*, vol. 15, pp. 485–498, dec 2014.

[50] "OpticalFIberCable." `https://community.fs.com/blog/the-advantages-and-disadvantages-of-optical-fibers.html`. Accessed: 2019-08-15.

[51] J. Kambiz, *Integrated Photonic Devices*. Technische Universitaet Dresden, 2019.

[52] "OpticalFiberModes." `https://www.fiberoptics4sale.com/blogs/archive-posts/95048070-basic-optics-for-optical-fiber`. Accessed: 2019-08-15.

[53] "Modes." `https://www.computational-photonics.eu/oms.html`. Accessed: 2019-08-15.

[54] K. Okamoto, *Fundamentals of Optical Waveguides (Optics & Photonics Series)*. Academic Press, 2005.

[55] S. Spolitis and G. Ivanovs, "Realization of combined chromatic dispersion compensation methods in high speed WDM optical transmission systems," *Electronics And Electrical Engineering*, vol. 113, sep 2011.

[56] "ModalDispersion." `http://www.fiber-optic-cable-sale.com/what-can-limit-the-data-transmission-distance.html,`.

[57] O. Heaviside, "ELECTROMAGNETIC INDUCTION AND ITS PROPAGATION (SECOND HALF.)," in *Electrical Papers*, pp. 39–155, Cambridge University Press, 1892.

[58] "ChromaticDispersion." `http://fobasics.blogspot.com/2012/07/chromatic-dispersion.html`. Accessed: 2019-08-15.

[59] S. G. Jennings, R. G. Pinnick, and J. B. Gillespie, "Relation between absorption coefficient and imaginary index of atmospheric aerosol constituents," *Applied Optics*, vol. 18, p. 1368, may 1979.

[60] R. Corvaja, *Optical and Quantum Communications*. Universita degli Studi di Padova, 2017.

[61] G. Ghione, *Semiconductor Devices for High-Speed Optoelectronics*. Cambridge University Press, 2009.

[62] K. Daikoku, "Direct modulation characteristics of semiconductor laser diodes," *Japanese Journal of Applied Physics*, vol. 16, pp. 117–124, jan 1977.

[63] S. Warm, *Electronic Predistortion Strategies For Directly Modulated Laser Systems*. Technische Universitaet Berlin, 2009.

[64] M. Berciano, G. Marcaud, P. Damas, X. L. Roux, P. Crozat, C. A. Ramos, D. P. Galacho, D. Benedikovic, D. Marris-Morini, E. Cassan, and L. Vivien, "Fast linear electro-optic effect in a centrosymmetric semiconductor," *Communications Physics*, vol. 1, oct 2018.

[65] B. Chmielak, M. Waldow, C. Matheisen, C. Ripperda, J. Bolten, T. Wahlbrink, M. Nagel, F. Merget, and H. Kurz, "Pockels effect based fully integrated, strained silicon electro-optic modulator," *Optics Express*, vol. 19, p. 17212, aug 2011.

[66] Y. Turkulets and I. Shalish, "Franz-keldysh effect in semiconductor built-in fields: Doping concentration and space charge region characterization," *Journal of Applied Physics*, vol. 124, p. 075102, aug 2018.

[67] R. S. Jacobsen, K. N. Andersen, P. I. Borel, J. Fage-Pedersen, L. H. Frandsen, O. Hansen, M. Kristensen, A. V. Lavrinenko, G. Moulin, H. Ou, C. Peucheret, B. Zsigri, and A. Bjarklev, "Strained silicon as a new electro-optic material," *Nature*, vol. 441, pp. 199–202, may 2006.

[68] C. Schriever, C. Bohley, J. Schilling, and R. B. Wehrspohn, "Strained silicon photonics," *Materials*, vol. 5, pp. 889–908, may 2012.

[69] R. Soref and B. Bennett, "Electrooptical effects in silicon," *IEEE Journal of Quantum Electronics*, vol. 23, pp. 123–129, jan 1987.

[70] A. Irace, G. Breglio, M. Iodice, and A. Cutolo, "Light modulation with silicon devices," in *Topics in Applied Physics*, pp. 361–391, Springer Berlin Heidelberg, feb 2004.

[71] D. Marris-Morini, L. Vivien, and G. Rasigade, *Optical Modulators in Silicon Photonic Circuits*. Institut d-Electronique Fondamentale - Universite Paris Sud, 2009.

[72] G. Cocorullo, F. G. D. Corte, and I. Rendina, "Temperature dependence of the thermo-optic coefficient in crystalline silicon between room temperature and 550 k at the wavelength of 1523 nm," *Applied Physics Letters*, vol. 74, pp. 3338–3340, may 1999.

[73] J. Fage-Pedersen, L. Frandsen, A. Lavrinenko, and P. Borel, "A linear electrooptic effect in silicon, induced by use of strain," in *3rd IEEE International Conference on Group IV Photonics, 2006.*, IEEE, 2006.

[74] Y. Varshni, "Temperature dependence of the energy gap in semiconductors," *Physica*, vol. 34, pp. 149–154, jan 1967.

[75] Z. Zhang, *Silicon-based Photonic Devices: Design, Fabrication and Characterization.* PhD thesis, KTH Royal Institute of Technology, 2008.

[76] A. Yariv, "Critical coupling and its control in optical waveguide-ring resonator systems," *IEEE Photonics Technology Letters*, vol. 14, pp. 483–485, apr 2002.

[77] G. Mashanovic, *Introduction to Silicon Photonics.* University of Southampton, 2018.

[78] K. D. Vos, *Label-free Silicon Photonics Biosensor Platform with Microring Resonator.* PhD thesis, Universiteit Gent, 2010.

[79] H. Qing-Zhong, Y. Jin-Zhong, C. Shao-Wu, X. Xue-Jun, H. Wei-Hua, and F. Zhong-Chao, "Design, fabrication and characterization of a high-performance microring resonator in silicon-on-insulator," *Chinese Physics B*, vol. 17, pp. 2562–2566, jul 2008.

[80] "Photolitoghraphy." `http://toppicture.dx.am/?top=3&definitions=Photolithography`. Accessed: 2019-08-15.

[81] J. Tian and M. Qiu, "Micro-ring resonators fabricated by focused-ion-beam on SOI," in *Optical Transmission, Switching, and Subsystems VI* (K. ichi Kitayama, P. C. Ghiggino, K. Roberts, and Y. Su, eds.), SPIE, nov 2008.

[82] B. A. Joyce, "Molecular beam epitaxy," *Reports on Progress in Physics*, vol. 48, pp. 1637–1697, dec 1985.

[83] T. Mikolajick, *Innovative Semiconductor Devices.* Technische Universitaet Dresden, 2018.

[84] S. Beebly, *Microsensor Technologies.* University of Southampton, 2018.

[85] A. Samarelli, *Micro Ring Resonators in Silicon-on-Insulator.* PhD thesis, University of Glasgow, 2011.

[86] U. W. Pohl, "Doping, diffusion, and contacts," in *Graduate Texts in Physics*, pp. 225–273, Springer Berlin Heidelberg, 2013.

[87] L. N. Large and R. W. Bicknell, "Ion-implantation doping of semiconductors," *Journal of Materials Science*, vol. 2, pp. 589–609, nov 1967.

[88] "RefractiveIndex." `https://refractiveindex.info/`. Accessed: 2019-08-15.

[89] S. Tanaka, T. Usuki, and Y. Tanaka, "Accurate SPICE model of forward-biased silicon PIN mach zehnder modulator for an energy-efficient multilevel transmitter," *Journal of Lightwave Technology*, vol. 36, pp. 1959–1969, may 2018.

[90] W. Bogaerts, R. Baets, P. Dumon, V. Wiaux, S. Beckx, D. Taillaert, B. Luyssaert, J. V. Campenhout, P. Bienstman, and D. V. Thurnout, "Nanophotonic waveguides in silicon-on-insulator fabricated with CMOS technology," *Journal of Lightwave Technology*, vol. 23, pp. 401–412, jan 2005.

[91] A. S. Jensen, *Fabrication and Characterisation of Silicon Waveguides for High-Speed Optical Signal Processing*. PhD thesis, Technical University of Denmark, 2015.

[92] A. Shutler, "Investigation of propagation loss of passive silicon waveguides using two different etching techniques," *NNIN REU Research Accomplishments*, 2008.

[93] D. Taillaert, W. V. Paepegem, J. Vlekken, and R. Baets, "A thin foil optical strain gage based on silicon-on-insulator microresonators," in *Third European Workshop on Optical Fibre Sensors*, SPIE, jul 2007.

[94] H.-T. Kim and M. Yu, "Cascaded ring resonator-based temperature sensor with simultaneously enhanced sensitivity and range," *Optics Express*, vol. 24, p. 9501, apr 2016.

[95] K. D. Vos, I. Bartolozzi, E. Schacht, P. Bienstman, and R. Baets, "Silicon-on-insulator microring resonator for sensitive and label-free biosensing," *Optics Express*, vol. 15, no. 12, p. 7610, 2007.

[96] "Biosensing." `http://photonics.deib.polimi.it/biosensing/`. Accessed: 2019-08-15.

[97] T. Meynen, "Crow-based optical delay lines : Consequences of fabrication limits on filter response and delay," Master's thesis, Universiteit Gent, 2009.

[98] M. Gad, J. Ackert, D. Yevick, L. Chrostowski, and P. Jessop, "Ring resonator wavelength division multiplexing interleaver," *Journal of Lightwave Technology*, vol. 29, pp. 2102–2109, jul 2011.

[99] M. F. Rosa, L. Rathgeber, R. Elster, N. Hoppe, T. Foehn, M. Schmidt, W. Vogel, and M. Berroth, "Design of a carrier-depletion mach-zehnder modulator in 250 nm silicon-on-insulator technology," *Advances in Radio Science*, vol. 15, pp. 269–281, dec 2017.

[100] G. T. Reed, G. Z. Mashanovich, F. Y. Gardes, M. Nedeljkovic, Y. Hu, D. J. Thomson, K. Li, P. R. Wilson, S.-W. Chen, and S. S. Hsu, "Recent breakthroughs in carrier depletion based silicon optical modulators," *Nanophotonics*, vol. 3, jan 2014.

[101] A. P. Knights and E. Huante-Ceron, "Design considerations for silicon micro-ring modulators," in *Smart Photonic and Optoelectronic Integrated Circuits XVIII* (S. He, E.-H. Lee, and L. A. Eldada, eds.), SPIE, mar 2016.

[102] T. Baba, S. Akiyama, M. Imai, N. Hirayama, H. Takahashi, Y. Noguchi, T. Horikawa, and T. Usuki, "50-gb/s ring-resonator-based silicon modulator," *Optics Express*, vol. 21, p. 11869, may 2013.

[103] C. Fonstad, *Compound Semiconductor Devices*. Massachusetts Institute of Technology, 2003.

[104] Y. Dattner and O. Yadid-Pecht, "Analysis of the effective refractive index of silicon waveguides through the constructive and destructive interference in a mach–zehnder interferometer," *IEEE Photonics Journal*, vol. 3, pp. 1123–1132, dec 2011.

[105] S. Dwivedi, T. V. Vaerenbergh, A. Ruocco, T. Spuesens, P. Bienstman, P. Dumon, and W. Bogaerts, "Measurements of effective refractive index of SOI waveguides using interferometers," in *Advanced Photonics 2015*, OSA, 2015.

[106] "PhotonicIntegratedCircuits." `https://www.edx.org/course/photonic-integrated-circuits`. Accessed: 2019-08-15.

[107] Q. Xu, B. Schmidt, S. Pradhan, and M. Lipson, "Micrometre-scale silicon electro-optic modulator," *Nature*, vol. 435, pp. 325–327, may 2005.

[108] "OpticalBands." `https://www.fiberlabs.com/glossary/about-optical-communication-band/`. Accessed: 2019-08-15.

[109] K. Debnath, D. J. Thomson, W. Zhang, A. Z. Khokhar, C. Littlejohns, J. Byers, L. Mastronardi, M. K. Husain, K. Ibukuro, F. Y. Gardes, G. T. Reed, and S. Saito, "All-silicon carrier accumulation modulator based on a lateral metal-oxide-semiconductor capacitor," *Photonics Research*, vol. 6, p. 373, apr 2018.

[110] M. Nedeljkovic, R. Soref, and G. Z. Mashanovich, "Free-carrier electrorefraction and electroabsorption modulation predictions for silicon over the 1-14- $\mu$m infrared wavelength range," *IEEE Photonics Journal*, vol. 3, pp. 1171–1180, dec 2011.

[111] "StokesOnline." `http://tutorial.math.lamar.edu/Classes/CalcIII/StokesTheorem.aspx`. Accessed: 2019-08-15.

[112] "Divergence." `https://en.wikipedia.org/wiki/Divergence_theorem`. Accessed: 2019-08-15.